博士論文

Sound source characteristics in compressible turbulent flows

(圧縮性乱流中の音源特性に関する研究)

Department of Aeronautics and Astronautics
The University of Tokyo

Daiki Terakado
寺門　大毅

March, 2016

Abstract

It is known that the Mach number and temperature ratio affects the characteristics of supersonic jet noise significantly. Toward the accurate prediction and reduction of the supersonic jet noise, it is necessary to understand those effects correctly. Regardless of the importance of the parameter dependence, however, the systematic explanation with detail underling physics has not been achieved so far.

In the present study, the direct numerical simulations (DNS) of the isotropic compressible turbulence and the temporally evolving compressible mixing layer were conducted to understand the Mach number and the temperature ratio dependence on supersonic jet noise. In the isotropic compressible turbulent simulation, the effects of the turbulent Mach number which is highly related with the smaller turbulent fluctuation were analyzed. In the temporally evolving compressible mixing layer simulation, on the other hand, the effects of two important parameters determining the large scale of turbulence were investigated. In the computation, the convective Mach number and the density (temperature) ratio dependence on the noise characteristics were analyzed. One unique point in the present study is that the source terms of the Lighthill equation which are numerically obtained by DNS results were analyzed to understand the relationship between change in flows and sound sources.

In the isotropic compressible turbulent simulation, it was shown that the sound generation mechanism is highly depending on the turbulent Mach number. For the lower turbulent Mach numbers, the important sound sources are only vortices. For the higher turbulent Mach numbers, on the other hand, eddy shocklets become the other important sound sources in addition to vortices. The relationship between the Reynolds stress term and the entropy term is changed depending on the turbulent Mach number due to the different sound generation mechanism (vortices and shocklets) between the lower and higher turbulent Mach numbers. For the lower turbulent Mach number flows, the Reynolds stress term and the entropy term are intensified each other around vortices, whereas those are canceled out each other across shocklets for the higher turbulent Mach numbers. Note, however, that the contribution of the entropy term for the lower turbu-

lent Mach numbers would become smaller, because the entropy term is generated by the diffusion process around vortices, so that it would become smaller in the higher Reynolds number flows, though the trend was not observed in the present range of the Reynolds number.

In the temporally evolving compressible mixing layer computation, the results showed that the convective Mach number has two important effects. One is that the acoustic waves are weakened with increasing the convective Mach number. This is due to the suppression of vortices because of the compressibility effects. The other important effect is that shocklets in flows affects the acoustic wave characteristics for the higher convective Mach number cases. For those cases, the turbulent Mach number becomes high enough to generate shocklets and the acoustic waves show smaller (based on the scale of vortices), random, and non-linear (but still small) characteristics.

For the density ratio dependence, the strength of acoustic waves becomes weaker with increasing the density (temperature) ratio. There are two possible reasons. One is that the vortices (as sound sources) are weakened with increasing the density ratio. The other reason is that the source terms of the Reynolds stress term and the entropy term are canceled out each other. This is because the mean profile of density affects the Reynolds stress term and the entropy term significantly. Then, it leads to the similar mean profiles of the Reynolds stress term and the entropy term. In addition, the randomness of the Mach angle increases with increasing the density ratio. The results of the Mach angle would suggest the existence of various modes of instability wave moving with different convective Mach number which generates different Mach wave for the higher density ratio cases. The mean temperature difference over the mixing layer leads to locally different speed of sound, so that it would cause the locally different Mach numbers. The other possibility affecting the Mach angle is that the appearance of a lot of different scale structures over the mixing layer for the higher density ratio cases. This is also due to the mean temperature difference across the mixing layer. The temperature difference makes the Reynolds number locally different over the mixing layer and creates many different scales of turbulence. Note, however, that the effect is expected to be smaller at sufficiently high Reynolds number flows, because the Reynolds number difference between upper and lower streams becomes relatively smaller (based on the Reynolds number of the mixing layer) than that of the low Reynolds number flows. Also, at least in the present range of the density ratio and the convective Mach number, the non-linearity of acoustic waves is not changed significantly depending on the density ratio, regardless of the different sound source characteristics between cases.

Acknowledgements

I would like to express my sincere gratitude to my advisor, Professor Kozo Fujii of Institute of Space and Astronautical Science/Japan Aerospace Exploration Agency (ISAS/JAXA). He taught me the importance for conducting research toward real applications and the importance for simplifying the problems to derive meaningful answers. The three years, as a student in Ph.D. course under his supervision, have been fruitful and pleasant, owing greatly to his generous and kind consideration to the students.

I would also like to express my deepest gratitude to my advisor, Associate Professor Akira Oyama of Institute of Space and Astronautical Science/Japan Aerospace Exploration Agency (ISAS/JAXA) for his generous support and encouragement throughout this research.

Also, I would like to thank Professor Kenichi Rinoie, Professor Kojiro Suzuki and Associate Professor Taro Imamura of Department of Aeronautics and Astronautics, the University of Tokyo for participating in my thesis committee, giving helpful discussion regarding to this work.

I am also obliged to Associate Professor Soshi Kawai of Department of Aerospace Engineering, Tohoku University for giving me a lot of chances to grow up and giving me many invaluable advice.

I must thank to Assistant Professor Hikaru Aono of Department of Mechanical Engineering, Tokyo University of Science for giving me wonderful supports and teaching me a lot of important things as a researcher.

I would be remiss if I did not also extend my gratitude to my advisor in Sendai, Professor Yuji Hattori of Institute of Fluid Science, Tohoku University for giving me the basis of research in fluid mechanics. Without the precious experiences under his supervision during the days of Tohoku University, this work could not have been completed.

During my daily research at the section of High Speed Aerodynamics Laboratory of ISAS/JAXA, I wish to thank Assistant Professor Taku Nonomura for giving me so many advice not only regarding to this work but also my future career. I am also thankful to secretariat Ms. Yuko Tamura, Ms. Mari Koyanagi and Ms. Makiko Ito for supporting

me in many ways and students in the lab. Special thanks to students in the lab. (Future) Professor Yoshiaki Abe, Mr. Hiroaki Fukumoto, Mr. Donghwi Lee, Mr. Taufik Sulaiman, Mr. Kento Asano, Mr. Issei Morinaka, Mr. Koichi Morihira, Mr. Akira Matsubara, Mr. Fortunato Nucera, Mr. Yuta Ozawa, Mr. Daisuke Kato, Mr. Takuya Harada, Mr. Hiroaki Nakano, Mr. Yuma Miyakawa, and post doctoral fellow Dr. Makoto Sato, Dr. Takeshi Watanabe, Dr. Aiko Yakeno, Dr. Koji Fujita, Dr. Martin Schlueter, and alumni Dr. Kengo Asada, Dr. Seiichiro Morizawa, Dr. Satoshi Sekimoto, Mr. Yoshinori Ando, Mr. Hiroki Iida, Mr. Naoya Fujioka, Mr. Hiroki Kato, Mr. Katsutoshi Kondo, Mr. Yuki Nagata, Mr. Gabriel Pichon, Mr. Naoki Tanaka for having discussion of various topics of fluid mechanics and helping me to keep my motivation to this study.

Finally, my parents, my sister, my grandmothers and my future wife are always mainstay for me I cannot guess how grateful I am to their support and consideration.

March 2016

Daiki Terakado

Contents

List of Figures

List of Tables

Nomenclature

Roman Symbols

a_l	coefficient of explicit central difference scheme
B_{ij}	two-point correlation of velocity
c	speed of sound
C	adjusting parameter of WENOCU scheme
c_p	specific heat at constant pressure
d	normal distance from surface of shocklets
d_k	optimized weights of WENOCU scheme ($k = 0, 1, 2, 3$)
e	total energy per unit volume
f, g	longitudinal and transverse velocity autocorrelation function (App. C)
E	kinetic energy (Chap. 4)
L_I	integral length scale (Chap. 4)
L_f, L_g	longitudinal and transverse integral length scales (App. C)
L_x, L_y, Lz	computational domain lengths based on initial momentum thickness
k	magnitude of wave number
k_{peak}	peak wave number
k_x, k_z	streamwise and spanwise wave numbers
N	grid points (Chap. 4)
N_x, N_y, N_z	grid points in the x, y and z directions (Chap. 5)
M_c	convective Mach number
M_J	jet Mach number
M_t	turbulent Mach number
$\mathbf{n}$	shock normal vector
p	pressure
p_r	pressure ratio across shocklets
$p'_{s=0}$	isentropic acoustic pressure
P	first invariant of velocity gradient tensor
Pr	Prandtl number

q_i	heat flux in the ith direction
Q	second invariant of velocity gradient tensor (Chap. 4 and Chap. 5)
R	gas constant
R_{ij}	Reynolds stress
Re_λ	Reynolds number based on Taylor micro scales
Re_θ	Reynolds number based on momentum thickness
s	density ratio between upper and lower streams in mixing layer
s	entropy (Chap. 4)
S_k	velocity derivative skewness
$S_k(p')$	skewness of pressure fluctuation (Chap. 1)
S_{all}	overall sound source term of Lighthill equation
$S_{\text{Re}}, S_{\text{en}}, S_{\text{vis}}$	Reynolds stress term, entropy term and viscous term of Lighthill equation
$S_{\text{en}_p}, S_{\text{en}_\rho}$	pressure and density contributions of entropy term of Lighthill equation
S_{ij}	strain rate tensor
t	time
T	temperature
T_{ij}	Lighthill's turbulent stress tensor
T_{ratio}	temperature ratio
u_i	velocity component in the ith direction
u, v, w	velocity components in the x, y, and z directions
U_c	convective velocity
x_i	Cartesian coordinate in the ith direction
x, y, z	Cartesian coordinates in the x, y, and z directions
W	enstrophy

Greek Symbols

α, β	free parameters for KG splitting
β_k, τ_6	smoothness indicators of WENOCU scheme ($k = 0, 1, 2, 3$)
δ_θ	momentum thickness
δ_{ij}	Kronecker delta
Δt	time step
Δu	mean streamwise velocity difference in mixing layer
Δx	grid spacing in the x direction
η	Kolmogorov length scale
ε	energy dissipation
γ	ratio of specific heats

κ	thermal conductivity
λ	Taylor micro scale (Chap. 4)
λ_f, λ_g	longitudinal and transverse Taylor micro scales (App. C)
λ_x, λ_z	streamwise and spanwise Taylor micro scales (Chap. 5)
μ	viscosity
ν	kinematic viscosity
ω	vorticity
Ω	rotation rate tensor
ω_k	non-linear weights in WENOCU
ϕ	Mach angle (Chap. 5)
Φ	Ducros sensor
ρ	density
ρ_r	density ratio across shocklets
τ	large-eddy turn over time
τ_{ij}	viscous stress tensor
θ	dilatation
ξ_i	three eigenvalues of velocity gradient tensor

Subscripts

ave	averaged value of upper and lower streams in mixing layer
inc	quantity for incompressible flow
i,c	incompressible and compressive components of velocity
max	maximum value
rms	root mean square value
X	$(x_1, ..., x_d)$
(1),(2)	upstream and downstream values of shock
1,2	upper and lower stream values in mixing layer
0	initial value
steady	value at steady state

Superscripts

skew	skew-symmetric splitting scheme
wenodisp	dissipation part of WENOCU scheme
$'$	Reynolds perturbation
$''$	Favre perturbation
$\bar{()}$	Reynolds averaged quantity

$\tilde{()}$	Favre averaged quantity
$\hat{()}$	Fourier coefficient (Chap. 2)
$\hat{()}$	numerical flux (Chap. 3)
*	non-dimensional quantity

Abbreviations

CFD	computational fluid dynamics
DNS	direct numerical simulation
dB	decibels
ICAO	International Civil Aviation Organization
JAXA	Japan Aerospace Exploration Agency
LES	large-eddy simulation
OASPL	overall sound pressure level
NASA	National Aeronautics and Space Administration
JPDF	joint probability density function
RANS	Reynolds-averaged Navier-Stokes
rms	root mean square
SGS	sub-grid scale
WENOCU	central-upwind weighted essentially non-oscillatory

Chapter 1

Introduction

In this chapter, at first, the background and general features of supersonic jet noise are presented. After the explanation, the recent advancement of the computational prediction of the supersonic jet noise and the relationship between supersonic jets and compressible turbulence are addressed. Then, the previous studies of compressible turbulent flows are introduced. Finally, the objectives and the outlines of this thesis are described.

1.1 Supersonic Jet Noise

Supersonic jet exhausted from rockets and supersonic aircrafts generate a large amount of noise (Fig. 1.1). The very loud noise causes the various issues in designing those transport systems. In rocket launch of H-IIA, for example, the noise level reaches 190 dB which is over 1000 times louder than that of subsonic aircraft engines (120-130dB). For the reliable launch, we need to conduct the very expensive sound vibration tests several times to prevent satellites from malfunction in such severe launch circumstances. Meanwhile, in airline industry, the regulation of noise has been more strict than it was in the past. International Civil Aviation Organization (ICAO) revised the regulation of noise level in 2001 and is expected to revise it again in the near future. The next generation civil supersonic aircrafts should also be strongly desired to satisfy the severe regulation. Therefore, the accurate prediction and reduction of supersonic jet noise is an essential topic for designing the future transport systems.

So far, the basic features of supersonic jets have been clarified by various previous studies[11]. The characteristics of supersonic jet noise are much different from subsonic contour part in which large scale turbulent structures are not sound sources[12], whereas those are one of the most important sound sources in supersonic jets. In supersonic jets,

(a)

(b)

Figure 1.1: Examples of the applications of supersonic jet noise: (a) Rockets; (b) supersonic aircrafts.

large scale turbulence with supersonic speed generates large amount of noise, so called Mach waves. Mach waves are classified into one component of turbulent mixing noise and have been investigated by a lot of researchers up to now. In 1963, Williams[13] derived that the acoustic power of the Mach waves is proportional to the third power of jet velocity U_J^3 by applying the Lighthill's work[12] to the supersonic context. In addition, Tam *et al.* successfully explained the generation mechanism of the Mach waves in 1980's. They showed that the sound sources of Mach waves are supersonically moving wavy wall like instability waves i.e. large scale structures with supersonic speed [14, 15, 16](Fig. 1.2). In addition to Mach waves, it is believed that the other turbulent mixing noise exists. Tam[17] reported that supersonic jet noise has two similarity spectra by analyzing a lot of experimental data of NASA Langley research center. One is for Mach waves, and the other is for acoustic waves from fine scale turbulence. The classification, however, is somewhat questionable, because the reported spectra of acoustic waves from fine scale turbulence spreads over the wide range of frequencies regardless of the name of fine scale acoustic waves. Also, the given spectra were derived only by fitting from various kind of experimental data, so that no theoretical explanation for the spectra of fine scale acoustic waves was provided. Though the term "fine scale" might not be suitable, his study implied the existence of the other turbulent mixing noise than Mach waves, because the similarity spectra were given from the data including ideally expanded jets in which no shock cell exists. Crackle noise which is generated from high thrust engines of military aircrafts would also be one of the turbulent mixing noise. The noise is known as shock-like N-shaped acoustic waves with sharp compression and shows high skewness

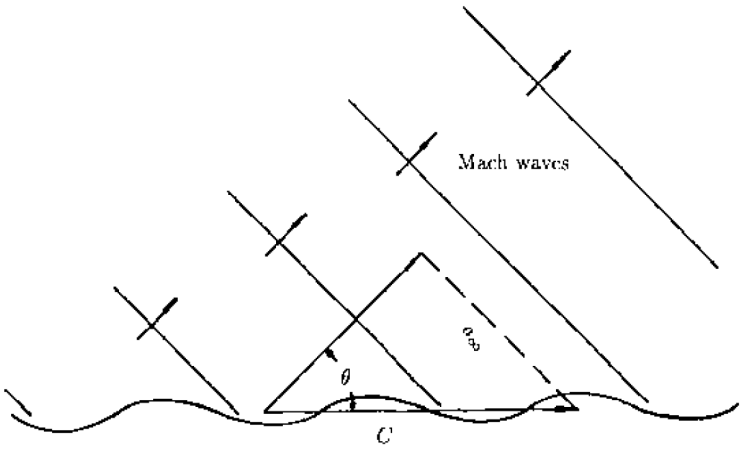

Figure 1.2: Schematic of Mach waves[1].

of pressure $S_k(p') > 0.4$[18]. Some studies suggested that the important parameters for crackle is flow speed[19, 20, 21] and temperature[22, 23], but how those parameters determine the characteristics of crackle remains unclear.

In addition to the turbulent mixing noise, shock associated noise should be taken into account in under- or over-expanded jets where shock train in the jet plume is present due to the pressure mismatch. The interaction between the quasi-periodic shock cells and mixing layer outside the plume creates additional noise components. The noise is relatively important in upstream side, whereas the preferential direction of Mach waves is downstream. It is known that shock-associated noise has two different noise components[1]. One is the screech tone, and the other is the broadband shock noise (Fig. 1.3). Though the firm conclusion has not been acquired yet, the most capable explanation of screech is a feedback loop mechanism proposed by Powell [24, 25]. The process is briefly stated as follows:

1. The initially small amplitude of intrinsic instability in the jet flow grows enough to interact with shock cells at the position of 2nd to 4th shock cells.

2. Due to the interaction between the instability waves and shock cells, acoustic waves are generated.

3. The acoustic waves propagate to the upstream direction and excite the other instability waves at the nozzle lip.

4. The excited instability waves grow with distance and interact with shock cells.

A feedback loop is closed by repeating those processes (Fig. 1.4). For a long period, the study of screech had not progressed much since the work by Powell. In the early 2000's,

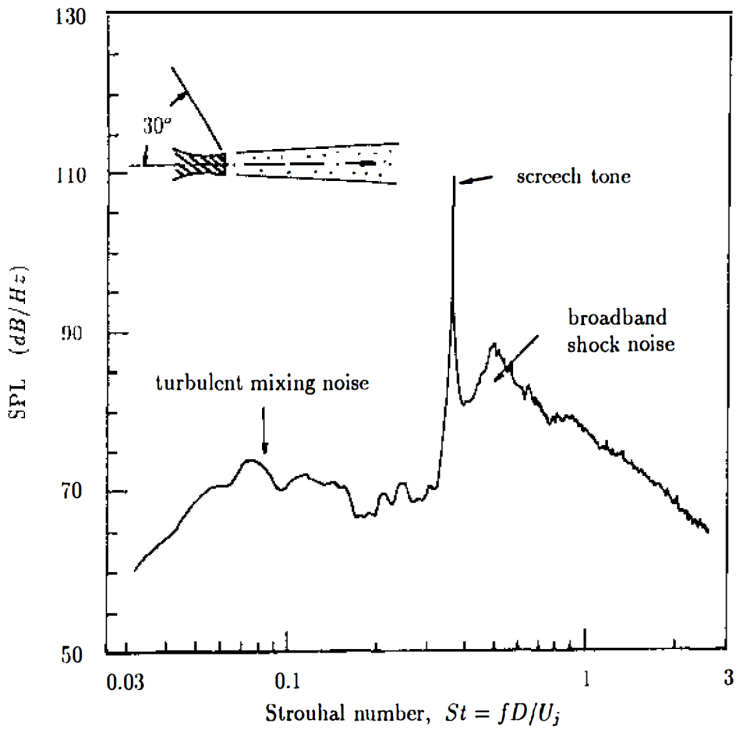

Figure 1.3: Two components of shock associated noise: (a) screech tone; (b) broadband shock noise[1].

however, a generation mechanism of the shock associated noise including both screech and broadband shock noise is proposed by the group of Stanford based on the direct numerical simulation (DNS) and a geometrical theory[26, 2]. They showed that the noise generation can be explained by a shock-leakage near the saddle points of vortices (Fig. 1.5). The requirement for the occurrence of shock-leackage is the unsteadiness of the vortices, so that some distance should be required from the nozzle lip for vortices to grow. The distance would correspond to the observed strong sound source position of the 2nd to 4th shock cells. In further downstream, however, the scale of vortices becomes finer, then, noise generation by shock-leackage becomes weaker. They claimed that the broadband shock noise generates at the further downstream position, instead.

The noise introduced above is known to be very sensitive to the parameters of the Mach number and the temperature ratio of jet plume and the atmosphere. Kandura[27] reported that the velocity dependence on the overall acoustic power is changed from 3 to 6 depending on the jet Mach number M_J by investigating the various experimental data. Bodony and Lele showed that the noise level is weakened in heated jets where the the nozzle exit velocity is set to be the same[28, 29]. Also, Suzuki and Lele[2] demonstrated that the directivity of shock associated noise is weakly changed to the downstream with increasing the temperature ratio. However, no systematic explanation of the effects of

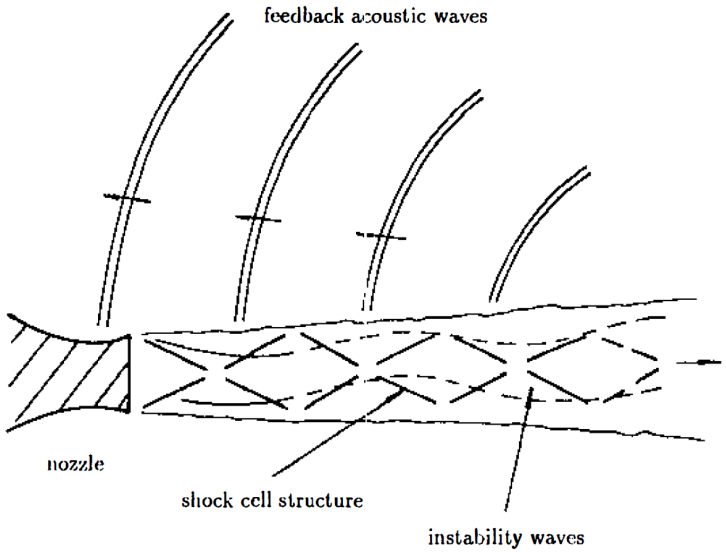

Figure 1.4: Schematic of jet screech[1].

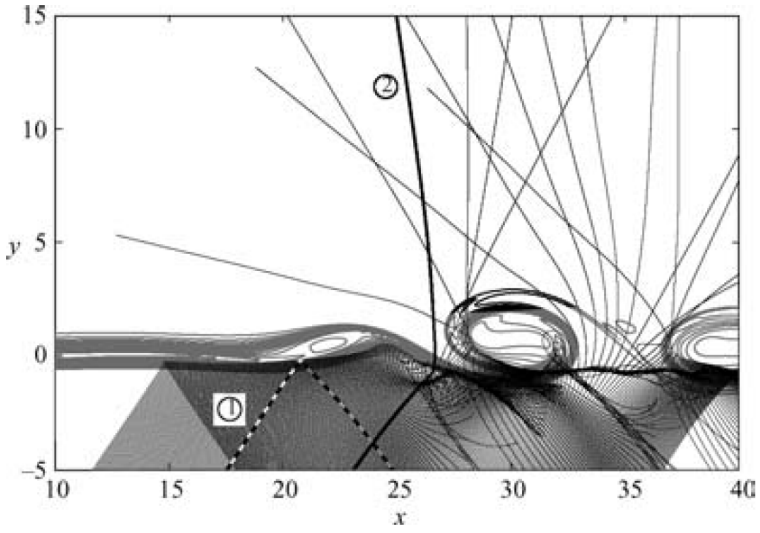

Figure 1.5: Shock-front trajectories in an iso-thermal mixing layer[2].

those parameters on the characteristics of acoustic waves has been achieved so far. In the present study, we tackle the problem of the Mach number and the temperature ratio dependence on acoustic waves toward the more accurate prediction of supersonic jet noise. Meanwhile, our target here is the turbulent mixing noise. This is because the turbulent mixing noise is present regardless of whether a jet is perfectly expanded or not by keeping its characteristics [17, 30]. Also, recent computation of the unstructured large eddy simulation (LES) showed that the shock associated noise can be weakened significantly by using a shevron nozzle[21]. This means that the turbulent mixing noise would become more important even in under- or over expanded jets when such device is used practically. Therefore, we investigate the characteristics of turbulent mixing noise which should be the first priority toward the systematic understanding, accurate prediction and reduction of the supersonic jet noise.

1.2 Computational Prediction of Supersonic Jet Noise

As explained in the previous section, supersonic jet noise is very complicated, because the sound sources are the non-linear unsteady fluid dynamics such as turbulence, shock waves and their interactions. Recent progresses of the computers and numerical methods, however, have enabled us to predict the complex acoustic waves. Japan Aerospace Exploration Agency (JAXA) has also devoted to the computational prediction of various aeroacoustical issues such as noise of rocket launch[31, 32, 33, 34], noise of slat[35] and noise of randing gear[36] of aircrafts. In particular, the recent launch of solid rocket (epsilon rocket) is one of the successful model cases using computational prediction. The acoustic level in the rocket launch of epsilon was 10 dB smaller than that of the previous solid rocket of M-V. In the designing process of launch pad, the computational prediction gave the valuable knowledge[34]. The computational analysis makes it possible to conduct the detail investigation of sound sources with instantaneous unsteady flow data which gives us plenty of knowledge for designing. Basically, sound sources are unsteady flow phenomena, so that DNS or LES should be appropriate to be used, though, some studies chose the Reynolds-averaged Navie-Stokes equations (RANS) for the advantage of computational costs. Many studies (including the examples of JAXA) chose LES (or the hybrid computation of LES and RANS) due to the acceptable computational costs and the capability for predicting the higher Reynolds numbers which are more important in engineering.

Since the late 1990s, various researchers have shown the prediction capability for supersonic jet noise by LES (Fig. 1.6). The recent status of prediction accuracy in the

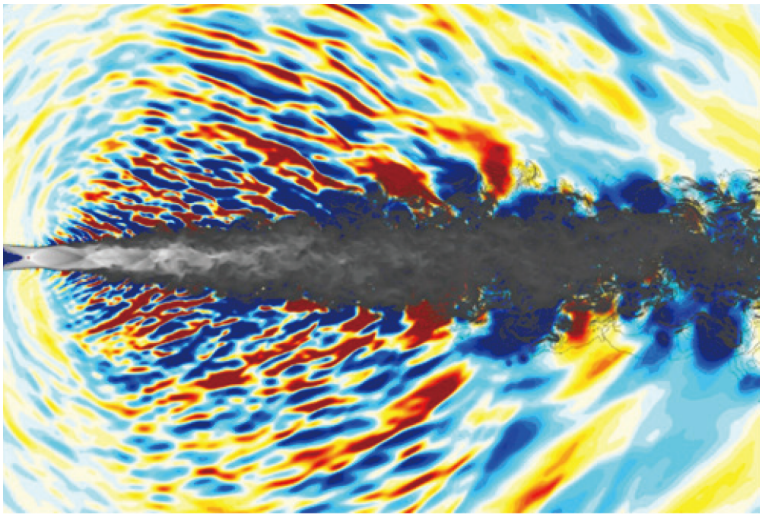

Figure 1.6: An example of the computational prediction of supersonic jet noise by LES[3].

overall sound pressure level (OASPL) is 1-5 dB compared with experiments[37, 38, 3]. The prediction can be more accurate in the near future thanks to the recent advancement of the computational technique and machine power. They enable us to improve the most important factors of inflow[39]. The point of the inflow in the experiments is thin turbulent shear layer. Inflow forcing technique[37, 40, 41] can enhance the turbulent flows and the machine power makes it possible to use more grid points to resolve the thin turbulent shear layer[42, 43]. In subsonic jet studies, the inflow forcing and shear layer thickness change the sound pressure level from 15 to 20 dB depending on whether strong vortex paring in transition (which should not occur in the experimental turbulent jets) occur or not. In supersonic jets, the thin shear layer decreases the sound pressure level by 5dB. Then, it leads to the better prediction due to the similar reason with subsonic counter part[33]. The reason why the relatively small effects of inflow in supersonic case would be the difference of the dominant mode of the vortex paring between subsonic and supersonic jets. Also, the unstructured high-fidelity LES has been developed these days and has enabled us to compute the jet flow with complex nozzle shape[44, 45]. As mentioned in the previous section, the unstructured LES provided the knowledge of the strong noise reduction capability of the shevron nozzle[45].

Computational studies of supersonic jets have contributed not only for the noise prediction, but also for understanding of the complex sound generation mechanism. Bodony and Lele investigated the relationship between the source terms of the Lighthill equation by using the results of LES[29] and suggested that the noise reduction in hot jets would be due to the canceling out of the Reynolds stress term and the entropy term. Nichols *et al.*[21] conducted LES of the heated supersonic jets and reported that the

flow velocity enhances the characteristics of crackle and the jet temperature seems not to affect them. Also, Berland *et al.* [46] confirmed that a noise generation in an under expanded planar jets can be expalined by shock-leakage mechanism proposed by Suzuki and Lele[2].

We have shown that the computational studies of supersonic jet noise is very strong tool for predicting the noise characteristics and understanding the underlying physics, but the computational database is still insufficient to clarify our target of parameter dependence of the Mach number and the temperature ratio. Parametric study of supersonic jet computation needs very large computational resources and contains a lot of uncertainties due to the individual inflow conditions, resolution, sub-grid scale (SGS) model, and method of far-field prediction. One way to resolve the difficulties is to simplify the problem from the whole jet configuration. The generation mechanism of the supersonic jet noise is basically the same as the sound generated from the fundamental compressible turbulent mixing layer (Fig. 1.7). The choice of the temporally evolving mixing layer (not spatially evolving mixing layer) makes it possible for us to save the computational costs and to conduct a parametric study with DNS data. Pressures at the upper and lower streams are the same in the temporally evolving compressible mixing layer, so that the density ratio between the upper and lower streams correspond to the temperature ratio. Thus, the effects of temperature are investigated by changing the density ratio of the temporally evolving compressible mixing layer. Moreover, thanks to the simplified model, we can focus on the pure parameter effects of the Mach number and temperature ratio without considering uncertainties stated above. In the present study, we analyze the effects of two different Mach numbers. The effects of the convective Mach number which is related with large scale turbulence are analyzed by DNS of the temporally evolving compressible mixing layer. In addition, the effects of the turbulent Mach number which is closely related with fine scale turbulent motion is mainly investigated by DNS of the isotropic compressible turbulence. We firstly conduct DNS of the isotropic compressible turbulence to understand the effects of the turbulent Mach number. After that, we investigate the effects of the convective Mach number and the temperature ratio by DNS of the temporally evolving compressible mixing layer. In the next section, previous studies of those compressible turbulent flows are introduced, and the points to focus in the present studies are addressed.

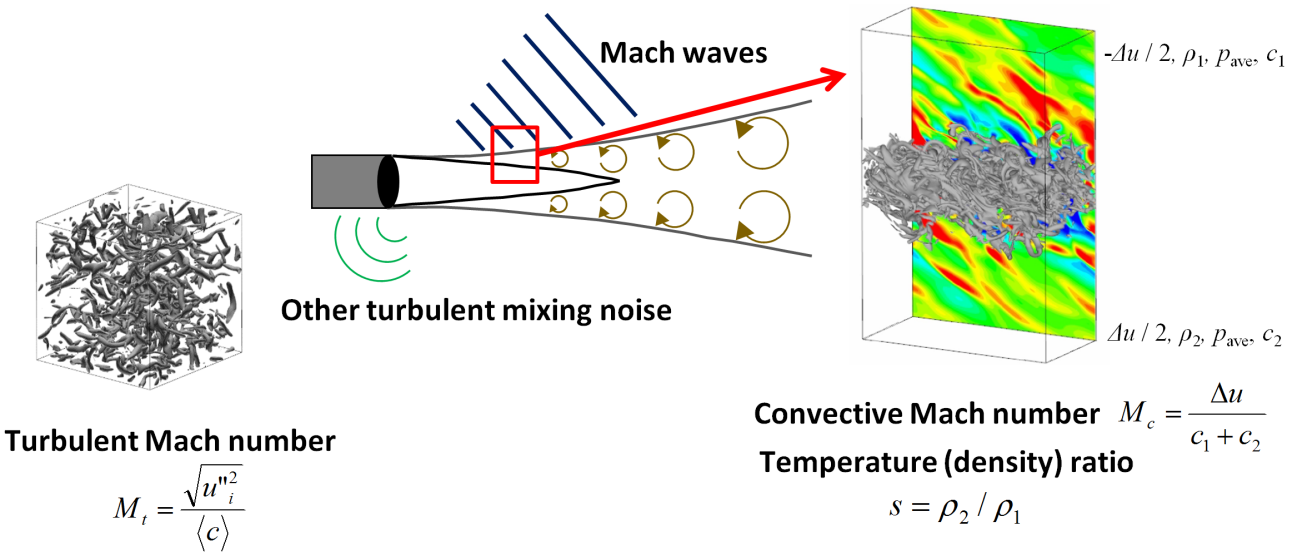

Figure 1.7: Present approach to understand the parameter dependence on supersonic jet noise.

1.3 Previous Studies of Compressible Turbulent Flows

We conduct DNS of the compressible turbulent flows to understand the Mach number and the temperature ratio dependence on supersonic jet noise. There are two types in the studies of compressible turbulent flows. One is for the turbulent structures, and the other is for the acoustic waves. The previous studies of turbulent structures are introduced at first, and then, those of acoustic waves are discussed.

1.3.1 Turbulent structures

In moderate to high turbulent Mach number flows, it is known that shocklets are generated when flows become locally supersonic (Fig. 1.8). The existence of shocklets was firstly reported by Passot and Pouquet[47] in two-dimensions, and later reported in three-dimensions[48]. Although the regions of shocklets are only a few percent of the total volume[5, 49], they strongly affect the properties of turbulence. Lee *et al.*[48] conducted DNS of the isotropic decaying compressible turbulence and confirmed that the properties of shocklets are the same as those of shock waves. They demonstrated that the compressible dissipation around shocklets is ten times larger than the typical values in incompressible turbulence. This is because, in shocklets regions, the pressure is highly correlated with dilatation to convert the kinetic energy to the internal energy. Shocklets have large impacts on the dynamics of the enstrophy or vorticity, and the suppression of the overall enstrophy production is remarkable once the Mach number becomes high enough for shocklets to appear [49]. However, shocklets also have a role to intensify the enstrophy production [50, 51]. Also, shocklets change the tear drop shape of the joint probability density function (JPDF) of the second and third invariants of the velocity gradient tensor to a longer tail one compared to those for incompressible turbulence[49, 52]. These previous studies clearly demonstrated that the occurrence of shocklets changes flow fields significantly.

The other important change in flows depending on the Mach number is decreased shear layer growth rate. The convective Mach number $M_c = \Delta u/(c_1 + c_2)$ proposed by Papamoschou and Roshko[7] has been used by a lot of studies as a parameter to determine the effects of compressibility in the shear layer where Δu is the velocity difference between two streams, c_1 and c_2 are the speeds of sound at the upper and lower streams, respectively. Fig. 1.9 shows the decrease of the shear layer growth rate with increasing the convective Mach number. A lot of studies were conducted to understand the reasons. The first attempt for the explanation was using pressure-dilatation term[53, 54]. At the higher turbulent Mach number flows, the magnitude of pressure-dilatation term

(a) (b)

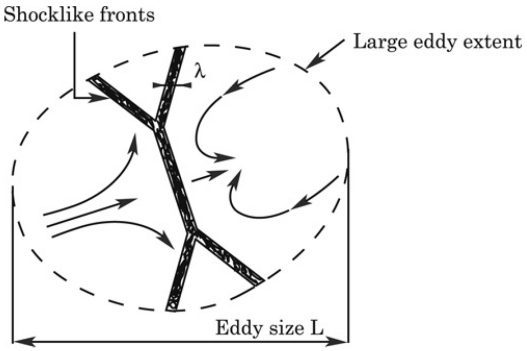

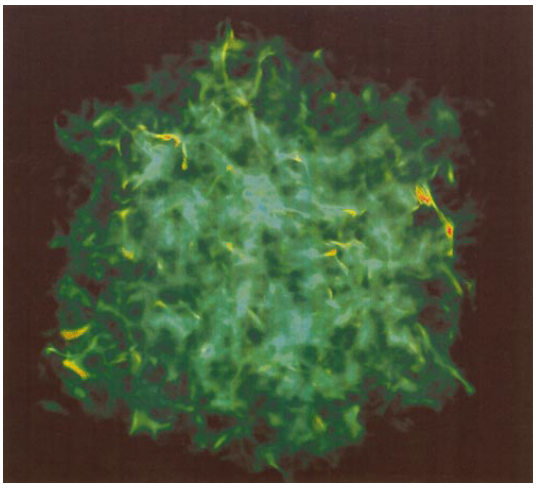

Figure 1.8: (a) Schematic of shocklets[4] and (b) shocklets in an isotropic compressible turbulence[5]. (b) shows volume rendering of dilatation.

is larger due to the existence of eddy shocklets, so that it could cause the decreased turbulent production and decreased growth rate. The later study, however, reported that the decreased growth rate is caused by the decreased kinetic energy, and not by the pressure-dilatation term[55]. Moreover, Vreman *et al.*[56] showed that the decreased pressure-strain term is the main reason for the decreased growth rate by their DNS of the temporally evolving compressible mixing layer. The explanation was also supported by DNS of the annular mixing layer[57]. In addition, Pantano and Sarkar[6] successfully explained the decreased pressure-strain term, and then decreased growth rate with increasing the convective Mach number. They also showed that the shear layer growth rate is decreased with increasing the density ratio because of the shift of the peak shear stress to the lower density side. In addition to the decreased growth rate, the decrease of the transverse length scale of the mixing layer was reported with increasing the convective Mach number[57].

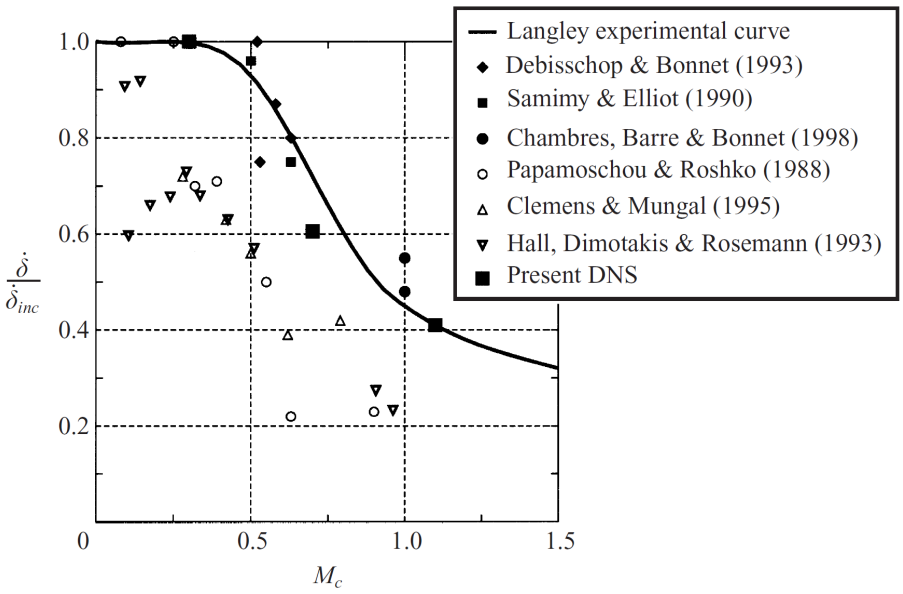

Figure 1.9: Convective Mach number dependence on the mixing layer growth rate[6].

1.3.2 Acoustic waves generated from compressible turbulence

Although, fewer studies were conducted compared with the studies of turbulent structures, some studies for the acoustic waves from compressible turbulent flows were reported. To begin with, the studies of the lower Mach number flows are introduced. Sarkar *et al.* [58] conducted DNS of the isotropic compressible turbulence and analyzed radiated noise from the turbulence at very low turbulent Mach number of 0.05. They showed that the obtained acoustic power agree with the proportionality which is derived theoretically by Proudman[59]. Choi *et al.*[60] conducted DNS of the temporally evolving compressible mixing layer of $M_c = 0.2$ in a transitional state to investigate the characteristics of the source terms of the Lighthill equation[12] and showed that the entropy term is comparable to the Reynolds stress term due to the large dissipation around vortices even in low Mach number flows. Colonius *et al.*[61] conducted two-dimensional DNS of the spatially evolving mixing layer for two stream Mach numbers of $M_1 = 0.05$ and $M_2 = 0.2$. They showed that the acoustic waves have some super-directive properties despite the low Mach number and supported that the theory of modulated wave packets[62]. Some studies in moderate to high Mach number cases were also investigated. Avital *et al.* [63, 64] conducted DNS of a transitional temporally evolving mixing layer at supersonic convective Mach numbers and showed that two types of Mach waves were observed in the transition. However, it was pointed out that the validity of the results were questionable due to the insufficient computational domain[65]. Kleinman *et al.*[65] performed DNS of the temporally evolving compressible mixing layer of $M_c = 0.45$ and showed that the far field pressure spectra collapse well with the scaling of the Taylor micro scale at different Reynolds number cases. In addition, recently, DNS of high convective Mach number ($M_c = 0.75 - 1.75$) mixing layer was performed and showed that characteristics of crackle appear for $M_c > 1.25$. The results implied that the non-linear merging occurs for crackle cases. Although, those previous studies showed that the studies of compressible turbulent flows provide valuable knowledge for the characteristics of acoustic waves, still only few studies were done compared with those of flow structures. Also, how the change in flows connects the sound sources have not been well understood. In order to resolve the problem, we compute the source terms of the Lighthill equation[12] by the results of DNS as in the previous study by Choi *et al*[60]. Their study only focused on the lower convective Mach number flow, whereas our study also apply the method to the higher Mach number and the variable temperature ratio cases. It would support us to understand the connection between change in flows and the sound generation process. Though, non-linear propagation effects should be taken in account

in the higher Mach number flows for the better discussion, the effects are small except for very far field[57, 38, 66]. In addition, even in high convective Mach number cases, the difference in pressure fluctuation with assumed isentropic pressure was shown to be small[20]. Those facts suggest that the Lighthill equation can be used for the qualitative discussion of the sound sources for the higher Mach number cases.

1.4 Objectives

A lot of knowledge of supersonic jet noise has revealed from the previous studies experimentally, theoretically and numerically. However, the understanding of the underling physics is still insufficient, regardless of the significant effects of parameters of the Mach numbers and the temperature ratio on the acoustic wave characteristics. The recent advancement of the computational technique and machine power increase the capability to understand the relationship between flows and sound sources with high resolution computational data. We conduct DNS of the simplified model of the isotropic compressible turbulence and the temporally evolving compressible mixing layer. The choice enables us to focus on the pure parameter dependence of the Mach numbers and temperature ratio without considering the effects of nozzle, resolution, and inflow condition and to save the computational costs for a parametric study. In order to understand the relationship between the change in flows and the sound generation process, the source terms of the Lighthill equation are used to support the discussion. In the present study, we focus on the turbulent mixing noise due to its importance. The points to focus in the present thesis are stated as follows.

Turbulent Mach number dependence

In the turbulent mixing noise, the properties of turbulent fluctuation should be one of the most important factors. For the discussion, the turbulent Mach number can be a suitable parameter. At higher turbulent Mach numbers, shocklets generate and affect the flow field significantly, so that they would change the sound source characteristics. We analyze the various turbulent Mach numbers by DNS of the isotropic compressible turbulence and discuss the change in the sound source characteristics.

Convective Mach number and temperature ratio dependence

The decreased shear layer growth rate with increasing the convective Mach number and the temperature ratio were discussed for a long period. Also, the decreased transverse

length scale with increasing the convective Mach number was shown in the previous study. However, how those changes in flows affect the sound sources have not been well understood. We conduct DNS of the temporally evolving compressible mixing layer and investigate the convective Mach number and the density ratio (corresponds to temperature ratio) dependence. The acoustic wave characteristics of the strength, radiation angle, spectra and non-linearity are discussed in addition to the sound source characteristics.

1.5 Outline of this thesis

The outline of this thesis is as follows. In chapter 2, the problem settings of the isotropic compressible turbulence and the temporally evolving compressible mixing layer are addressed. The initial condition to simulate the turbulent flows and the treatment of the boundary are described. In chapter 3, governing equation, applied numerical methods are introduced. In chapter 4, the turbulent Mach number dependence by DNS of the isotropic compressible turbulence is discussed. Firstly, the determination of time for comparison of the simulated cases and verification of the present computation are conducted. Then, the change in sound source characteristics with various turbulent Mach numbers is discussed. In chapter 5, the convective Mach number and the density ratio (temperature ratio) dependence on the sound source and acoustic wave characteristics are discussed by conducting DNS of the temporally evolving compressible mixing layer. Firstly, the determination of time for comparison results and the validation are conducted. After that, the convective Mach number dependence are discussed by fixing the density ratio to be unity. Then, the density ratio dependence is investigated with a fixed convective Mach number of 1.5. In chapter 5, the characteristics of acoustic waves at a distance from the center of mixing layer are analyzed in addition to the sound source characteristics toward the understanding the far field acoustic wave characteristics. Chapter 6 summarizes the obtained the results and draws conclusions.

Chapter 2

Problem Settings

In the present study, two fundamental compressible turbulent flows are simulated. At first, the isotropic compressible turbulence is explained, and then, the temporally evolving compressible mixing layer is introduced.

2.1 Isotropic compressible turbulence

A three-dimensional decaying isotropic compressible turbulence is simulated (Fig. 2.1). Turbulent fluctuations whose spectrum is a final state of decaying turbulence are given for the initial condition. Turbulence is freely decaying from the initial state to a quasi steady state in the cubic box of 2π. The periodic boundary conditions are imposed for all directions. The isotropic compressible turbulence is characterized by two important parameters of the turbulent Mach number and the Taylor micro scale Reynolds number, so that those parameters are introduced in the next subsection. Also, the initial condition which takes one of the most important roles in the simulation is introduced subsequently.

2.1.1 Turbulent Mach number and Taylor micro scale Reynolds number

The turbulent Mach number is defined based on the magnitude of the velocity fluctuation $\sqrt{u_i^2}$ and the average value of the speed of sound c:

$$M_t = \frac{\sqrt{< u_i^2 >}}{< c >}, \tag{2.1}$$

where $< \cdot >$ denotes the spatial average. The values of the turbulent Mach number are highly depending on the small scale turbulent fluctuations, so that the effects of

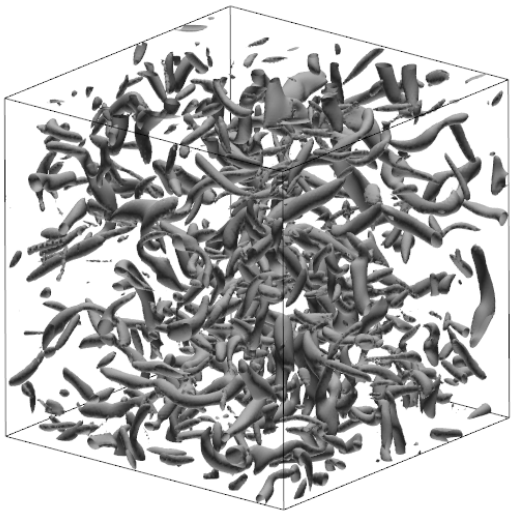

Figure 2.1: A simulation result of the decaying isotropic compressible turbulence. The iso-surface is the second invariant of the velocity gradient tensor.

small scale turbulent fluctuations can be investigated. Note that the convective Mach number in the temporally evolving compressible mixing layer is related with the large scale turbulent motion. It is worth noting that the existence of shocklets are reported for moderate to high turbulent Mach numbers and the typical critical turbulent Mach number for the occurrence of shocklets is around $M_{t0} = 0.4$[48, 5, 49]. Note that M_{t0} is the initial turbulent Mach number. The range of simulated turbulent Mach number is $M_{t0} = 0.2 - 1.0$, so that the effects of the turbulent Mach number including the effects of shocklets on sound source characteristics can be investigated.

For the Reynolds number, the Reynolds number based on the Taylor micro scale R_λ is often used. The Reynolds number is defined as;

$$R_\lambda = \frac{<\rho>\sqrt{<u_i^2/3>}\lambda}{<\mu>} \tag{2.2}$$

in which ρ and μ are density and viscosity, respectively. The Taylor micro scale λ is defined as follows:

$$\lambda = \sqrt{\frac{<u_i^2/3>}{<(\partial u_i/\partial x_i)^2/3>}}. \tag{2.3}$$

The derivation of the Taylor micro scale is found in App. C. We set the initially three different Taylor micro scale Reynolds numbers of 130, 100 and 70 to understand the Reynolds number effects. $R_{\lambda 0} = 130$ is used for the most discussion.

2.1.2 Initial condition

An initially solenoidal and isentropic fluctuation is used in the present simulation. Note that some initial condition dependence are reported in the isotropic decaying compressible turbulence[67, 68, 50, 69, 5, 49, 70]. One reason for choosing the initial condition is to check whether the entropy term in the Lighthill equation which is often neglected in low Mach numbers can be actually negligible or not. The turbulent motion could generate entropy term even in low Mach number flow[60]. The discussion for neglecting the entropy term is given by assuming isentropic condition. We try to exclude the possibility that the non-uniformity of entropy is generated by the initial condition. A recent DNS of the two-dimensional decaying isotropic compressible turbulence for low turbulent Mach numbers showed that the initially solenoidal, uniform entropy case maintain almost uniform entropic flow, whereas the initially solenoidal, non-unifrom entropy case changes the scaling of density[70]. The results suggested that the initially solenoidal, isentropic conditions are preferable not to contaminate the assumption of the low Mach number flows by at least the initial condition. If the assumption is no longer applied after a period of the simulation with the initial condition, the resulting non-uniform entropy field should be caused by the turbulent motion, not by the initial condition. Also, the initial condition would change the critical turbulent Mach number for generating shocklets and the strength of shocklets[50, 49, 70], but the characteristics of shocklets themselves are not changed. Therefore, the conclusions for the effects of shocklets on sound sources can be discussed without considering of the effects of the initial condition. The brief procedure for generating the initial fluctuation is as follows:

1. Velocity is determined to satisfy the spectra of a final state of decaying turbulence.
2. The compressive component of velocity is subtracted by the given velocity field above.
3. Pressure and density fluctuations are determined by a Poisson equation derived by assuming isentropic and selenoidal conditions.

To begin with, a energy spectrum of a final state of the decaying turbulence is considered:

$$E(k) \sim k^4 \exp\Big(-2\frac{k^2}{k_{\mathrm{peak}}^2}\Big), \tag{2.4}$$

where k is the magnitude of the wave number in space and k_{peak} is its peak value. The value k^4 is multiplied for k_{peak} to be the peak wave number. In the present simulation,

the peak wave number is set to be $k_{\text{peak}} = \sqrt{10}$. To satisfy the energy spectrum, the velocity in the Fourier space $\hat{\mathbf{u}}$ is determined as follows:

$$\hat{\mathbf{u}} \sim k \exp\Big(-\frac{k^2}{k_{\text{peak}}^2}\Big), \tag{2.5}$$

where the amplitudes and the phases are randomized by a random seed. The solenoidal condition is satisfied by subtracting the compressive component $\hat{\mathbf{u}}_c$ written as;

$$\hat{\mathbf{u}}_c = \frac{\mathbf{k} \cdot \mathbf{u}}{|\mathbf{k}|}. \tag{2.6}$$

After the inverse Fourier transform, the solenoidal velocity field is obtained. The amplitudes of the given velocity filed are adjusted depending on the initial turbulent Mach numbers.

The pressure and density fluctuations (p' and ρ') are determined by a Poisson equation as follows[70]:

$$\nabla^2\Big(\frac{p'}{\rho'}\Big) = -\frac{\gamma - 1}{\gamma}\frac{\partial^2(u_i u_j)}{\partial x_i \partial x_j}, \tag{2.7}$$

The Poisson equation is derived by the divergence of the momentum equation by assuming solenoidal and isentropic flows[5]. Here, the viscous term is neglected in (Eq. 2.7). The Poisson equation is solved with the isentropic relation $p'/(\rho')^\gamma = p_{\text{ref}}/(\rho)_{\text{ref}}^\gamma = 1/\gamma$, where p_{ref} and ρ_{ref} is the reference values of pressure and density.

2.2 Temporally evolving compressible mixing layer

The schematic of the temporally evolving compressible mixing layer is shown in Fig. 2.2. The computational domain is $L_x \times L_y \times L_z = 343 \times 86 \times 692$. The flow develops temporally to the transverse directions. The periodic boundary conditions are imposed in the streamwise and spanwise directions. The boundaries of the transverse direction are set to be very far to avoid the reflection of spurious acoustic waves. Two important parameters of the convective Mach number M_c and the density ratio s in the temporally evolving compressible mixing layer are explained in the following subsection. Also, the Reynolds number based on the momentum thickness is introduced. The initial condition for the present simulation is explained afterwards.

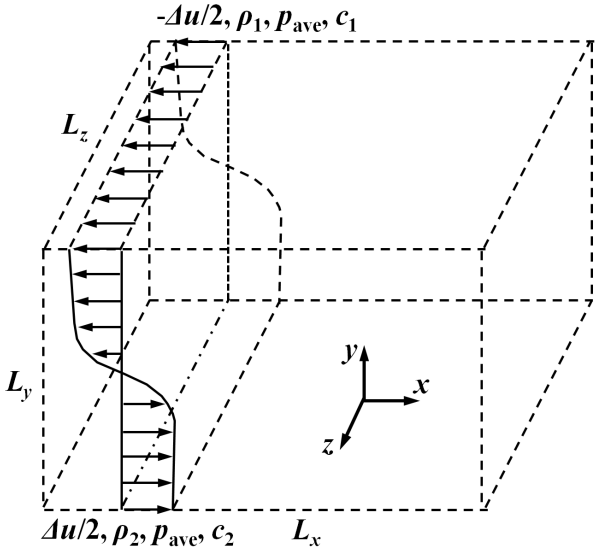

Figure 2.2: Schematic of temporally evolving compressible mixing layer.

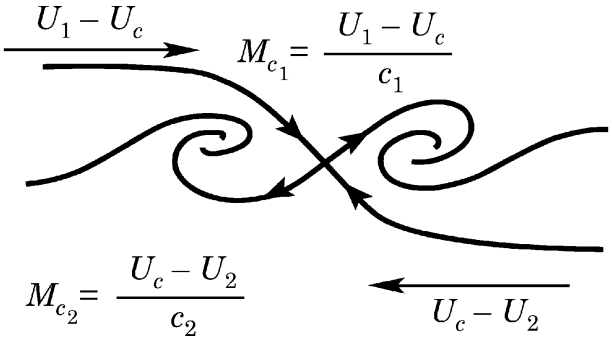

Figure 2.3: Schematic figure of the turbulent mixing layer in the convective frame of reference moving with convective velocity U_c[7].

2.2.1 Convective Mach number, density ratio and Reynolds number

The convective Mach number M_c is a popular choice to determine the compressibility in the shear layer and defined as;

$$M_c = \frac{\Delta u}{c_1 + c_2}, \tag{2.8}$$

where Δu is the velocity difference between the upper and lower streams, whereas c_1 and c_2 are the speeds of sound at the upper and lower streams. The derivation is briefly described in the following[7]. Fig. 2.3 shows the schematic figure of the mixing layer in the convective frame of reference moving with the convective velocity U_c. The Mach

number at the upper stream M_{c1} and the lower stream M_{c2} are defined as follows:

$$M_{c_1} = \frac{U_1 - U_c}{c_1},$$
$$M_{c_2} = \frac{U_c - U_2}{c_2}, \tag{2.9}$$

where U_1 and U_2 are the velocities at the upper and lower streams, respectively. If the flow is assumed to be steady and isentropic, the static pressures of two streams are equal:

$$\left(1 + \frac{\gamma_1 - 1}{2} M_{c_1}\right)^{\frac{\gamma_1}{\gamma_1 - 1}} = \left(1 + \frac{\gamma_2 - 1}{2} M_{c_2}^2\right)^{\frac{\gamma_2}{\gamma_2 - 1}}, \tag{2.10}$$

where γ_1 and γ_2 are the ratio of specific heats at the upper and lower streams, respectively. Note that the the assumption comes from the existence of the saddle point (corresponds to a stagnation point) between two streams in the convective frame. Assuming $\gamma_1 = \gamma_2$, (Eq. 2.10) is written in;

$$M_{c_1} = M_{c_2} (= M_c). \tag{2.11}$$

Substituting (Eq. 2.9) into (Eq. 2.11), the convective velocity U_c is given as;

$$U_c = \frac{c_1 U_2 + c_2 U_1}{c_1 + c_2}. \tag{2.12}$$

Then, we have the final form of the convective Mach number M_c as follows:

$$\begin{aligned} M_c = M_{c_1} &= \frac{U_1 - \frac{c_1 U_2 + c_2 U_1}{c_1 + c_2}}{c_1} \\ &= \frac{U_1 - U_2}{c_1 + c_2} \\ &= \frac{\Delta u}{c_1 + c_2}. \end{aligned} \tag{2.13}$$

Note that the flow direction of the present setup of the mixing layer (Fig. 2.2) is opposite to the discussion above, but the the same form of the convective Mach number is derived by setting the subscripts to be $2 \to 1$ and $1 \to 2$.

The fact that the decreased mixing layer growth rate was explained as the function of the convective Mach number[6] showed that the convective Mach number is a very important parameter to characterize the shear layer, i.e. large scale flow structures. The change in sound sources and generated acoustic waves are discussed with different convective Mach numbers. Our focus is on supersonic jet noise, so that the values of the convective

Mach number are set to be $1.2 - 1.8$. In isothermal jets, the convective Mach number is the half of the jet Mach number[71], so that the corresponding jet Mach numbers are the range $2.4 - 3.6$ which covers the various applications of supersonic jets from supersonic aircrafts to rockets. Note that the convective Mach number dependence is investigated using the isothermal mixing layer as explained later. Density ratio s is also an important parameter and defined as;

$$s = \frac{\rho_1}{\rho_2}. \tag{2.14}$$

In the temporally evolving compressible mixing layer, the pressures at the upper and lower streams are the same, so that density ratio corresponds to the temperature ratio which is very important for hot jets. The density ratio (temperature ratio) is also known as an important parameter to determine the decreased mixing layer growth rate[6]. The temperature effects are investigated with various density ratios $s = 1 - 8$. It is worth noting that the temperature ratio of a sub-scale liquid rocket motor is 6.48[3], so that the range $s = 1 - 8$ covers such an extreme case. For the discussion of the effects of the convective Mach number, we consider the isothermal mixing layer, i.e. $s = 1$. For the effects of the density ratio, on the other hand, we fix the convective Mach number to be 1.5 and discuss the effects of density (temperature) ratio on the sound source and acoustic wave characteristics.

In the present simulation, we use the Reynolds number based on the momentum thickness defined as;

$$Re_\theta = \frac{\rho_{\rm ave}\Delta u \delta_\theta}{\mu_{\rm ave}}, \tag{2.15}$$

where $\rho_{\rm ave} = (\rho_1 + \rho_2)/2$ and $\mu_{\rm ave} = (\mu_1 + \mu_2)/2$ are averaged density and viscosity of the upper and lower streams. The momentum thickness δ_θ is defined as follows:

$$\delta_\theta = \frac{1}{\rho_{\rm ave}\Delta u^2}\int_{-L_y/2}^{L_y/2} \bar{\rho}\Big(\frac{1}{2}\Delta u - \tilde{u}_1\Big)\Big(\frac{1}{2}\Delta u + \tilde{u}_1\Big)dx_2, \tag{2.16}$$

where $\tilde{()}$ and $\bar{()}$ denote the Favre and Reynolds averages. The initial Reynolds number based on the momentum thickness $R_{\theta 0}$ is set to be the similar value 154.2 with the previous DNS by Pantano and Sarkar[6].

2.2.2 Initial condition

We follow the similar procedure of the previous DNS by Pantano and Sarkar[6]. The velocity profile is given by a hyperbolic tangent profile:

$$\bar{u}_1(y) = \frac{\Delta u}{2}\tanh\left(-\frac{y}{2\delta_{\theta 0}}\right), \bar{u}_2 = 0, \bar{u}_3 = 0, \tag{2.17}$$

where $\delta_{\theta 0}$ is the initial momentum thickness. The mean density profile is also determined by the following hyperbolic tangent profile:

$$\bar{\rho}(y) = \rho_{\text{ave}}\left(1 + \lambda(s)\tanh\left(-\frac{y}{2\delta_{\theta 0}}\right)\right), \tag{2.18}$$

where $\lambda(s) = (s-1)/(s+1)$. To trigger turbulence we impose the same initial fluctuation with that of the isotropic compressible turbulent simulation. The initial turbulent intensity is set to be 10% of the velocity difference Δu. The isotropic fluctuations are limited in the y direction by an exponential decay of the form[72]:

$$\exp\left(-\frac{x_2}{2\delta_{\theta 0}}\right). \tag{2.19}$$

Chapter 3

Numerical Methods

The numerical methods used in the present study are described. Our focus in the present study is to investigate the pure parameter dependence on sound sources and radiated acoustic waves in supersonic jets. To achieve the objectives, the direct numerical simulations of the isotropic compressible turbulence and the temporally evolving compressible mixing layer are conducted. This approach helps us to investigate the underlying physics without considering uncertainties such as inflow condition, nozzle, resolution and turbulence model. In the following sections, firstly, the governing equation is described. Then, the spatial difference scheme with shock-capturing and the time integration scheme are presented. After the explanation of the numerical schemes, the boundary conditions are explained.

3.1 Governing Equation

The three-dimensional compressible Navier-Stokes equations in the conservation form are written as;

$$\frac{\partial Q}{\partial t} + \frac{\partial E}{\partial x} + \frac{\partial F}{\partial y} + \frac{\partial G}{\partial z} = \frac{\partial E_v}{\partial x} + \frac{\partial F_v}{\partial y} + \frac{\partial G_v}{\partial z}, \tag{3.1}$$

$$
\begin{aligned}
Q &= (\rho, \rho u, \rho v, \rho w, e)^T, \\
E &= (\rho u, \rho u^2 + p, \rho uv, \rho uw, (e+p)u)^T, \\
F &= (\rho v, \rho vu, \rho v^2 + p, \rho vw, (e+p)v)^T, \\
G &= (\rho w, \rho wu, \rho wv, \rho w^2 + p, (e+p)w)^T, \\
E_v &= (0, \tau_{xx}, \tau_{xy}, \tau_{xz}, \beta_x), \\
F_v &= (0, \tau_{yx}, \tau_{yy}, \tau_{yz}, \beta_y), \\
G_v &= (0, \tau_{zx}, \tau_{zy}, \tau_{zz}, \beta_z),
\end{aligned} \tag{3.2}
$$

$$
\begin{aligned}
\beta_x &= \tau_{xx}u + \tau_{xy}v + \tau_{xz} - q_x, \\
\beta_y &= \tau_{yx}u + \tau_{yy}v + \tau_{yz} - q_y, \\
\beta_z &= \tau_{zx}u + \tau_{zy}v + \tau_{zz} - q_z,
\end{aligned}
$$

where e, τ_{ij}, q_i is the total energy per unit volume, viscous stress tensor and heat flux, respectively. For an ideal state of gas, the total energy per unit volume e satisfies the following equation:

$$
\rho e = \frac{1}{\gamma - 1} p + \frac{1}{2}\rho(u^2 + v^2 + w^2), \tag{3.3}
$$

in which γ is the ratio of specific heats. With Stokes's hypothesis, the viscous stress tensor τ_{ij} is written as follows:

$$
\tau_{ij} = \mu\Big(\frac{\partial u_i}{\partial x_j} + \frac{\partial u_j}{\partial x_i} - \frac{2}{3}\delta_{ij}\frac{\partial u_k}{\partial x_k}\Big). \tag{3.4}
$$

The viscous coefficient μ is determined by the Sutherland's law:

$$
\frac{\mu}{\mu_{\text{ref}}} = \Big(\frac{T}{T_{\text{ref}}}\Big)^{3/2}\Big(\frac{(1+T_1)/T_{\text{ref}}}{(T+T_1)/T_{\text{ref}}}\Big), \tag{3.5}
$$

where T_1 and T_{ref} are 110.6 and 293.7, respectively. Also, μ_{ref} is determined by the Reynolds number explained in the following subsection. The heat flux q_i is defined by the Fourier's law:

$$
q_i = -\kappa\frac{\partial T}{\partial x_i}, \quad (i = 1, 2, 3), \tag{3.6}
$$

where κ is the thermal conductivity. The equation is rewritten with the Prandtl number Pr and the speed of sound c in the ideal state of gas:

$$Pr = \frac{c_p \mu}{\kappa}, \tag{3.7}$$

$$c = \sqrt{\gamma RT} = \sqrt{\frac{\gamma p}{\rho}}, \tag{3.8}$$

where c_p is the specific heat at constant pressure and R is the gas constant, respectively. In the ideal state of gas, the specific heat at constant pressure is written as;

$$c_p = \frac{\gamma R}{\gamma - 1}. \tag{3.9}$$

With those relations, the final form of the heat flux q_i is derived as follows:

$$q_i = -\frac{1}{\gamma - 1} \frac{\mu}{Pr} \frac{\partial c^2}{\partial x_i}, \tag{3.10}$$

where the Prandtl number Pr is set to be 0.72 in the present computation.

3.1.1 Non-dimensionalization of Navier-Stokes Equations

The non-dimensional form of the Navier-Stokes equations is used for the actual computation. In the present study, the non-dimensionalization is conducted by using the reference values of density ρ_{ref}, speed of sound c_{ref}, and length scale L_{ref}:

$$\rho^* = \frac{\rho}{\rho_{\text{ref}}}, c^* = \frac{c}{c_{\text{ref}}}, L^* = \frac{L}{L_{\text{ref}}}, \tag{3.11}$$

where astarisk shows non-dimensional quantities. Those operations derive the following non-dimensionalized Navier-Stokes equations:

$$\frac{\partial Q^*}{\partial t^*} + \frac{\partial E^*}{\partial x^*} + \frac{\partial F^*}{\partial y^*} + \frac{\partial G^*}{\partial z^*} = \frac{M}{Re}\Big(\frac{\partial E_v^*}{\partial x^*} + \frac{\partial F_v^*}{\partial y^*} + \frac{\partial G_v^*}{\partial z^*}\Big), \tag{3.12}$$

$$
\begin{aligned}
Q^* &= (\rho^*, \rho^* u^*, \rho^* v^*, \rho^* w^*, e^*)^T, \\
E^* &= (\rho^* u^*, \rho^* u^{*2} + p^*, \rho^* u^* v^*, \rho^* u^* w^*, (e^* + p^*) u^*)^T, \\
F^* &= (\rho^* v^*, \rho^* v^* u^*, \rho^* v^{*2} + p^*, \rho^* v^* w^*, (e^* + p^*) v^*)^T, \\
G^* &= (\rho^* w^*, \rho^* w^* u^*, \rho^* w^* v^*, \rho^* w^{*2} + p^*, (e^* + p^*) w^*)^T, \\
E_v^* &= (0, \tau_{xx}^*, \tau_{xy}^*, \tau_{xz}^*, \beta_x^*), \\
F_v^* &= (0, \tau_{yx}^*, \tau_{yy}^*, \tau_{yz}^*, \beta_y^*), \\
G_v^* &= (0, \tau_{zx}^*, \tau_{zy}^*, \tau_{zz}^*, \beta_z^*),
\end{aligned} \tag{3.13}
$$

$$
\begin{aligned}
\beta_x^* &= \tau_{xx}^* u^* + \tau_{xy}^* v^* + \tau_{xz}^* - q_x^*, \\
\beta_y^* &= \tau_{yx}^* u^* + \tau_{yy}^* v^* + \tau_{yz}^* - q_y^*, \\
\beta_z^* &= \tau_{zx}^* u^* + \tau_{zy}^* v^* + \tau_{zz}^* - q_z^*,
\end{aligned}
$$

where

$$
x_i^* = \frac{x_i}{L_{\text{ref}}}, t^* = \frac{t}{L_{\text{ref}}/c_{\text{ref}}}, u_i^* = \frac{u_i}{c_{\text{ref}}}, e^* = \frac{e}{\rho_{\text{ref}} c_{\text{ref}}^2}, p^* = \frac{p}{\rho_{\text{ref}} c_{\text{ref}}^2} = \frac{p}{\gamma p_{\text{ref}}},
$$

$$
\mu^* = \frac{\mu}{\mu_{\text{ref}}}, \tau_{ij}^* = \frac{\tau_{ij}}{\mu_{\text{ref}} c_{\text{ref}}/L_{\text{ref}}}, q_i^* = \frac{q_i}{\mu_{\text{ref}} c_{\text{ref}}^2/L_{\text{ref}}}. \tag{3.14}
$$

Also, the Reynolds number Re and Mach number M are defined as follows:

$$
Re = \frac{\rho_{\text{ref}} u_{\text{ref}} L_{\text{ref}}}{\mu_{\text{ref}}}, M = \frac{u_{\text{ref}}}{c_{\text{ref}}}. \tag{3.15}
$$

3.2 Numerical Schemes

3.2.1 Spacial Difference Scheme

The central difference scheme is preferable to solve turbulent flows due to its non-dissipative properties. It is known that, however, the numerical instability occurs when a standard central finite difference scheme is used without any viscosity. One possible solution to resolve the issue is to stabilize the computation by quadratic invariants preservation which corresponds to the kinetic energy conservation for incompressible flows. The skew-symmetric splitting scheme is constructed based on the idea of the quadratic in-

variants preservation, and preserve the kinetic energy at the semi-discrete level. A form of the skew-symmetric scheme used in the present computation is explained. In addition, our study needs to consider turbulent flows with weak shock waves, i.e. shocklets, because our target is high speed turbulent flows. Thus, the method of shock capturing is described after introducing the skew-symmetric splitting scheme.

Skew-symmetric splitting scheme

The discussion starts with the following Euler equation:

$$\frac{\partial Q}{\partial t}+\frac{\partial E}{\partial x}+\frac{\partial F}{\partial y}+\frac{\partial G}{\partial z}=0, \tag{3.16}$$

$$\begin{aligned} Q &= (\rho,\rho u,\rho v,\rho w,e)^T,\\ E &= (\rho u,\rho u^2+p,\rho uv,\rho uw,(e+p)u)^T,\\ F &= (\rho v,\rho vu,\rho v^2+p,\rho vw,(e+p)v)^T,\\ G &= (\rho w,\rho wu,\rho wv,\rho w^2+p,(e+p)w)^T. \end{aligned} \tag{3.17}$$

If the pressure force is disregarded, the equation for any components of the vector can be written as;

$$\frac{\partial \rho\phi}{\partial t}+\frac{\partial}{\partial x_i}(\rho u_i\phi)=0, \tag{3.18}$$

where ϕ is a general transport scalar. Here, two splitting forms of the convective derivative are introduced:

1. FE splitting form[73]

$$\frac{\partial u_i\phi}{\partial x_i}=\frac{1}{2}\frac{\partial \rho u_i\phi}{\partial x_i}+\frac{1}{2}\phi\frac{\partial \rho u_i}{\partial x_i}+\frac{1}{2}\rho u_i\frac{\partial \phi}{\partial x_i}. \tag{3.19}$$

2. KG splitting form[74, 75]

$$\begin{aligned} \frac{\partial u_i\phi}{\partial x_i} &= \alpha\frac{\partial \rho u_i\phi}{\partial x_i}+\beta\Big(u_i\frac{\partial \rho\phi}{\partial x_i}+\rho\frac{\partial u_i\phi}{\partial x_i}+\phi\frac{\partial \rho u_i}{\partial x_i}\Big)\\ &\quad+(1-\alpha-2\beta)\Big(\rho u_i\frac{\partial \phi}{\partial x_i}+\rho\phi\frac{\partial u_i}{\partial x_i}+u_i\phi\frac{\partial \rho}{\partial x_i}\Big), \end{aligned} \tag{3.20}$$

where α,β are free parameters.

The above two splitting forms preserve kinetic energy at the semi-discrete level. Note that the kinetic energy preservation in KG form is achieved only for $\alpha = 1/4, \beta = 1/4$. For simplicity, the kinetic energy preservation in FE splitting form is shown by following the explanation of Pirozolli[75]. Similar discussion can be applied to KG form. Before the discussion, the discretization rule is introduced. For the discretization, the explicit central approximation for the general function f in the ith direction is considered:

$$D_i f_X = \sum_{l=1}^{L} a_l (f_{i;l} - f_{i;-l})_X, \tag{3.21}$$

where $X \equiv (x_1, ..., x_d)$ represents grid node and $(f_{i;l})_X$ is simple notation for the shift defined as;

$$(f_{i;l})_X = f_{x_1,...,x_{i+l},...,x_d}. \tag{3.22}$$

a_l are determined depending on the formal order of accuracy, so that the order of accuracy is $2L$ for a given stencil half-width L. Then, the kinetic energy preservation at the semi-discrete level is shown as follows. Substituting $\phi = 1$ for the continuity equation, and $\phi = u_i$ for the momentum equation into (Eq. 3.19), then equation (Eq. 3.19) is discretized by;

$$\frac{d(\rho)_X}{dt} + D_i(\rho u_i)_X = 0, \tag{3.23}$$

$$\frac{d(\rho u_j)_X}{dt} + \frac{1}{2} D_i(\rho u_i u_j)_X + \frac{1}{2}(u_j)_X D_i(\rho u_i)_X + \frac{1}{2}(\rho u_i)_X D_i(u_j)_X = 0. \tag{3.24}$$

(Eq. 3.23)$\times(u_j)_X$, summing over j, and subtracting (Eq. 3.24)$\times(u_j u_j/2)_X$ derive:

$$\frac{d}{dt}(\frac{\rho u_j u_j}{2})_X + \frac{1}{2}(u_j)_X D_i(\rho u_i u_j)_X + \frac{1}{2}(\rho u_i u_j)_X D_i(u_j)_X = 0. \tag{3.25}$$

By summing (Eq. 3.25) over all grid nodes, the total kinetic energy preservation is achieved. Note that the convective derivative of both FE splitting form and KG splitting forms can be approximated as;

$$\left(\frac{\partial u_i \phi}{\partial x_i}\right)_X \approx \frac{1}{\Delta x}\left(\hat{f}_{i;1/2} - \hat{f}_{i;-1/2}\right)_X, \tag{3.26}$$

where Δx is the grid spacing. Especially, for the KG splitting form, the numerical flux can be written as;

$$\begin{aligned}\hat{f}_{i;1/2} &= 2\sum_{l=1}^{L} a_l \sum_{m=0}^{l-1}\Big(\frac{1}{8}(\rho_{i;-m}+\rho_{i;-m+l})(u_{i;-m}+u_{i;-m+l})(\phi_{i;-m}+\phi_{i;-m+l})\Big) \\ &= \frac{1}{4}\sum_{l=1}^{L} a_l \sum_{m=0}^{l-1}\Big((\rho_{i;-m}+\rho_{i;-m+l})(u_{i;-m}+u_{i;-m+l})(\phi_{i;-m}+\phi_{i;-m+l})\Big). \quad (3.27)\end{aligned}$$

Similarly, the numerical flux of the pressure gradient in the conservative form is derived (not shown here). Applying those formula to the Euler equation, the numerical flux $\hat{F}^{\text{skew}}_{i;1/2}$ is obtained. In the present study, the KG splitting with the sixth order explicit central difference approximation ($L = 3$) is used for the computation.

Shock capturing

In highly compressible turbulent flows, eddy-shocklets appear due to the high level of fluctuations. To solve such complex flow fields, shock capturing scheme providing appropriate dissipation in shock region is necessary. In the present study, the dissipation part of the sixth order central-upwind weighted essentially non-oscillatory (WENOCU) scheme is used for shock capturing with a shock sensor. In no shock region, only the sixth order skew symmetric splitting scheme is used, whereas in shock region, the dissipation part of the sixth order WENOCU[76] scheme is used with the skew symmetric scheme. For detecting shocklets, a sensor similarly with Ducros sensor[77] is used:

$$\Phi = \frac{-\nabla\cdot\mathbf{u}}{|\nabla\cdot\mathbf{u}| + |\omega| + \epsilon}, \quad (3.28)$$

where ω is vorticity, ϵ is very small number to avoid division by zero. For strong shock region, the sensor approaches unity, whereas it approaches to zero in no-shock region, so that the values of adding dissipation is determined depending on the sensor. In the detected shocklets region, the dissipation part of the sixth order WENOCU scheme is added. Here, the sixth order WENOCU scheme and the decomposition into the consistent part and the dissipative term are briefly described. We consider one-dimensional advection equation:

$$\frac{\partial u}{\partial t} + \frac{\partial}{\partial x} f(u) = 0, \quad (3.29)$$

where $\frac{\partial f}{\partial x} > 0$ is assumed for simplicity. The simple notation (Eq. 3.22) is also used here. The convective derivative is approximated in the conservative form as;

$$\left(\frac{\partial f}{\partial x}\right)_X \approx \frac{1}{\Delta x}(\hat{f}_{i;1/2} - \hat{f}_{i;-1/2}). \tag{3.30}$$

For the sixth order WENOCU scheme, the numerical flux $\hat{f}_{i;1/2}$ is constructed by the upwinding fluxes:

$$\hat{f}_{0,i;1/2} = \frac{1}{6}(2f_{i;-2} - 7f_{i;-1} + 11f_{i;0}), \tag{3.31}$$

$$\hat{f}_{1,i;1/2} = \frac{1}{6}(-f_{i;-1} + 5f_{i;0} + 2f_{i;1}), \tag{3.32}$$

$$\hat{f}_{2,i;1/2} = \frac{1}{6}(2f_{i;0} + 5f_{i;1} - f_{i;2}), \tag{3.33}$$

$$\hat{f}_{3,i;1/2} = \frac{1}{6}(11f_{i;1} - 7f_{i;2} + 2f_{i;3}). \tag{3.34}$$

With the upwinding fluxes, $\hat{f}_{i;1/2}$ is reconstructed as follows:

$$\hat{f}_{i;1/2} = \omega_0\hat{f}_{0,i;1/2} + \omega_1\hat{f}_{1,i;1/2} + \omega_2\hat{f}_{2,i;1/2} + \omega_3\hat{f}_{3,i;1/2}, \tag{3.35}$$

where ω_k is non-linear weight and defined by;

$$\omega_k = \frac{\alpha_k}{\alpha_0 + \alpha_1 + \alpha_2 + \alpha_3}, \quad \alpha_k = d_k\left(C + \frac{\tau_6}{\beta_k + \epsilon}\right) \quad (k = 0, 1, 2, 3), \tag{3.36}$$

in which the optimized weight d_k, smoothness indicators β_k, τ_6, adjusting parameter C, and small number ϵ for avoiding division by zero are as follows:

$$
\begin{aligned}
d_0 &= \frac{1}{20}, d_1 = \frac{9}{20}, d_2 = \frac{9}{20}, d_3 = \frac{1}{20}, \\
C &= 20, \\
\beta_0 &= \frac{1}{4}(f_{i;-2} - 4f_{i;-1} + 3f_{i;0})^2 + \frac{13}{12}(f_{i;-2} - 2f_{i;-1} + f_{i;0})^2, \\
\beta_1 &= \frac{1}{4}(f_{i;-1} - f_{i;1})^2 + \frac{13}{12}(f_{i;-1} - 2f_{i;0} + f_{i;1})^2, \\
\beta_2 &= \frac{1}{4}(3f_{i;0} - 4f_{i;1} + f_{i;2})^2 + \frac{13}{12}(f_{i;0} - 2f_{i;1} + f_{i;2})^2, \\
\beta_3 &= \beta_6 \\
&= \frac{1}{120960}\Big[271779f_{i;-2}^2 + \\
&+ f_{i;-2}(2380800f_{i;-1} + 4086352f_{i;0} - 3462252f_{i;1} + 1458762f_{i;2} - 245620f_{i;3}) \\
&+ f_{i;-1}(5653317f_{i;-1} - 20427884f_{i;0} + 17905032f_{i;1} - 7728988f_{i;2} + 1325006f_{i;3}) \\
&+ f_{i;0}(19510972f_{i;0} - 35817664f_{i;1} + 15929912f_{i;2} - 2792660f_{i;3}) \\
&+ f_{i;1}(17195652f_{i;1} - 15880404f_{i;2} + 2863984f_{i;3}) \\
&+ f_{i;2}(3824847f_{i;2} - 1429976f_{i;3}) + 139633f_{i;3}^2\Big], \\
\tau_6 &= \beta_6 - \frac{1}{6}(\beta_0 + 4\beta_1 + \beta_2).
\end{aligned} \tag{3.37}
$$

Note that β_6 is the smoothness indicator of 6 point stencil for the sixth order interpolation and replaced by the original form of β_3. The flux $\hat{f}_{i;1/2}$ can be divided into the consistent part and the dissipation part as follows[78, 33]:

$$
\begin{aligned}
\hat{f}_{i;1/2} &= \underbrace{\frac{1}{60}(\hat{f}_{i;-2} - 8\hat{f}_{i;-1} + 37\hat{f}_{i;0} + 37\hat{f}_{i;1} - 8\hat{f}_{i;2} + \hat{f}_{i;3})}_{\text{consistent part}} \\
&+ \underbrace{\frac{1}{60}\Big((20\omega_0 - 1)f_0''' - (10(\omega_0 + \omega_1) - 5)f_1''' + (1 - 20\omega_3)f_2'''\Big)}_{\textit{dissipation part}},
\end{aligned} \tag{3.38}
$$

where the first term and the second term are the consistent part and the dissipation part, respectively, and f_l''' are as follows:

$$
\begin{aligned}
f_0''' &= f_{i;1} - 3f_{i;0+}3f_{i;-1} - f_{i;-2}, \\
f_1''' &= f_{i;2} - 3f_{i;1} + 3f_{i;0} - f_{i;-1}, \\
f_2''' &= f_{i;3} - 3f_{i;2} + 3f_{i;1} - f_{i;0}.
\end{aligned} \tag{3.39}
$$

The dissipation part has only high order derivatives[33], so that it can be purely behaved as numerical dissipation. We add the term in the detected shocklets region. In the actual computation, the sixth order WENOCU scheme is adopted to the characteristic fields with Roe average and the flux of the dissipation part $\hat{F}^{\text{wenodisp}}_{i;1/2}$ is obtained, where the low dissipation Lax-Friedrichs splitting[79] is used for the flux splitting. Using the fluxes of the skew symmetric scheme $\hat{F}^{\text{skew}}_{i;1/2}$ and the dissipation part $\hat{F}^{\text{wenodisp}}_{i;1/2}$, the numerical flux of the whole region $\hat{F}^{\text{whole}}_{i;1/2}$ is determined as follows:

$$\hat{F}^{\text{whole}}_{i;1/2} = \begin{cases} \hat{F}^{\text{skew}}_{i;1/2} & \text{(for smooth region)} \\ \hat{F}^{\text{skew}}_{i;1/2} + \hat{F}^{\text{wenodisp}}_{i;1/2} & \text{(for shocklets region).} \end{cases} \tag{3.40}$$

3.2.2 Time integration scheme

In the present study, the classical fourth order Runge-Kutta method is used. We start with a differential equation:

$$\frac{\partial \phi}{\partial t} = g(\phi, t). \tag{3.41}$$

$$\tag{3.42}$$

In the Runge-Kutta method, the value at (n+1) time step ϕ^{n+1} is given by the estimated gradients k_l;

$$k_1 = g(\phi^n, t_n), \tag{3.43}$$

$$k_2 = g((\phi^n + \Delta t/2)k_1, t_n + \Delta t/2) \tag{3.44}$$

$$k_3 = g((\phi^n + \Delta t/2)k_2, t_n + \Delta t/2), \tag{3.45}$$

$$k_4 = g((\phi^n + \Delta t)k_3, t_n + \Delta t), \tag{3.46}$$

$$\phi^{n+1} = \phi^n + \frac{\Delta t}{6}(k_1 + 2k_2 + 2k_3 + k_4), \tag{3.47}$$

where Δt is the time step. The final gradient is determined by a weighted average of four gradients $k_1 - k_4$. Each gradient is computed in the following steps:

1. k_1 is the gradient at the present time.

2. k_2 is the gradient at the intermediate point $t_n + \Delta t/2$ which are given by assuming the gradient to be k_1 at $t_n \leq t \leq t_n + \Delta t/2$.

3. k_3 is the recalculated gradient at the intermediate point $t^n + \Delta t/2$ which are given by assuming the gradient to be k_2 at $t_n \leq t \leq t_n + \Delta t/2$.

4. k_4 is the gradient at the next time $(t_n + \Delta t)$ which are given by assuming the gradient to be k_3 at $t_n \leq t \leq t_n + \Delta t$.

3.2.3 Boundary Conditions

Periodic Boundary Condition

The periodic boundary conditions are used in all directions for the isotropic compressible turbulence, and in the streamwise and spanwise directions for the temporally evolving mixing layer. Additional grid points are used in addition to the computational grids. Ten grid points for the isotropic compressible turbulence, and twelve points for the temporally evolving compressible mixing layer are overlapped for the interpolation. The information of flow variables Q in the ith direction are interpolated in the following way:

$$\begin{aligned}
Q_{i=1} &= Q_{i=i_{\max}-i_{\text{sleeve}}+1}, \\
Q_{i=2} &= Q_{i=i_{\max}-i_{\text{sleeve}}+2}, \\
&\vdots \\
Q_{i=i_{\text{sleeve}}/2-1} &= Q_{i=i_{\max}-i_{\text{sleeve}}/2-1}, \\
Q_{i=i_{\text{sleeve}}/2} &= Q_{i=i_{\max}-i_{\text{sleeve}}/2},
\end{aligned} \tag{3.48}$$

$$\begin{aligned}
Q_{i=i_{\max}-i_{\text{sleeve}}/2+1} &= Q_{i=i_{\text{sleeve}}/2+1}, \\
Q_{i=i_{\max}-i_{\text{sleeve}}/2+2} &= Q_{i=i_{\text{sleeve}}/2+2}, \\
&\vdots \\
Q_{i=i_{\max}-1} &= Q_{i=i_{\text{sleeve}}-1}, \\
Q_{i=i_{\max}} &= Q_{i=i_{\text{sleeve}}}.
\end{aligned} \tag{3.49}$$

Note that $i_{\max} = i_{\text{comp}} + i_{\text{sleeve}}$ is the total grid point in the computation, where i_{comp} is the grid point for the computational region and i_{sleeve} is the grid point for the interpolation, so that the index for the computational domain corresponds to $(i_{\text{sleeve}}/2 + 1 \leq i \leq i_{\text{comp}} + i_{\text{sleeve}}/2)$.

Buffer region

For the temporally evolving compressible mixing layer, the boundary for the transverse direction is set to be very far from the computational region. Total 72 grid points for

both upper and lower directions are used. The stretching ratio for the buffer grids are set to be 5% at $|z_{\rm edge}| \leq |z| \leq |z_{\rm edge}| + 20\delta_{\theta 0}$ and 20% at $|z| \geq |z_{\rm edge}| + 20\delta_{\theta 0}$ where $z_{\rm edge}$ is the position at the edge of the computational region and $\delta_{\theta 0}$ is the initial momentum thickness, respectively.

Chapter 4

Sound source characteristics in isotropic compressible turbulence

In this chapter, the turbulent Mach number dependence on sound sources are investigated using the source terms of the Lighthill equation[12] which are numerically computed by DNS results of the isotropic compressible turbulence. Simulation parameters are shown in Tab. 4.1. We compute total 15 cases. The main discussion is conducted by the highest Reynolds number $R_{\lambda 0} = 130$ corresponding to series A, whereas the lower Reynolds number $R_{\lambda 0} = 100$ and $R_{\lambda 0} = 70$ (series B and C) are used to investigate the Reynolds number dependence. Note that A10' and A10" are used for verification study. The normalization is conducted by the root mean square (rms) value of the considered valuable, unless otherwise noted.

4.1 Development of flow and grid sensitivity

The isotropic compressible turbulence decays temporally, so that the determination of the time for comparison between cases is necessary. In the present study, time is normalized by the initial values of large eddy turn over time $\tau = L_I/\sqrt{< u_i^2/3 >}$. The integral scale L_I is defined as;

$$L_I = \frac{3\pi}{2\sqrt{< u_i^2 >}} \int_0^{k_{max}} \frac{E(k)}{k} dk, \tag{4.1}$$

where k is the magnitude of the wave number. To determine a quasi-steady state, the enstrophy $W =< |\omega|^2 >$ and the velocity derivative skewness S_k are often used in the decaying isotropic turbulence[80, 81] where ω is vorticity. The velocity derivative

Case	M_{t0}	$R_{\lambda 0}$	$M_{t\ \mathrm{steady}}$	$R_{\lambda\ \mathrm{steady}}$	Resolution N^3	$k_{\max}\eta$
A02	0.2	130	0.11	32	512^3	6.29
A03	0.3	130	0.17	32	512^3	6.31
A04	0.4	130	0.22	32	512^3	6.35
A05	0.5	130	0.29	33	512^3	6.40
A06	0.6	130	0.33	33	512^3	6.49
A07	0.7	130	0.38	33	512^3	6.59
A08	0.8	130	0.42	33	512^3	6.75
A09	0.9	130	0.45	33	512^3	6.91
A10	1.0	130	0.48	32	512^3	7.22
A10'	1.0	130	0.48	22	384^3	5.34
A10"	1.0	130	0.46	24	256^3	3.69
B02	0.2	100	0.12	29	384^3	5.59
B10	1.0	100	0.48	28	384^3	6.44
C02	0.2	70	0.12	24	256^3	4.96
C10	1.0	70	0.48	24	256^3	5.64

Table 4.1: Parameters used in the direct numerical simulation. M_{t0} and $R_{\lambda 0}$ are the initial values of turbulent Mach number and Taylor micro scale Reynolds number. $M_{t\ \mathrm{steady}}$ and $R_{\lambda\ \mathrm{steady}}$ and $k_{\max}\eta$ are the turbulent Mach number, the Taylor micro scale Reynolds number, and the resolution parameter at the quasi steady state: $t/\tau_0 = 3$ for case A; $t/\tau_0 = 2.78$ for case B; $t/\tau_0 = 2.39$ for case C where τ_0 is the initial value of the large eddy turn over time.

skewness is defined as follows:

$$S_k = \frac{< ((\partial u_i/\partial x_i)^2/3 >}{[< ((\partial u_i/\partial x_i)^2/3 >]^{3/2}}. \tag{4.2}$$

The time history of the enstrophy and the velocity derivative skewness for $R_{\lambda 0} = 130$ are shown in Figs. 4.1 (a) and 4.1 (b), respectively. The value of the enstrophy is normalized by its initial value. The enstrophy has passed the peak after $t/\tau_0 = 2$ and the velocity derivative skewness reaches the steady negative value of around -0.5 at $t/\tau_0 = 3$ for all cases. Those indicate that turbulence developed enough and show nonlinear dynamics with the smallest scales. Therefore, we determine the time t/τ_0=3 as a steady state and compare the results at that time. At $t/\tau_0 = 3$, the kinetic energy $E =< u_i^2 >$ decreases around 33% of the initial state for all cases, and almost decay similarly between cases except for the initial transient (Fig. 4.2). Note that the lower Reynolds number cases develops faster than the cases of $R_{\lambda 0} = 130$, so that we chose the time $t/\tau_0 = 2.39$ for $R_{\lambda 0} = 70$ and $t/\tau_0 = 2.78$ for $R_{\lambda 0} = 100$ when the kinetic energy reaches 33% of the initial values. At the selected times, the enstrophy and the velocity derivative skewness also showed the same sign of the nonlinear characteristics discussed above. We use those selected time for the discussion hereafter.

Before the main discussion, the verification study is conducted. In the computation of the isotropic turbulence, the validation is very difficult to conduct due to lack of the experimental data, so that grid sensitivity is checked, instead. In order to asses the grid sensitivity, we consider the velocity power spectra of two components based on the Helmholtz decomposition:

$$\mathbf{u} = \mathbf{u}^i + \mathbf{u}^c, \tag{4.3}$$

where the incompressible component $\mathbf{u}^i$ and the compressive component $\mathbf{u}^c$ satisfy $\nabla \cdot \mathbf{u}^i = 0$ and $\nabla \times \mathbf{u}^c = \mathbf{0}$, respectively. The case $M_{t0} = 1.0$ at $R_{\lambda 0} = 130$ is shown in Fig. 4.3 with different resolutions where the selected case shows the most probability of shocklets occurrence, so that the necessity of resolution is the highest. The spectra of the incompressible component shows very good agreement between cases. Also, resolution $N^3 = 512$ achieves good grid convergence for the compressive component of the velocity spectra which are highly related with shocklets. In addition to the discussion above, the resolution parameter $k_{max}\eta$ based on the maximum value of wave number k_{max} and the Kolmogorov length scale $\eta = [(< \mu/\rho >)^3/ < \varepsilon/\rho >]^{1/4}$ is shown in Tab. 4.1. Note that $\varepsilon = \tau_{ij}S_{ij}$ is the dissipation where $S_{ij} = 1/2\ (\partial u_i/\partial x_j + \partial u_j/\partial x_i)$ is the strain rate

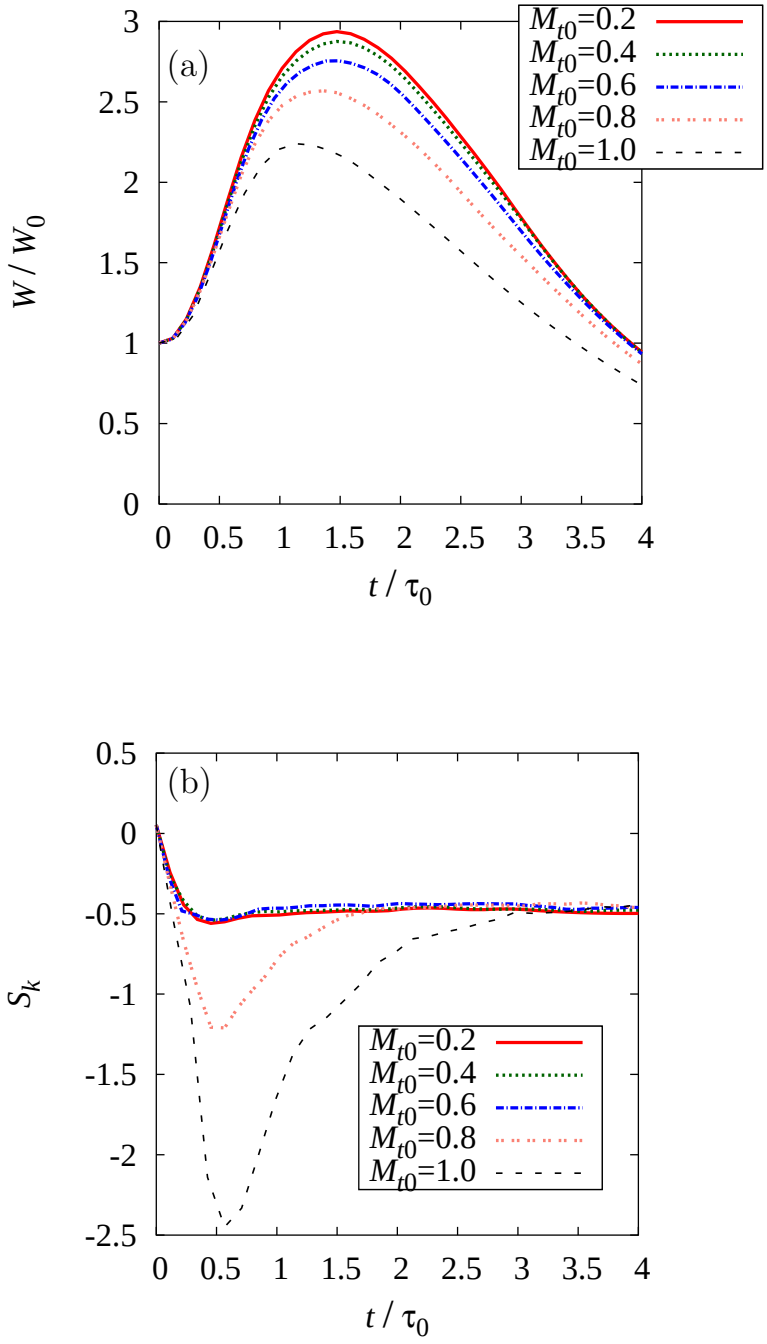

Figure 4.1: Time history of (a) enstrophy and (b) velocity derivative skewness for $R_{\lambda 0} = 130$: —, $M_{t0} = 0.2$; ···, $M_{t0} = 0.4$; – · –, $M_{t0} = 0.6$; ·· ··, $M_{t0} = 0.8$; – –, $M_{t0} = 1.0$. Note that the value of enstrophy is normalized by its initial value.

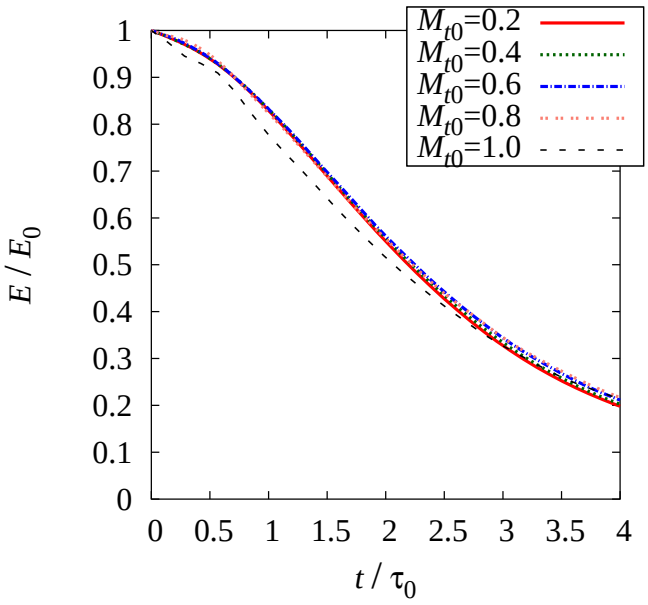

Figure 4.2: Time history of the kinetic energy for $R_{\lambda 0} = 130$: —, $M_{t0} = 0.2$; ···, $M_{t0} = 0.4$; – · –, $M_{t0} = 0.6$; ·· ··, $M_{t0} = 0.8$; – –, $M_{t0} = 1.0$. Note that the value is normalized by its initial value

tensor. All cases except for the verification case A10" are $k_{max}\eta \simeq 5$ or larger which are much larger values of the criteria for DNS of incompressible turbulence $k_{max} \sim 1$, so that the smallest scale turbulent characteristics are well resolved in our simulation. Note that we set the higher resolution from the viewpoint of the criteria of incompressible DNS to capture the characteristics of shocklets which take important role of sound sources in the higher turbulent Mach numbers. Overall, the smallest scale of turbulence and shocklets are well captured in the present simulation. The same confirmation has been done also for $R_{\lambda 0} = 100$ and $R_{\lambda 0} = 70$, and the resolution $N^3 = 384^3$ and $N^3 = 256^3$ are selected for those cases.

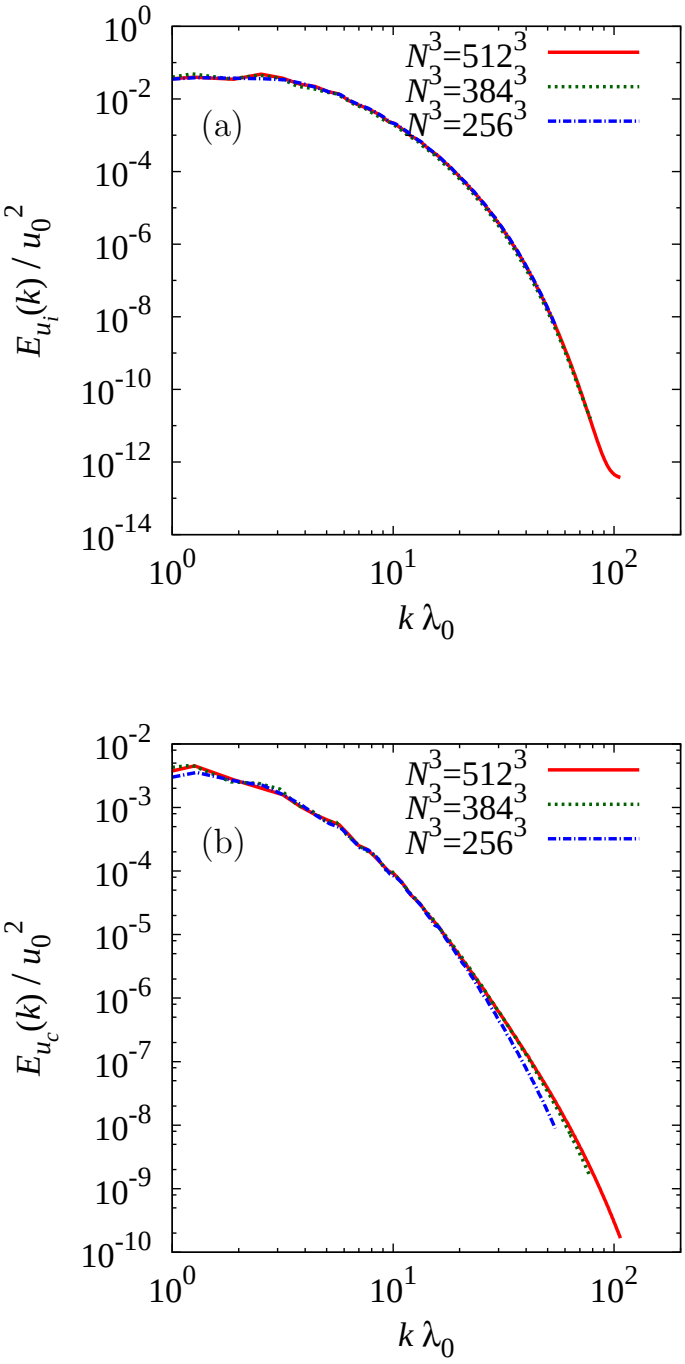

Figure 4.3: Velocity spectra of two components; (a) incompressible component and (b) compressive component for $M_{t0} = 1.0$, $R_{\lambda 0} = 130$ at $t/\tau_0 = 3$: —, $N^3 = 512^3$; $\cdots$, $N^3 = 384^3$; $-\cdot-$, $N^3 = 256^3$.

4.2 Mach number dependence on sound sources

In this subsection, the overall trend of the turbulent Mach number dependence on the source terms of the Lighthill equation are analyzed with the case $R_{\lambda 0} = 130$. The Lighthill equation [12] is defined as follows:

$$\frac{\partial^2 \rho}{\partial t^2} - c_0^2 \nabla^2 \rho = \frac{\partial^2 T_{ij}}{\partial x_i \partial x_j}, \tag{4.4}$$

where T_{ij} is the Lighthill's turbulent stress tensor written as;

$$T_{ij} = \rho u_i u_j + \delta_{ij}[p - p_0 - c_0^2(\rho - \rho_0)] + \mu\Big(\frac{\partial u_i}{\partial x_j}\frac{\partial u_j}{\partial x_i} - \frac{2}{3}\delta_{ij}\frac{\partial u_k}{\partial x_k}\Big). \tag{4.5}$$

Note that p_0, ρ_0, c_0 are the initial values of the pressure, density and the speed of sound, respectively. The second term (entropy component) is exactly zero, if the flow is isentropic, so that it is often neglected in the low Mach number flows. The third term is the viscous stress tensor τ_{ij}. For the higher Reynolds numbers, this term is also considered to be negligible. Thus, the first term of the Reynolds stress contribution is often considered to be the main sound source in the low Mach number turbulent flows. We analyze all components above, however, because the characteristics of three terms in the higher Mach number flows have not been well understood. Also, a previous study showed that the entropy term has non-negligible value even in the low convective Mach number mixing layer due to the dissipation generated around vortices[60], so that all components should be carefully discussed in all range of Mach numbers. In this study, we mostly investigate the sound source characteristics by using the sound source itself $\partial^2 T_{ij}/\partial x_i \partial x_j$, not by the Lightlhill's turbulent stress tensor T_{ij}. Thus, for discussion, we classify the sound source into following three terms:

$$\begin{aligned}
S_{\mathrm{Re}} &= \frac{\partial \rho u_i u_j}{\partial x_i \partial x_j}, \\
S_{\mathrm{en}} &= \frac{\partial(\delta_{ij}[p - p_0 - c_0^2(\rho - \rho_0)])}{\partial x_i \partial x_j}, \\
S_{\mathrm{vis}} &= \frac{\partial\Big(\mu\Big(\frac{\partial u_i}{\partial x_j}\frac{\partial u_j}{\partial x_i} - \frac{2}{3}\delta_{ij}\frac{\partial u_k}{\partial x_k}\Big)\Big)}{\partial x_i \partial x_j}, \\
S_{\mathrm{all}} &= S_{\mathrm{Re}} + S_{\mathrm{en}} + S_{\mathrm{vis}},
\end{aligned} \tag{4.6}$$

where S_{Re} is the Reynolds stress term, S_{en} is the entropy term, S_{vis} is the viscous term, and S_{all} is the sum of three terms (called as term total), respectively. To begin with, the contributions of each source term are analyzed. For the discussion, the sound source

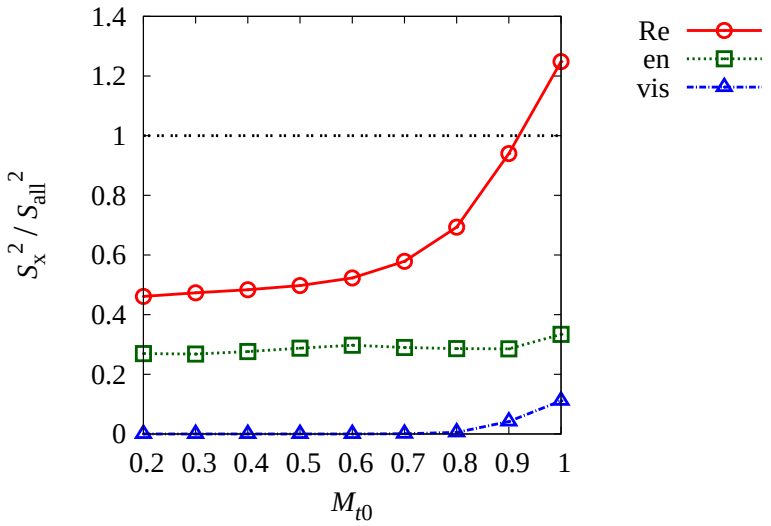

Figure 4.4: The ratio of each term to the overall sound source in the sound source strength for $R_{\lambda 0} = 130$: —, Reynolds stress term $S_{\mathrm{R}e}$; $\cdots$, Entropy term S_{en}; $-\cdot-$, Viscous term S_{vis}. Note that the values are spatially averaged.

strength is defined by the square of source term. The ratio of each source term to the term total in the sound source strength is shown in Fig. 4.4. Note that the values are spatially averaged. The Reynolds stress term shows the most contribution over the range of turbulent Mach numbers as expected. However, the entropy term is not negligible even for the lower turbulent Mach number cases which is differently from the theoretical prediction where the entropy term is negligible in the low Mach number flows. Also, the viscous term can not be negligible for the higher turbulent Mach number cases ($M_{t0} \geq 0.8$). The other important point is that the ratio of the Reynolds stress term exceeds the value of unity for $M_{t0} = 1.0$, so that two or all terms are canceled out each other. For the lower turbulent Mach number cases, on the other hand, source terms are intensified each other, because each value is below unity. Detail discussion for the relationship between terms is conducted after discussing the spectra characteristics.

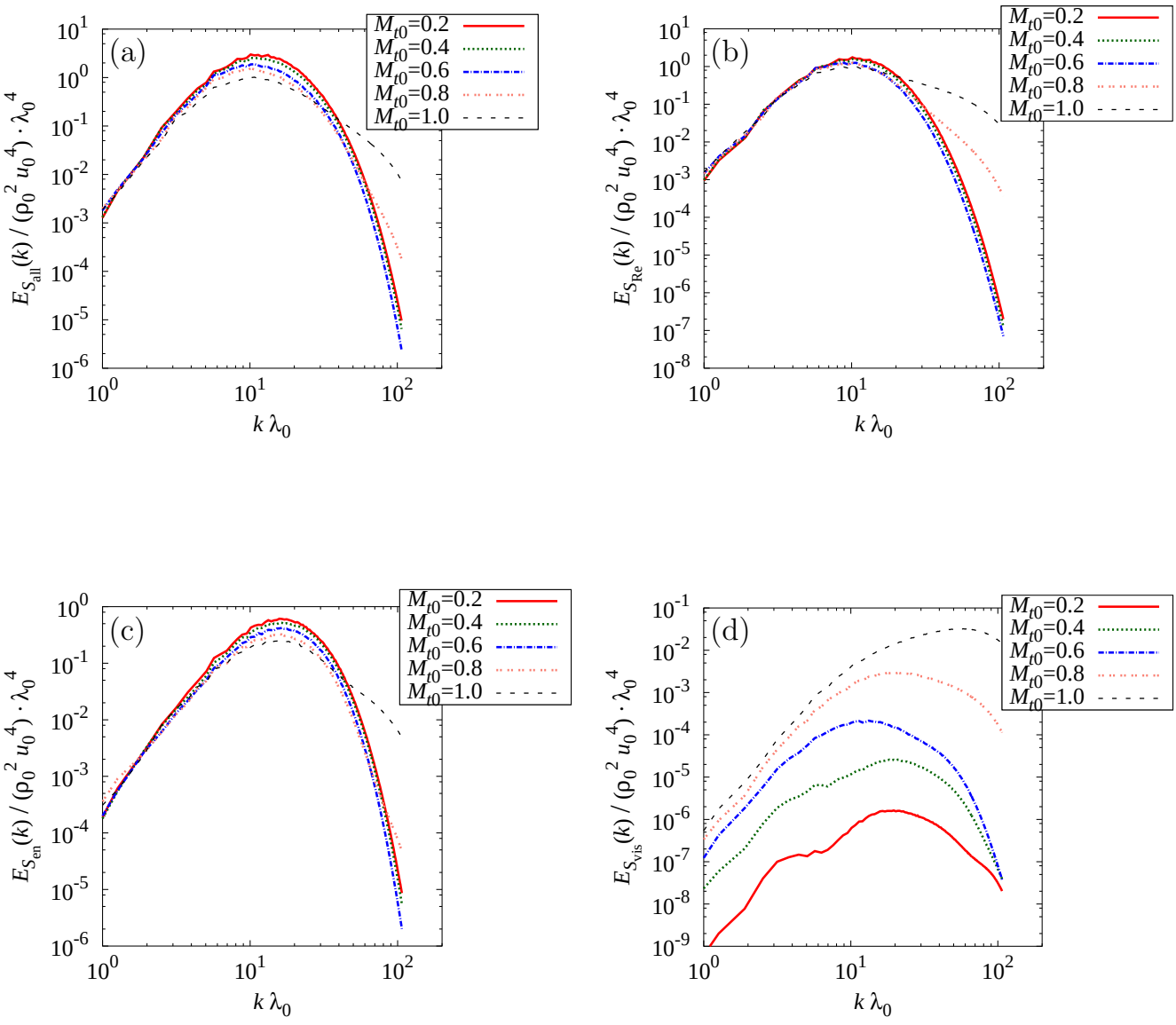

Figure 4.5: Sound source spectra of (a) term total S_{all}, (b) Reynolds stress term S_{Re}, (c) entropy term S_{en} and (d) viscous term S_{vis} for $R_{\lambda 0} = 130$: —, $M_{t0} = 0.2$; ···, $M_{t0} = 0.4$; –·–, $M_{t0} = 0.6$; ·· ··, $M_{t0} = 0.8$; – –, $M_{t0} = 1.0$.

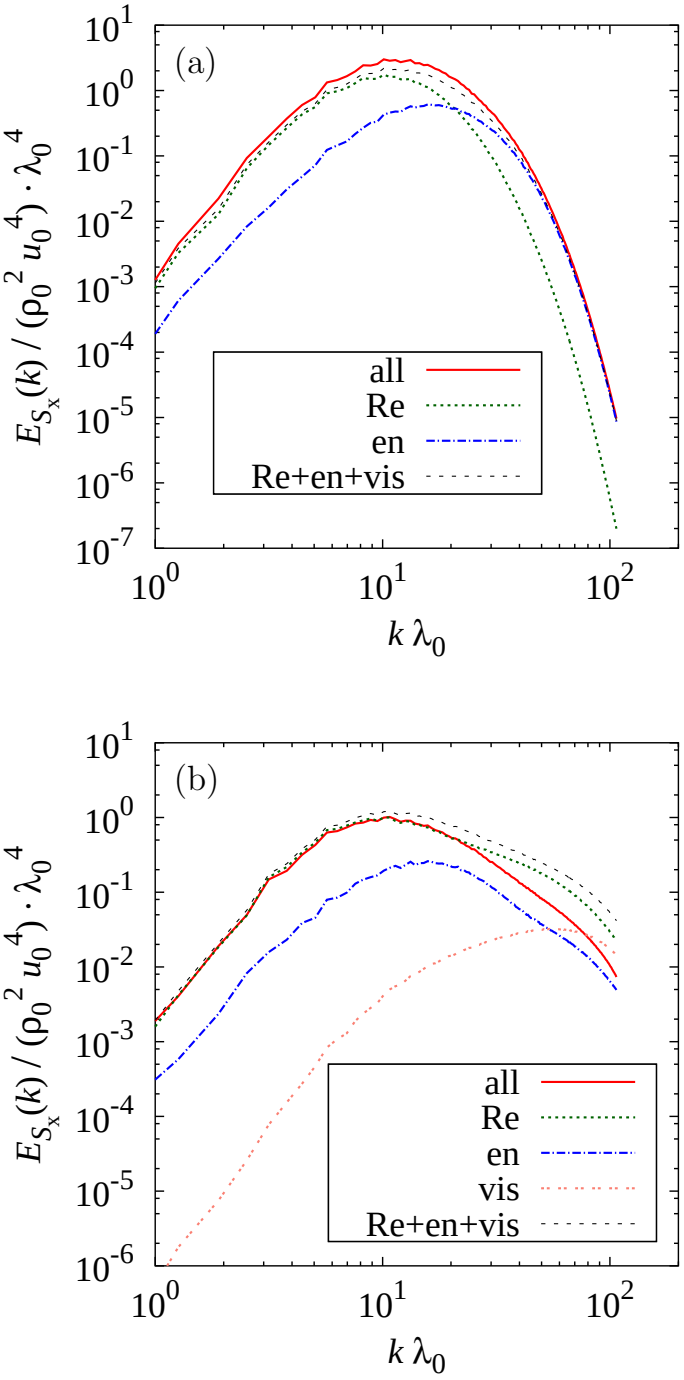

Figure 4.6: Sound source spectra for (a) $M_{t0} = 0.2$ and (b) $M_{t0} = 1.0$ at $R_{\lambda 0} = 130$: —, term total S_{all}; $\cdots$, Reynolds stress term S_{Re}; $-\cdot-$, entropy term S_{en}; $\cdot\cdot\,\cdot\cdot$, viscous term S_{vis}; $-\,-$, simple sum of spectra $S_{\text{Re}} + S_{\text{en}} + S_{\text{vis}}$. Note that the viscous term is not shown for $M_{t0} = 0.2$ due to its negligible value.

For the spectra, the normalization is conducted by the initial values of density ρ_0, the magnitude of velocity u_0 and the Taylor micro scale λ_0, where those values are spatially averaged. Fig. 4.5 shows sound source spectra for five different turbulent Mach number cases. The spectra of the term total have two characteristics. One is the decrease of the peak value with increasing the turbulent Mach number and the other is the appearance of the higher wave number components for the higher turbulent Mach number cases $M_{t0} = 0.8 - 1.0$. Similar trend is observed in the Reynolds stress term and the entropy term, though the degree of change is somewhat different: The peak value decreases more in the entropy term, and the higher wave number components increase more in the Reynolds stress term. The decrease of the peak values would be affected by the compressibility effects in which the vortical motion is suppressed[49, 82]. Note that the ratio of the entropy term to the overall sound source is expected to increase with increasing the turbulent Mach number, because isentropic flow assumption is not suitable any more in the moderate to high turbulent Mach numbers. The expectation in which the ratio of the entropy term increases with increasing the turbulent Mach number is confirmed in Fig. 4.4, though, the strength itself decreases due to the compressibility effects. The results of the viscous term also show the trend in which the values of the higher wave number components increases as the turbulent Mach number increases. The appearance of the higher wave number components for all source terms implies that the different sound generation mechanism between lower and higher turbulent Mach numbers.

M_{t0}	0.2	0.3	0.4	0.5	0.6	0.7	0.8	0.9	1.0
$Corr(S_{\mathrm{Re}}, S_{\mathrm{en}})$	0.38	0.36	0.32	0.28	0.22	0.15	0.01	-0.23	-0.44
$Corr(S_{\mathrm{Re}}, S_{\mathrm{vis}})$	-	-	-	-	-	-	-0.01	-0.08	-0.16
$Corr(S_{\mathrm{en}}, S_{\mathrm{vis}})$	-	-	-	-	-	-	0.13	0.03	0.02

Table 4.2: Correlation coefficients between source terms for $R_{\lambda 0} = 130$.

The spectra of the terms are compared in Fig. 4.6. The viscous term is shown only in the figures of the higher turbulent Mach number case, because the values in the smaller turbulent Mach number cases are too small to discuss. In order to check whether terms are intensified or weakened each other, the spectra of the Reynolds stress term, the entropy term and the viscous term are simply sum up and shown by the line – –. The line does not contain the effects of canceling out or constructive interference between terms, because it is the sum of the square values. If the term total has larger value than the simple sum up spectra, each term is intensified each other, and vice versa. In Fig. 4.6 (a), the term total spectra show the highest value, so that the Reynolds stress term and the entropy term are intensified each other for $M_{t0} = 0.2$. Those terms are intensified at the broad range of the wave numbers. In addition, it is worth noting that the spectrum of the entropy term has the peak at the higher wave number than that of the Reynolds stress term. This is because the entropy term is generated by the diffusion process as discussed in Sec. 4.3. On the other hand, the spectra of simple sum of terms show the highest value for $M_{t0} = 1.0$, so that two terms or all terms are canceled out each other. The trend is remarkable at the higher wave numbers. Thus, the results suggest that a smaller scale event should be the key for the terms to be canceled out each other. The reason will be discussed in Sec. 4.4. For more precise discussion, terms are compared one by one using the joint probability density function (JPDF). In Fig. 4.7, we show JPDF of the Reynolds stress term S_{Re} and the entropy term S_{en}. Terms are normalized by the rms values. Positive correlation is observed for $M_{t0} = 0.2$. The correlation decreases with increasing the turbulent Mach number, and case $M_{t0} = 0.8$ shows almost no correlation. For the highest turbulent Mach number case $M_{t0} = 1.0$, then, shows negative correlation. Correlation coefficients in Tab. 4.2 also show the trend where the lower turbulent Mach numbers show poisitive correlation, whereas the higher turbulent Mach numbers show negative correlation. The reason why the trend is changed depending on the turbulent Mach number is that eddy shocklets become important sound sources for the higher turbulent Mach numbers in addition to vortices. The remaining relationships regarding the viscous term are also considered. JPDF of the viscous term

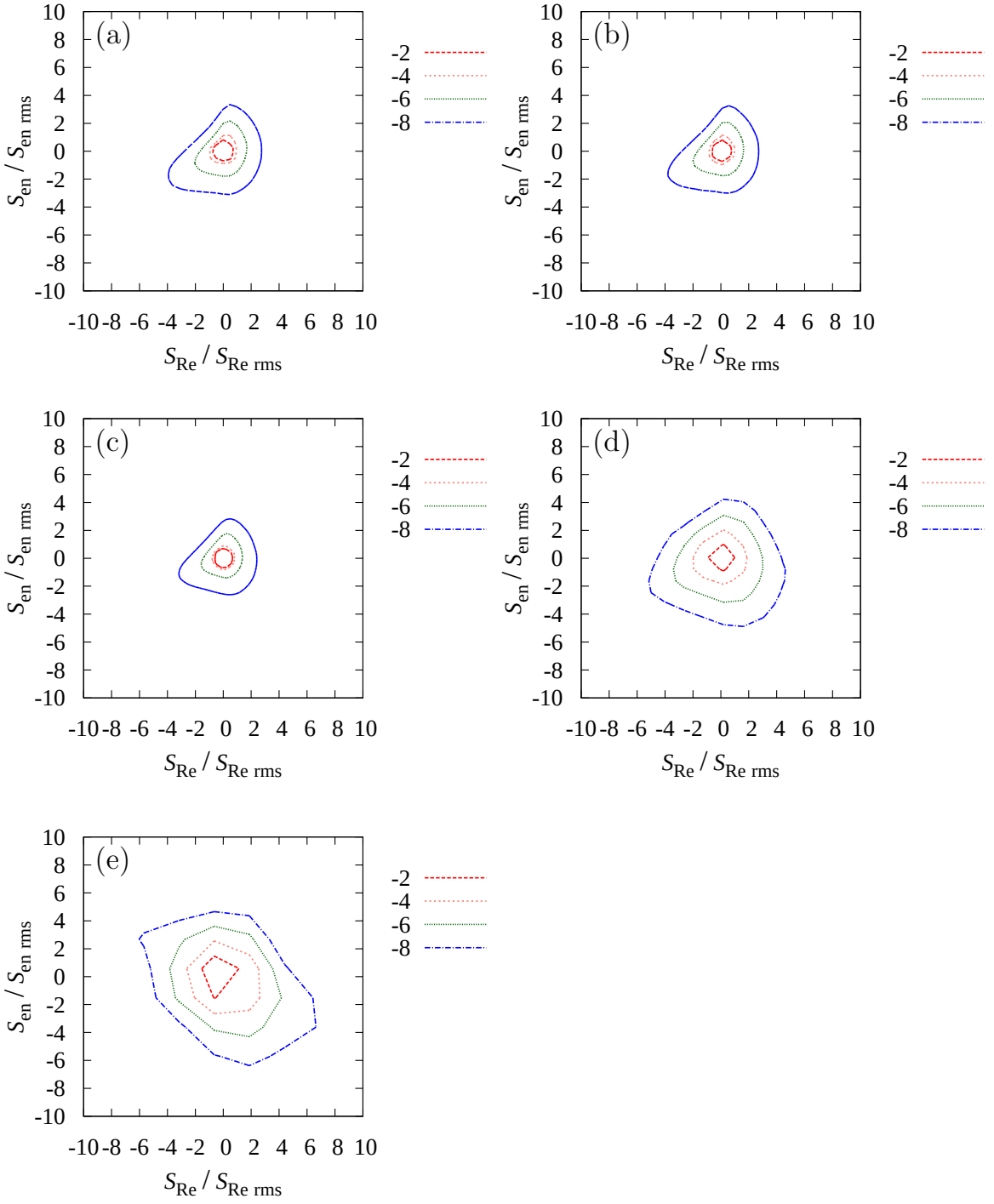

Figure 4.7: $\log_{10}\mathrm{PDF}(S_{\mathrm{Re}}/S_{\mathrm{Re\ rms}}, S_{\mathrm{en}}/S_{\mathrm{en\ rms}})$ for (a) $M_{t0} = 0.2$, (b) $M_{t0} = 0.4$, (c) $M_{t0} = 0.6$, (d) $M_{t0} = 0.8$ and (e) $M_{t0} = 1.0$ at $R_{\lambda 0} = 130$: Contour lines are —, 10^{-2}; – · –, 10^{-4}; ·· ··, 10^{-6}; – –, 10^{-8}.

and the Reynolds stress term is shown in Fig. 4.8, and that of the viscous term and the entropy term is shown in Fig. 4.9. Note that the only higher turbulent Mach number cases are shown in Figs. 4.8 and 4.9, because the viscous term is negligible in the lower turbulent Mach number cases. Figures do not show clear correlation differently from Fig. 4.7 (a) or Fig. 4.7 (e). Correlation coefficients (Tab. 4.2) also confirm that there is no clear correlation between the viscous term and the remaining terms. To summarize, the results show the different sound source characteristics between the lower turbulent Mach number and higher turbulent Mach number flows. In the next section, the sound source characteristics in the lower turbulent Mach numbers are discussed in detail. After the discussion, detail investigation of the higher turbulent Mach numbers is conducted.

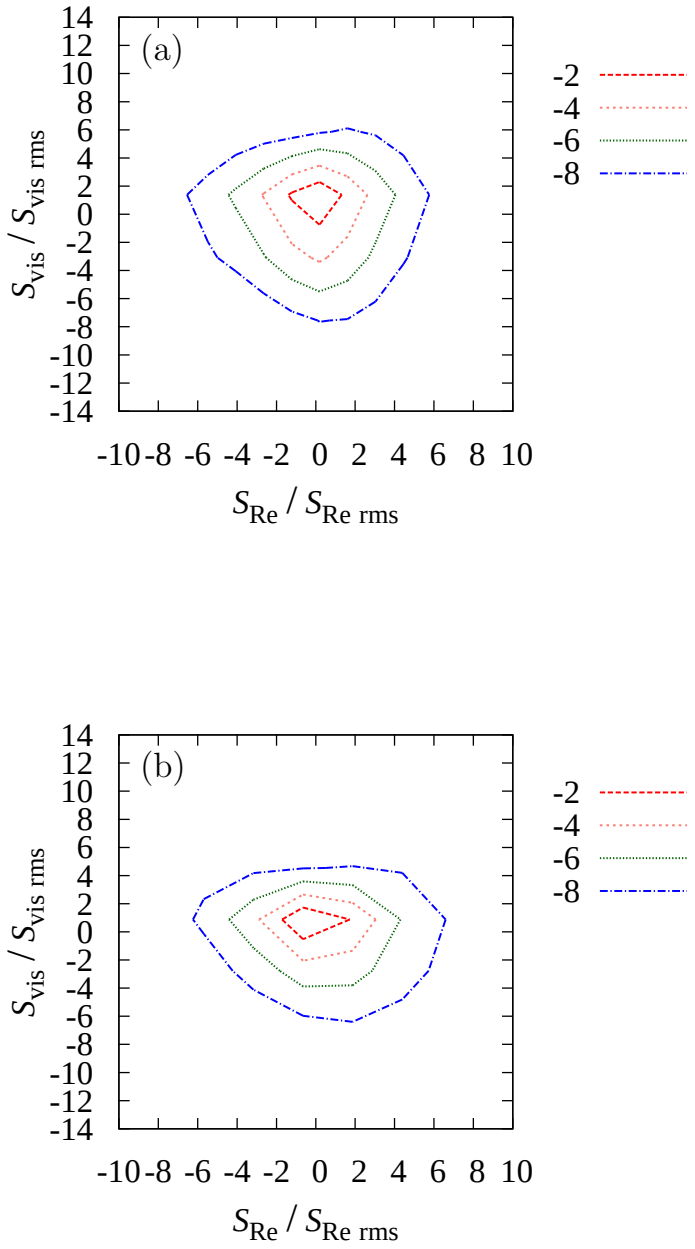

Figure 4.8: $\log_{10}\mathrm{PDF}(S_{\mathrm{Re}}/S_{\mathrm{Re\ rms}}, S_{\mathrm{vis}}/S_{\mathrm{vis\ rms}})$ for (a) $M_{t0} = 0.8$, (b) $M_{t0} = 1.0$ for $R_{\lambda 0} = 130$: Contour lines are —, 10^{-2}; – · –, 10^{-4}; ·· ··, 10^{-6}; – –, 10^{-8}.

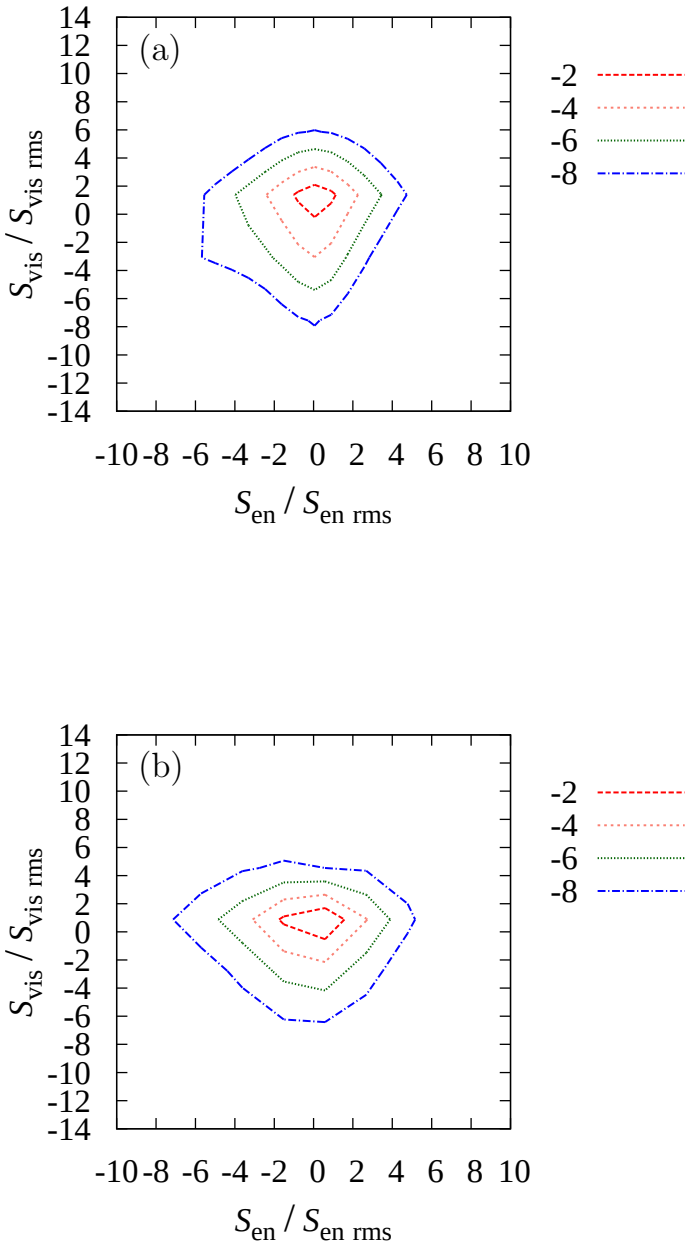

Figure 4.9: $\log_{10}\mathrm{PDF}(S_{\mathrm{en}}/S_{\mathrm{en\ rms}}, S_{\mathrm{vis}}/S_{\mathrm{vis\ rms}})$ for (a) $M_{t0} = 0.8$, (b) $M_{t0} = 1.0$ for $R_{\lambda 0} = 130$: Contour lines are —, 10^{-2}; – · –, 10^{-4}; ·· ··, 10^{-6}; – –, 10^{-8}.

4.3 Sound sources in low turbulent Mach numbers

In this subsection, we use $M_{t0} = 0.2$ as the representative of low turbulent Mach number cases. Fig. 4.4 showed that the Reynolds stress term and the entropy term are two main sound sources in the lower turbulent Mach numbers, so that those terms are analyzed. Firstly, we discuss the Reynolds stress term by focusing on the similarity with the second invariant of the velocity gradient tensor. The second invariant of the velocity gradient tensor is defined as;

$$Q = \xi_1\xi_2 + \xi_2\xi_3 + \xi_3\xi_1 = \frac{1}{2}(P^2 - S_{ij}S_{ij} + \Omega_{ij}\Omega_{ij}), \tag{4.7}$$

where $P = -(\xi_1 + \xi_2 + \xi_3) = -\partial u_i/\partial x_i = -\theta$, $S_{ij} = 1/2\ (\partial u_i/\partial x_j + \partial u_j/\partial x_i)$ and $\Omega_{ij} = 1/2\ (\partial u_i/\partial x_j - \partial u_i/\partial x_j)$ are the first invariant of the velocity gradient tensor (negative dilatation), the strain rate tensor and the rotation rate tensor, respectively, and ξ_i are the three eigenvalues of the velocity gradient tensor. In the nearly incompressible regime, P is negligibly small due to almost divergence free flow field; thus, (Eq. 4.7) can be written as follows:

$$Q = Q_{\text{inc}} = \frac{1}{2}(-S_{ij}S_{ij} + \Omega_{ij}\Omega_{ij}) = -\frac{1}{2}\frac{\partial u_i}{\partial x_j}\frac{\partial u_j}{\partial x_i}. \tag{4.8}$$

Thus, the Reynolds stress term in nearly incompressible regime is considered as well. Assuming constant density, the Reynolds stress term is written as;

$$\begin{aligned}
S_{\text{Re inc}} &= \rho_0 \frac{\partial^2 (u_i u_j)}{\partial x_i \partial x_j} \\
&= \rho_0 \frac{\partial}{\partial x_j}\left(\frac{\partial u_i u_j}{\partial x_i}\right) \\
&= \rho_0 \frac{\partial}{\partial x_j}\left(u_i \frac{\partial u_j}{\partial x_i} + u_j \frac{\partial u_i}{\partial x_i}\right) \\
&= \rho_0 \frac{\partial}{\partial x_j}\left(u_i \frac{\partial u_j}{\partial x_i}\right) \\
&= \rho_0 \frac{\partial u_i}{\partial x_j}\frac{\partial u_j}{\partial x_i} + u_i \frac{\partial}{\partial x_i}\left(\frac{\partial u_j}{\partial x_j}\right) \\
&= \rho_0 \frac{\partial u_i}{\partial u_j}\frac{\partial u_j}{\partial x_i},
\end{aligned} \tag{4.9}$$

where $\partial x_k/\partial u_k \simeq 0$ is used to have 4th and 6th equality. (Eq. 4.8) and (Eq. 4.9) show that the second invariant and the Reynolds stress term indicate almost the same distribution (but signs are opposite) in low Mach number flows[60]. The Reynolds stress

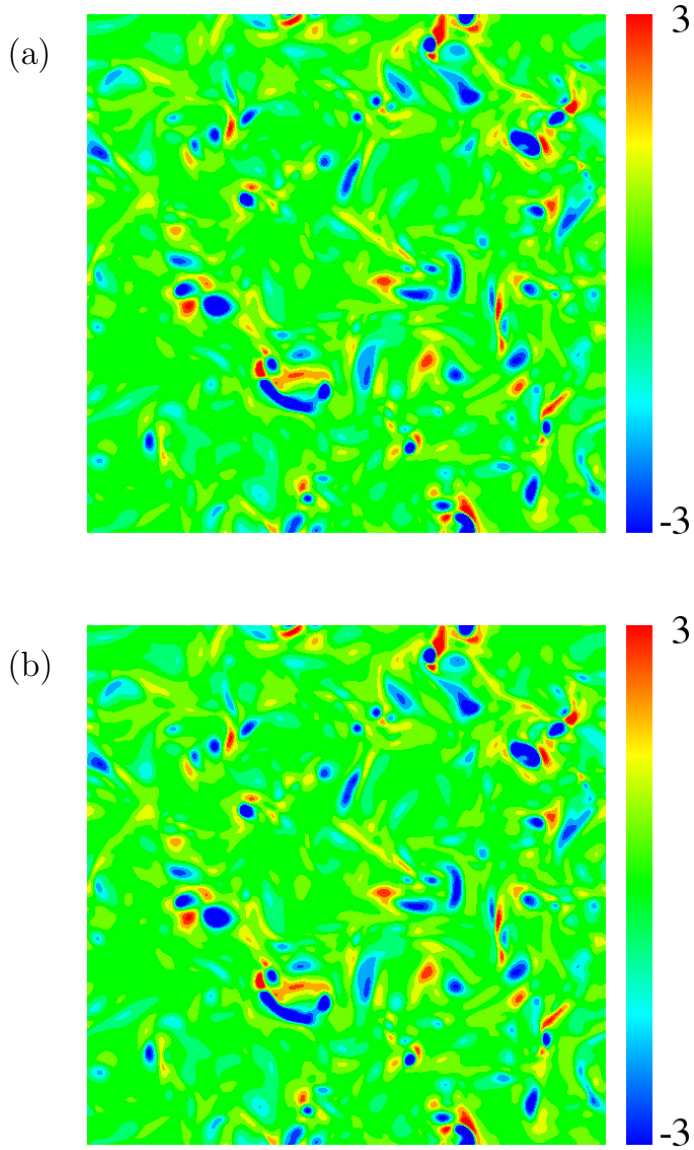

Figure 4.10: Cross section of (a) normalized Reynolds stress term $S_{\mathrm{Re}}/S_{\mathrm{Re\ rms}}$ and (b) normalized negative second invariant $-Q/Q_{\mathrm{rms}}$ at $z/2\pi$=0.5.

term and the negative second invariant of the velocity gradient tensor for $M_{t0} = 0.2$ is shown in Fig. 4.10. Those show almost the same distributions as expected, so that vortices are one of the main sound sources in the lower turbulent Mach number cases.

From the results of Fig. 4.4, the assumption of isentropic flow is not applicable due to the existence of the entropy term. To understand the reason, we consider the following entropy equation:

$$\rho T\Big(\frac{\partial s}{\partial t} + (\nabla \cdot \mathbf{u})s\Big) = \kappa \nabla^2 T + \varepsilon, \tag{4.10}$$

where κ is the thermal conductivity and ε is the dissipation. Entropy equation shows that

$Corr(\lvert S_{\rm en}\rvert, \lvert\kappa\nabla^2 T\rvert)$	$Corr(\lvert S_{\rm en}\rvert, \lvert\varepsilon\rvert)$
0.81	0.44

Table 4.3: Correlation coefficients between the magnitude of the entropy term $S_{\rm en}$ and the right-hand side terms of entropy equation ($\kappa\nabla^2 T$ and ε) for $M_{t0} = 0.2, R_{\lambda 0} = 130$ where ε is the dissipation and $\kappa\nabla^2 T$ is the temperature contribution.

non-uniformity of the entropy is caused by $\kappa\nabla^2 T$ (called as temperature contribution) and the dissipation ε, because the flow is nearly incompressible i.e. $\nabla \cdot \mathbf{u} \simeq 0$. Those terms and the entropy term are shown in Fig. 4.11 with contour lines of the positive values of the second invariant Q which represents vortices. The entropy term and the temperature contribution have similar distributions around vortices. Also, some strong dissipation regions around vortices correspond to the entropy term existence regions. Those two terms are related with the diffusion process, so that those leads the smaller scales in the entropy term. Thus, the spectrum of the entropy term shows the peak at the higher wave number than that of the Reynolds stress term (Fig. 4.6 (a)). In addition, the correlation coefficients of the magnitude of the entropy term and those of right-hand side terms of the entropy equation in Tab. 4.3 indicate that the production of the entropy term is affected more by the temperature contribution $\kappa\nabla^2 T$ than the dissipation ε. Note that both the temperature contribution $\kappa\nabla^2 T$ and the dissipation ε are related with temperature, because the dissipation is related with the thermal energy. Thus, the change in temperature is the key to determine the distributions of the entropy term. In order to study how the change in temperature affects the entropy term, the entropy term (Eq. 4.6) is divided into two terms as follows:

$$\begin{aligned} S_{\rm en} &= \nabla^2 p - c_0^2 \nabla^2 \rho \\ S_{{\rm en}_p} &= \nabla^2 p \\ S_{{\rm en}_\rho} &= c_0^2 \nabla^2 \rho, \end{aligned} \tag{4.11}$$

where $S_{{\rm en}_p}$ is the pressure contribution of the entropy term and $S_{{\rm en}_\rho}$ is the density contribution. The cross section of the entropy term S_{en}, those of the pressure contribution $S_{{\rm en}_p}$ and the negative density contribution $S_{{\rm en}_\rho}$ are shown in Fig. 4.12. Note that the value of the density contribution is set to be negative for visibility. The distributions of the pressure contribution and the negative density contribution are similar, but the magnitude is larger for the density contribution than that for the pressure contribution. Thus, the distributions of the total entropy term become more like those of the negative

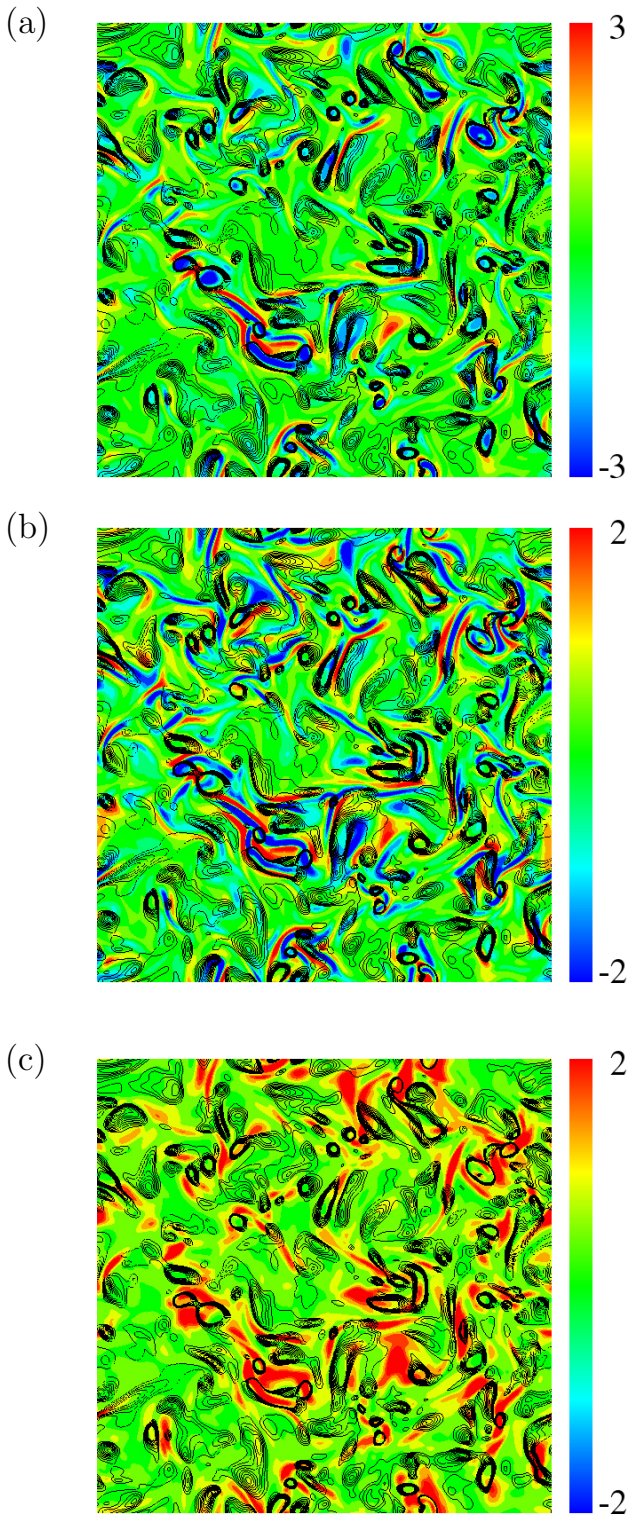

Figure 4.11: Cross section of (a) normalized entropy term $S_{\mathrm{en}}/S_{\mathrm{enrms}}$ and (b) normalized temperature contribution $\kappa\nabla^2 T/(\kappa\nabla^2 T)_{\mathrm{rms}}$ and (c) normalized dissipation $\varepsilon/\varepsilon_{\mathrm{rms}}$ with contour lines of normalized second invariant of the velocity gradient tensor Q/Q_{rms} at $z/2\pi$=0.5. The range of contour lines is $0 \leq Q/Q_{\mathrm{rms}} \leq 2$.

$Corr(S_{\mathrm{en_p}}, Q)$	$Corr(S_{\mathrm{en}_\rho}, Q)$
0.99	0.88

Table 4.4: Correlation coefficients between divided entropy term ($S_{\mathrm{en_p}}$ and S_{en_ρ}) and second invariant of the velocity gradient tensor Q for $M_{t0} = 0.2, R_{\lambda 0} = 130$.

density contribution. One possible explanation for them is that only density is affected by temperature, whereas the pressure is determined by the velocity field in the form of Poisson equation in nearly incompressible flows. In incompressible flows, the pressure contribution $\nabla^2 p$ is exactly the same as the second invariant of the velocity gradient tensor Q, so that the correlation coefficients between $\nabla^2 p$ and Q in Tab. 4.4 supports the discussion. The value of $Corr(S_{\mathrm{en_p}}, Q)$ is almost unity, whereas $Corr(S_{\mathrm{en}_\rho}, Q)$ is below 0.9. Thus, only density is affected by temperature. To summarize, the entropy term is generated by the temperature contribution $\kappa\nabla^2 T$ and the dissipation ε of the entropy equation which are both related with change in temperature. Only the density contribution of the entropy term is affected by the change in temperature. Those lead to the larger magnitude in the density contribution of the entropy term. It is worth noting that the pressure contribution of the entropy term (which have almost the same distributions as Q, and so, as $-S_{\mathrm{Re}}$) and the density contribution show, basically, similar distributions, but the magnitude of the density contribution become larger affected by temperature, so that the total entropy term partly shows similar distributions with S_{Re} $(-Q)$. Thus, the Reynolds stress term and the entropy term are partially intensified each other.

As the final topic of this subsection, the Reynolds number dependence is discussed. The change in the characteristics depending on the Reynolds number are explained by using sound source spectra for three different Reynolds number cases (Fig. 4.13). Note that the viscous term is not shown here due to its negligible value. The larger peak values and higher wave number components appear with increasing the Reynolds number, but the basic shape of spectra does not change for all terms. Those results are acceptable, because the characteristics are corresponding to those of higher Reynolds number flows. Note, however, that the contribution of the entropy term should be carefully discussed. This is because the entropy term is generated by the diffusion process ($\kappa\nabla^2 T$ and ε), so that the effects would be smaller with increasing the Reynolds number due to the smaller values of thermal conductivity κ and viscosity μ in the higher Reynolds number flows, though the trend was not observed in the present range of the Reynolds number.

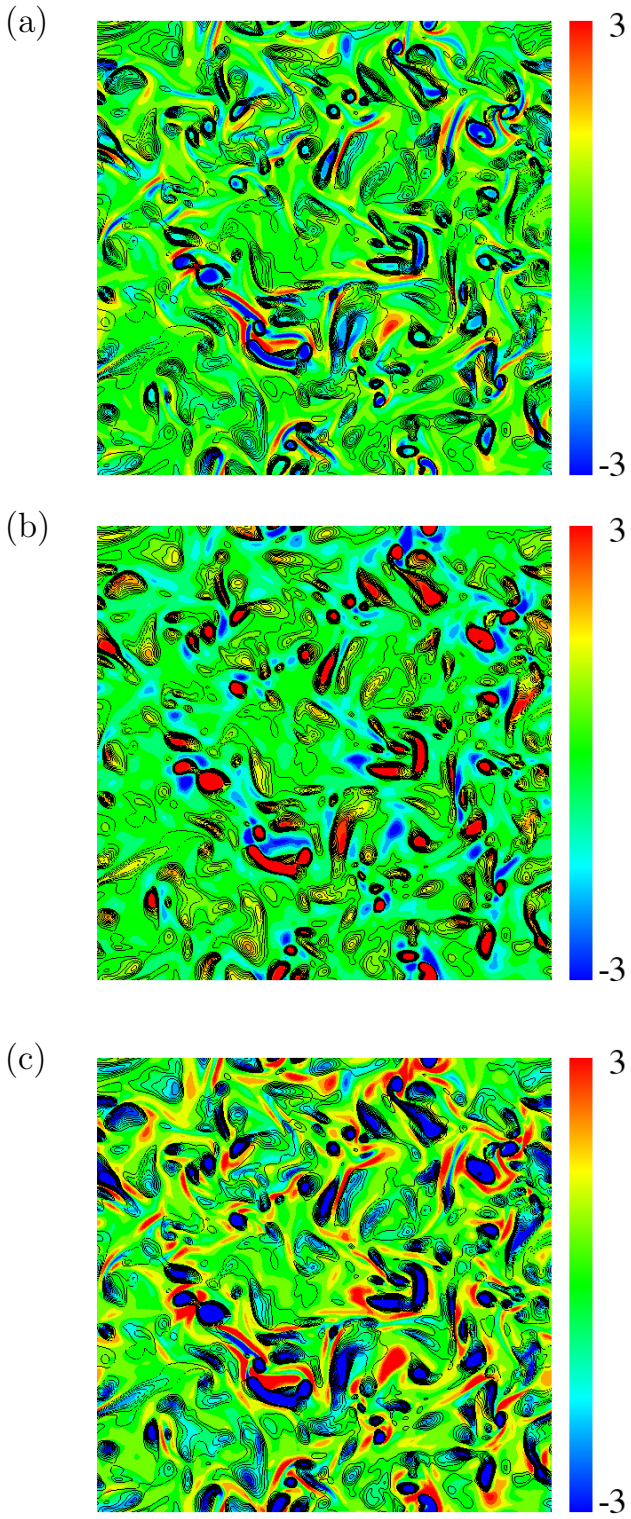

Figure 4.12: Cross section of (a)normalized entropy term$S_{\mathrm{en}}/S_{\mathrm{en\ rms}}$ and (b)normalized pressure contribution of entropy term $\nabla^2 p/(\nabla^2 p)_{\mathrm{rms}}$ and (c) normalized negative density contribution of entropy term $-c_0^2\nabla^2\rho/(c_0^2\nabla^2\rho)_{\mathrm{rms}}$ with contour lines of normalized second invariant of the velocity gradient tensor Q/Q_{rms} at $z/2\pi$=0.5. The range of contour lines is $0 \leq Q/Q_{\mathrm{rms}} \leq 2$.

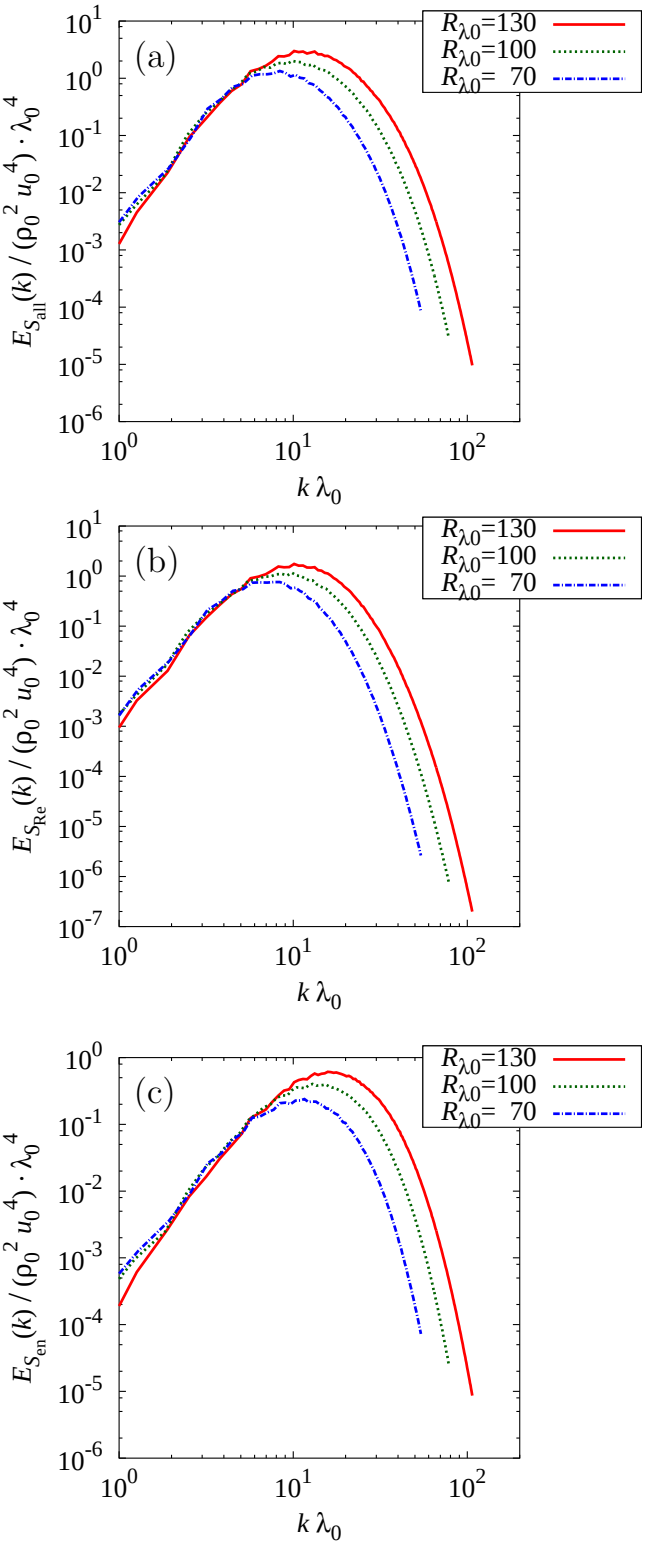

Figure 4.13: Reynolds number dependence on sound source spectra of (a) term total S_{all}, (b) Reynolds stress term S_{Re} and (c) entropy term S_{en} for $M_{t0} = 0.2$: —, $R_{\lambda 0} = 130$; ···, $R_{\lambda 0} = 100$; – · –, $R_{\lambda 0} = 70$.

θ/θ_{rms}	$[-\infty, -2.0]$	$[-2.0, -1.0]$	$[-1.0,\ 0.0]$	$[\ 0.0,\ 1.0]$	$[\ 1.0,\ 2.0]$	$[\ 2.0,\ \infty]$
Fractions of $S^2_{\mathrm{all}}[\%]$	26.4	10.0	24.4	29.0	8.0	2.2
Fractions of $S^2_{\mathrm{Re}}[\%]$	48.7	9.5	17.0	18.0	5.2	1.6
Fractions of $S^2_{\mathrm{en}}[\%]$	30.1	8.4	23.2	29.0	7.5	1.8
Fractions of $S^2_{\mathrm{vis}}[\%]$	75.7	5.0	5.2	5.0	3.9	5.2

Table 4.5: Percentage of sound source strength in flow regions with various dilatation levels for $M_{t0} = 1.0$.

4.4 Sound sources in high turbulent Mach numbers

JPDF of the Reynolds stress term and the entropy term in the higher turbulent Mach numbers show negative correlation, whereas it shows positive correlation in the lower turbulent Mach numbers (Fig. 4.7). An important difference between the lower turbulent Mach numbers and higher turbulent Mach numbers is the level of dilatation. For the higher turbulent Mach numbers, the level of dilatation increases due to the compressibility. Previous studies[83, 52, 84] conducted conditional sampling by the local dilatation level and showed that the statistical properties in strong compression region are changed significantly due to the existence of shocklets. We follow their analysis and apply to the analysis of sound sources. Fig. 4.14 shows JPDF of the Reynolds stress term and the entropy term conditioned on various dilation levels. The results clearly showed that the negative correlation is shown in the strong compression region $\theta/\theta_{\mathrm{rms}} \leq -2$. Also, the compression region is one of the most contributer to the overall sound source strength for all terms (Tab. 4.5). Those results suggest the appearance of the important sound sources in strong compression region. For visualization, we show the iso-surface of dilation at $\theta/\theta_{\mathrm{rms}} = -3$ colored by the Reynolds stress term and the entropy term in Fig. 4.15. Iso-surface of dilatation shows sheet-like structures which are similar to the reported structures of shocklets[52]. Also, both terms show large values on the iso-surface of dilatation. In addition, the distributions of the Reynolds stress term and the entropy term show opposite signs. Therefore, shocklets in strong compression region are strong sound sources and lead canceling out of the Reynolds stress term and the entropy term.

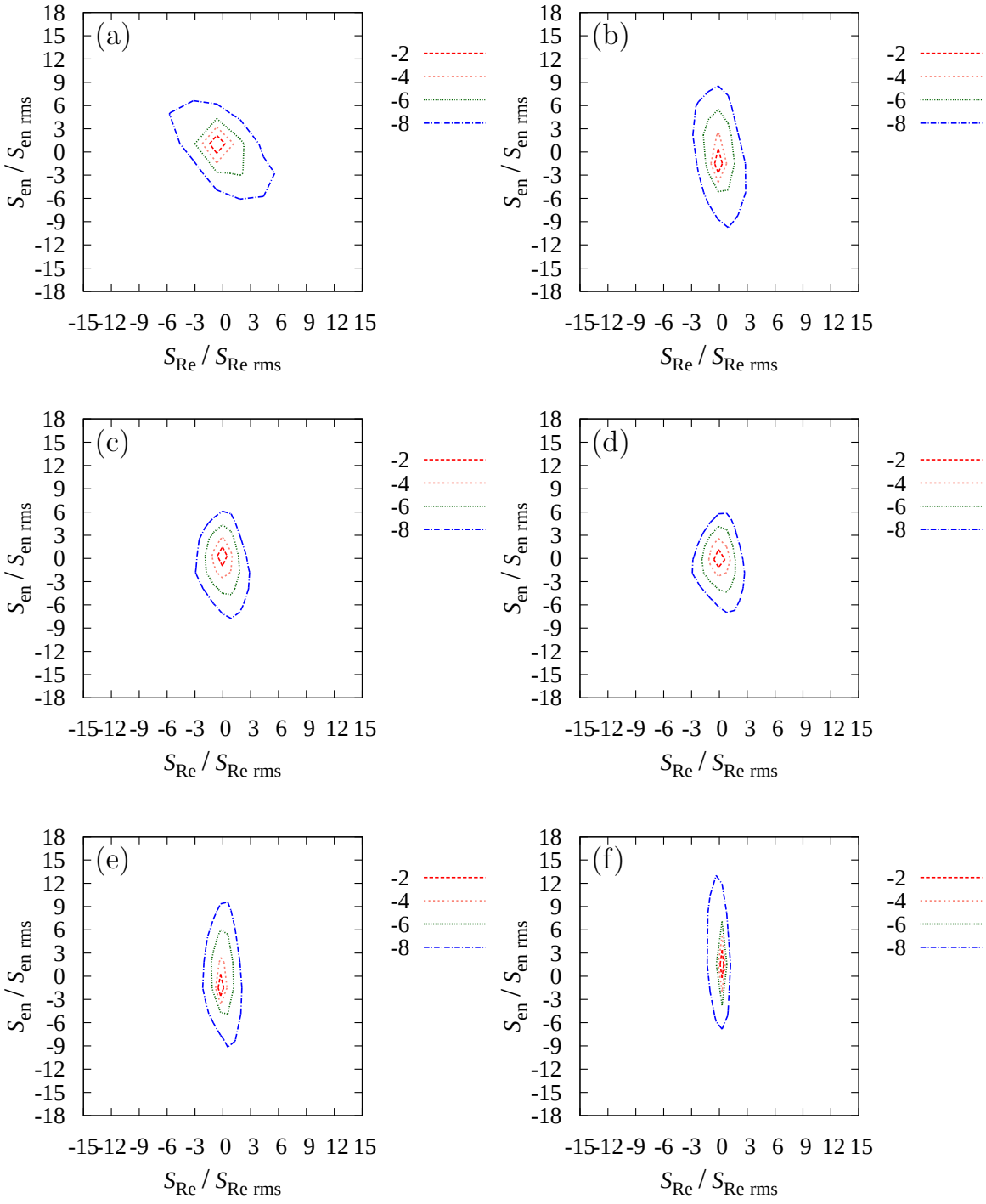

Figure 4.14: $\log_{10}\mathrm{PDF}(S_{\mathrm{Re}}/S_{\mathrm{Re\ rms}}, S_{\mathrm{en}}/S_{\mathrm{en\ rms}})$ for $M_{t0} = 1.0, R_{\lambda 0} = 130$ at (a) $\theta/\theta_{\mathrm{rms}} \leq -2$, (b) $-2 \leq \theta/\theta_{\mathrm{rms}} \leq -1$, (c) $-1 \leq \theta/\theta_{\mathrm{rms}} \leq 0$, (d) $0 \leq \theta/\theta_{\mathrm{rms}} \leq 1$, (e) $1 \leq \theta/\theta_{\mathrm{rms}} \leq 2$ and (f) $\theta/\theta_{\mathrm{rms}} \geq 2$: Contour lines are —, 10^{-2}; – · –, 10^{-4}; ·· ··, 10^{-6}; – –, 10^{-8}.

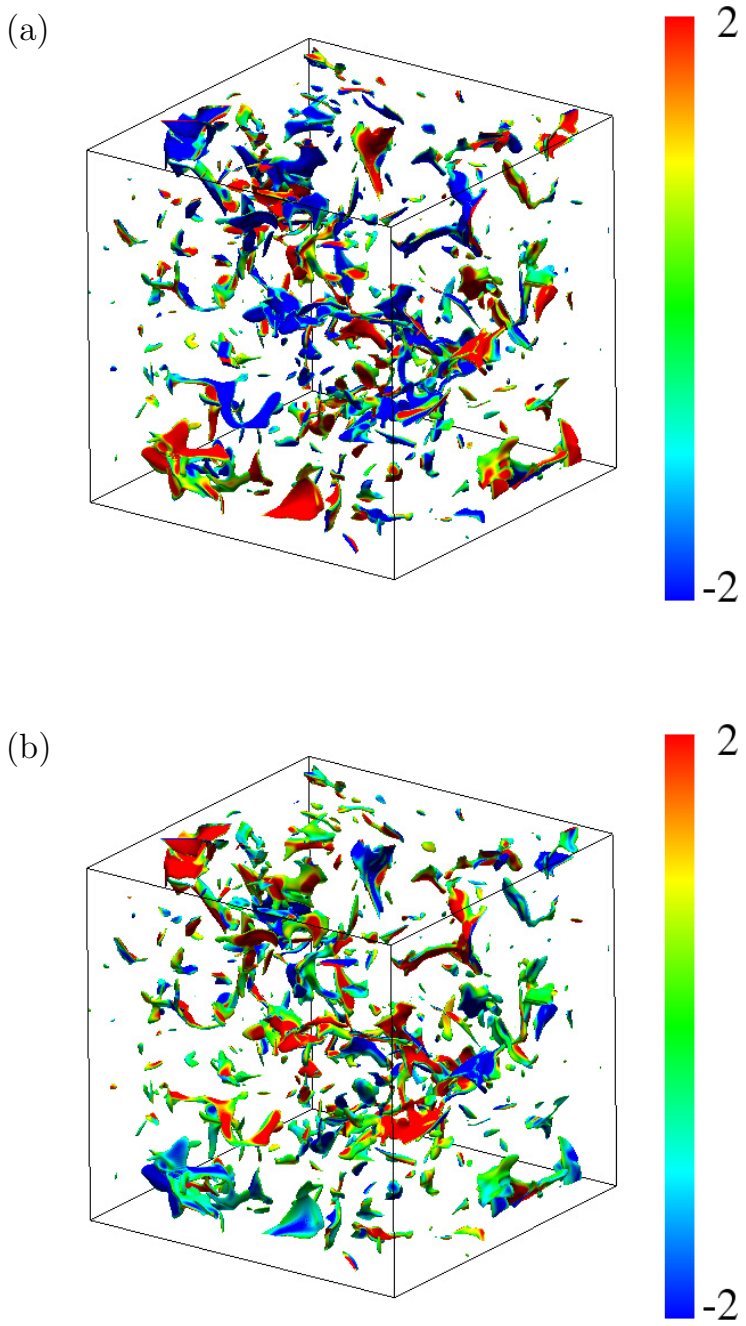

Figure 4.15: Distributions of (a) normalized Reynolds stress term $S_{\mathrm{Re}}/S_{\mathrm{Re}\ rms}$ and (b) normalized entropy term $S_{en}/S_{en\ rms}$ on the iso-surface of normalized dilatation $\theta/\theta_{rms} = -3$.

To discuss in detail, shocklets extraction is conducted. The method used here is similar to the previous studies[5, 51, 70]. The brief procedure to extract shocklets are as follows:

1. The local minimum of dilatation at $\theta/\theta_{\rm rms} \leq -3$ is detected.
2. The shock normal direction is determined by $\nabla p/|\nabla p|$.
3. The physical values (including pressure and density) in lines of shock normal direction is calculated using tri-linear interpolation.
4. If the pressure ratio p_r and the density ratio ρ_r between upstream and downstream $(p_r - 1)(\rho_r - 1) < 0$, the extracted shocklets is not used.
5. If the pressure ratio $p_r < 1$, invert the pressure ratio to $1/p_r$ and the density ratio to $1/\rho_r$.
6. The reference values of pressure ratio p_r and density ratio ρ_r are determined from the computed values on the shock normal lines by minimizing following function based on the ideal Rankine-Hugoniot condition:

$$C = \left| \rho_r - \frac{(\gamma+1)p_r + \gamma - 1}{(\gamma-1)p_r + \gamma + 1} \right|, \tag{4.12}$$

where $C = 0$ means that the values satisfy the Rankine-Hugoniot condition exactly.

Fig. 4.16 shows the distributions of dilatation across shocklets for $M_{t0} = 1.0, R_\lambda = 130$ where d is the distance from the shock and η is the Kolmogorov length scale. The positive d and the negative d show the upstream and the downstream of shocklets. The shape of dilatation shows very good agreement with that of the extracted shocklets in the previous study[51]. The computed reference values of the pressure ratio p_r and density ratio ρ_r are shown in Fig 4.17 as scatter plots. The plots are also very good agreement with the ideal Rankine-Hugoniot condition represented by the solid line.

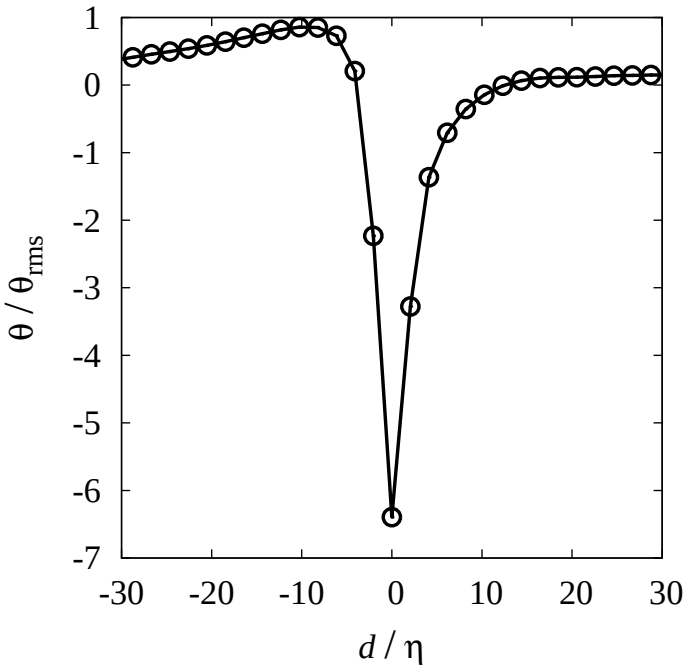

Figure 4.16: Distribution of normalized dilatation $\theta/\theta_{\rm rms}$ across shocklets for $M_{t0} = 1.0, R_{\lambda 0} = 130$. Distance d is normalized by the Kolmogorov length scale η. The positive d and the negative d show the upstream and the downstream of shocklets.

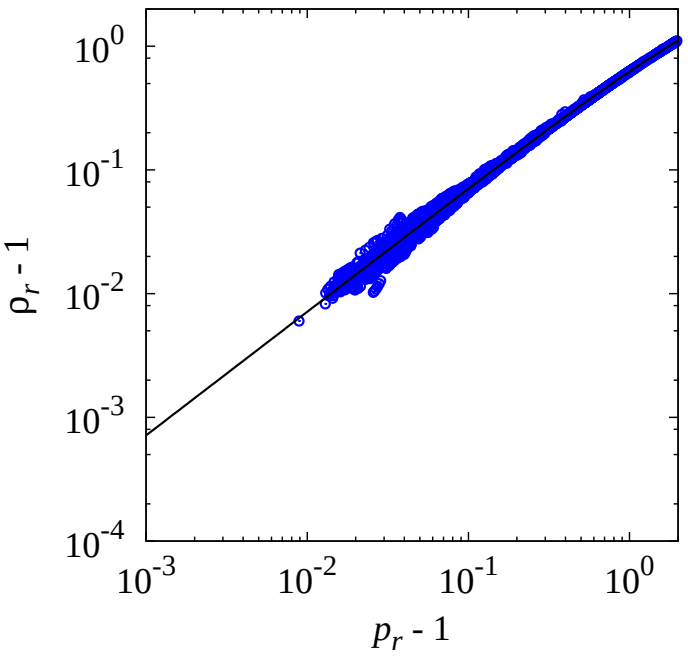

Figure 4.17: Pressure ratio p_r v.s. density ratio ρ_r in the normal direction to the extracted shocklets for $M_{t0} = 1.0, R_{\lambda 0} = 130$. Roughly 22000 points are used for the scattered plots. The solid line represents the ideal Rankine-Hugoniot relation.

Then, we discuss the sound sources around shocklets. Fig. 4.18 shows the sound source distributions across shocklets for $R_{\lambda 0} = 130, M_{t0} = 1.0$. All terms have large values near shocklets. The term total S_{all} and the Reynolds stress term S_{Re} have similar shape (positive peak at the back and negative peak at the front of shocklets), so that the Reynolds stress term is the main sound sources across shocklets. The entropy term also has two peaks across shocklets, but the sign is opposite to that of the Reynolds stress term. The results confirm that the Reynolds stress term and the entropy term are canceled out each other across shocklets. The viscous term, on the other hand, has different trend which has strong negative peak at the position of shocklets and two positive peaks at the front and back of shocklets. The reason why the Reynolds stress term and the entropy term are canceled out each other and the viscous term shows different trend are explained using one-dimensional shock relation with the Lighthill's turbulent stress tensor (Eq. 4.5). Let (1) be the upstream value and (2) be the downstream value of the shock (Fig. 4.19). In one dimension, the Reynolds stress component of the Lighthill's turbulent stress tensor is written as ρu^2. The mass conservation law $\rho_{(1)} u_{(1)} = \rho_{(2)} u_{(2)}$ leads to a conclusion that the ratio of the Reynolds stress components across shock is the same as that of the velocity. Also, the ratio of the entropy components of the Lighthill's turbulent stress tensor across shock is determined by the pressure ratio and the density ratio. The shock relation of density, velocity and pressure are written as follows:

$$\begin{aligned} \frac{\rho_{(2)}}{\rho_{(1)}} &= \frac{(\gamma+1)M_{(1)}^2}{(\gamma-1)M_{(1)}^2+2} = \frac{u_{(1)}}{u_{(2)}}, \\ \frac{p_{(2)}}{p_{(1)}} &= \frac{2\gamma M_{(1)}^2 - (\gamma-1)}{\gamma+1}. \end{aligned} \tag{4.13}$$

As $p_{(2)}/p_{(1)} > \rho_{(2)}/\rho_{(1)} > 1$, the change direction across shock of the entropy components $((p-p_0) - c_0^2(\rho-\rho_0))$ is the same as that of density (or pressure). (Eq. 4.13) shows that the change direction of density across shock is the opposite to that of velocity. Therefore, the change direction across shock of the Reynolds stress component (same as velocity) is opposite to that of the entropy component (same as density), then each term is canceled out each other across shock. In addition, the viscous component in one-dimension is written as $\mu \partial u/\partial x$. As the change in μ across shocklets is small compared to that of the first derivative of velocity, the viscosity is assumed to be constant across shock. Thus, the distribution of viscous component corresponds to that of the first derivative of velocity. The discussion above showed that the ratio of the Reynolds stress component across shock is the same as that of velocity. Thus, the first derivative of the Reynolds stress term distribution in Fig. 4.18 should correspond to that of the viscous

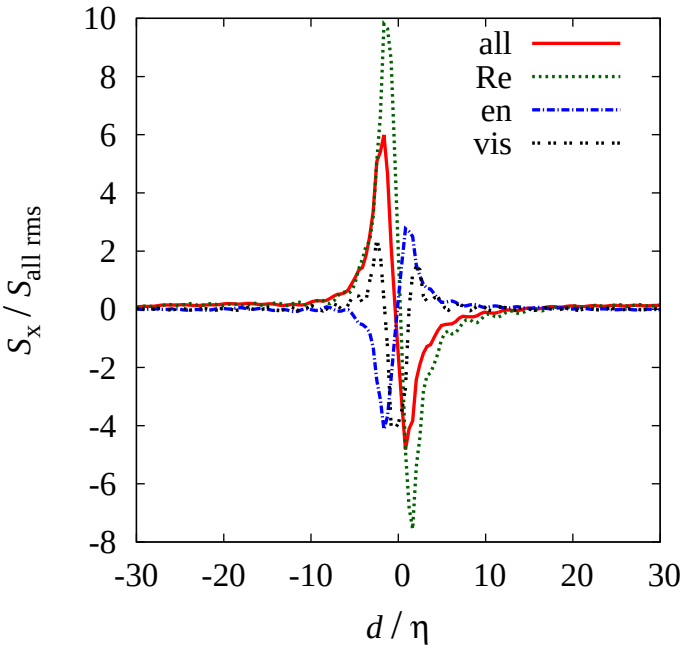

Figure 4.18: Sound source distributions across shocklets for $M_{t0} = 1.0, R_{\lambda 0} = 130$: —, term total S_{all}; $\cdots$, Reynolds stress term S_{Re}; $-\cdot-$, entropy term S_{en}; $\cdot\cdot\,\cdot\cdot$, viscous term S_{vis}. The values are normalized by rms value of term total $S_{\mathrm{all\ rms}}$. The positive d and the negative d show the upstream and the downstream of shocklets.

term distribution. The positive slope at the front and back of shocklets and the negative slope near shocklets are observed in the distribution of the Reynolds stress term. If the first derivative of the distribution is considered, two positive peaks at the front and back of shocklets and one negative peak at near the center of shocklets are derived for the viscous term distribution. The distribution of the viscous term in Fig. 4.18 supports the explanation above.

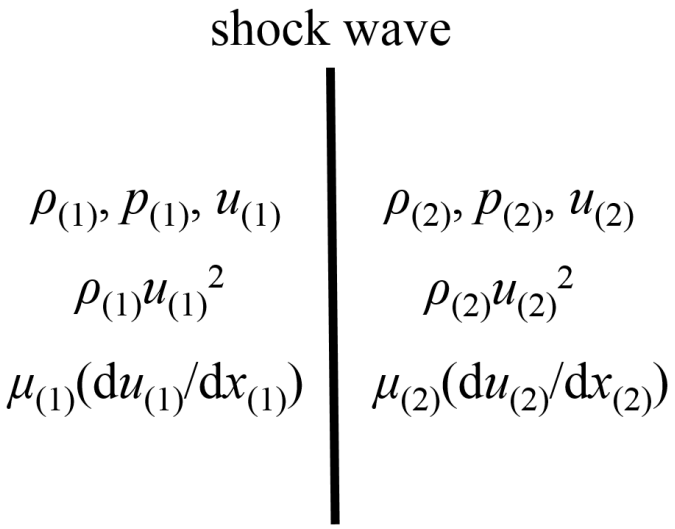

Figure 4.19: Schematic of physical quantities across one-dimensional shock. (1) is for the upstream value and (2) is that for the downstream.

Finally, the Mach number and the Reynolds number dependence on sound sources across shocklets are investigated. Fig. 4.20 shows that the sound source distributions across shocklets with five different turbulent Mach numbers. All terms show larger values with increasing the Mach number due to the appearance of stronger shocklets for the higher turbulent Mach number cases. The Reynolds number dependence is also shown in Fig. 4.21. The trend is the same as that of the turbulent Mach number. Larger Reynolds number shows larger values of sound sources. Lee *et al.*[48] showed that higher Reynolds number leads to more frequent large compression events of shocklets. Therefore, the higher Reynolds numbers also cause stronger shocklets, and then, the stronger sound sources are created. Note that the contribution of the viscous term would become smaller for the higher Reynolds number flows due to the smaller viscosity μ, though, the trend was not observed in the present range of the Reynolds number.

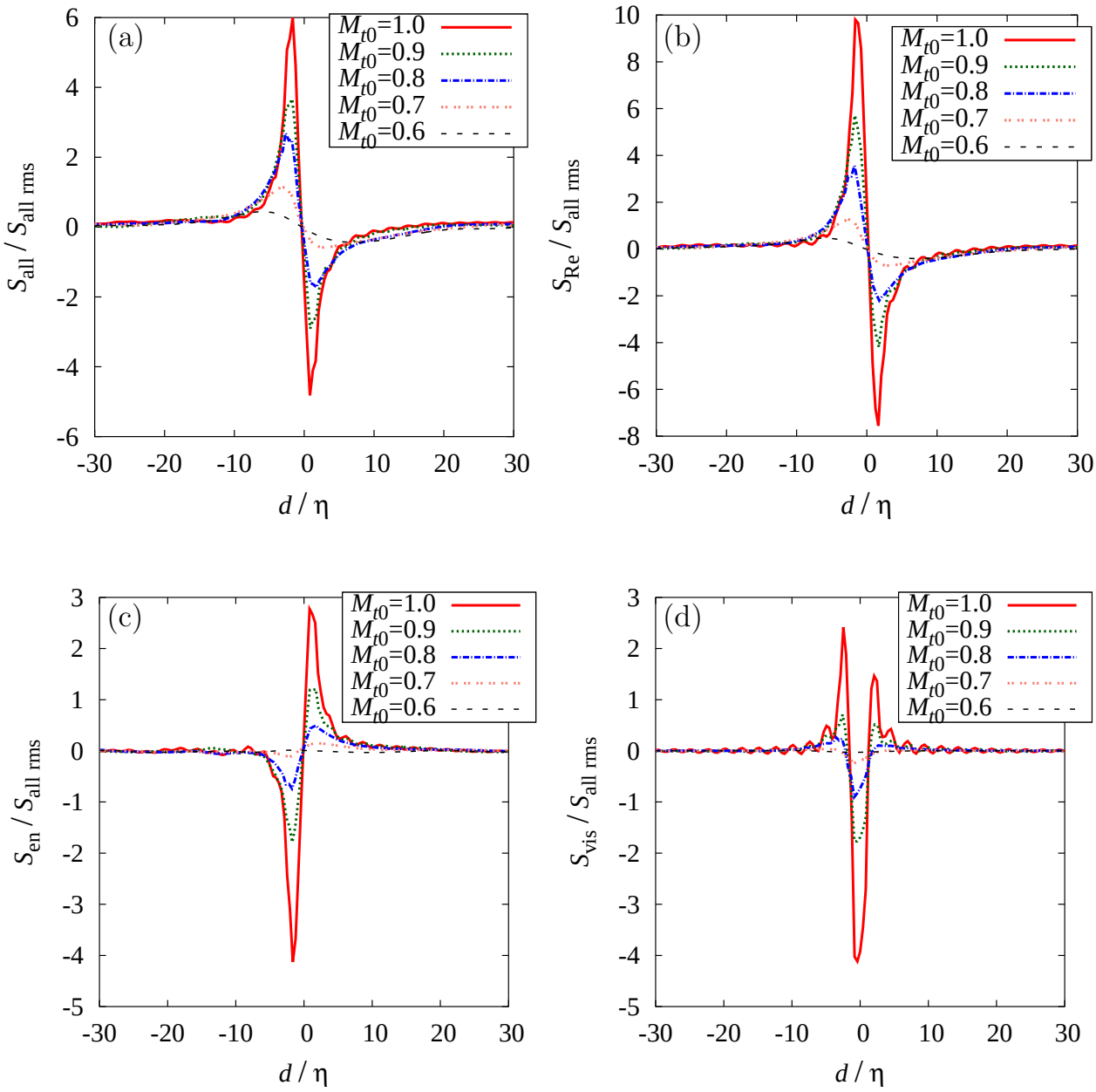

Figure 4.20: Turbulent Mach number dependence on sound sources across shocklets for $R_{\lambda 0} = 130$: —, $M_{t0} = 1.0$; ···, $M_{t0} = 0.9$; – · –, $M_{t0} = 0.8$; ·· ··, $M_{t0} = 0.7$; – –, $M_{t0} = 0.6$. (a) Term total $S_{\rm all}$, (b) Reynolds stress term $S_{\rm Re}$, (c) entropy term $S_{\rm en}$ and (d) viscous term $S_{\rm vis}$. The values are normalized by rms value of term total $S_{\rm all\ rms}$. The positive d and the negative d show the upstream and the downstream of shocklets.

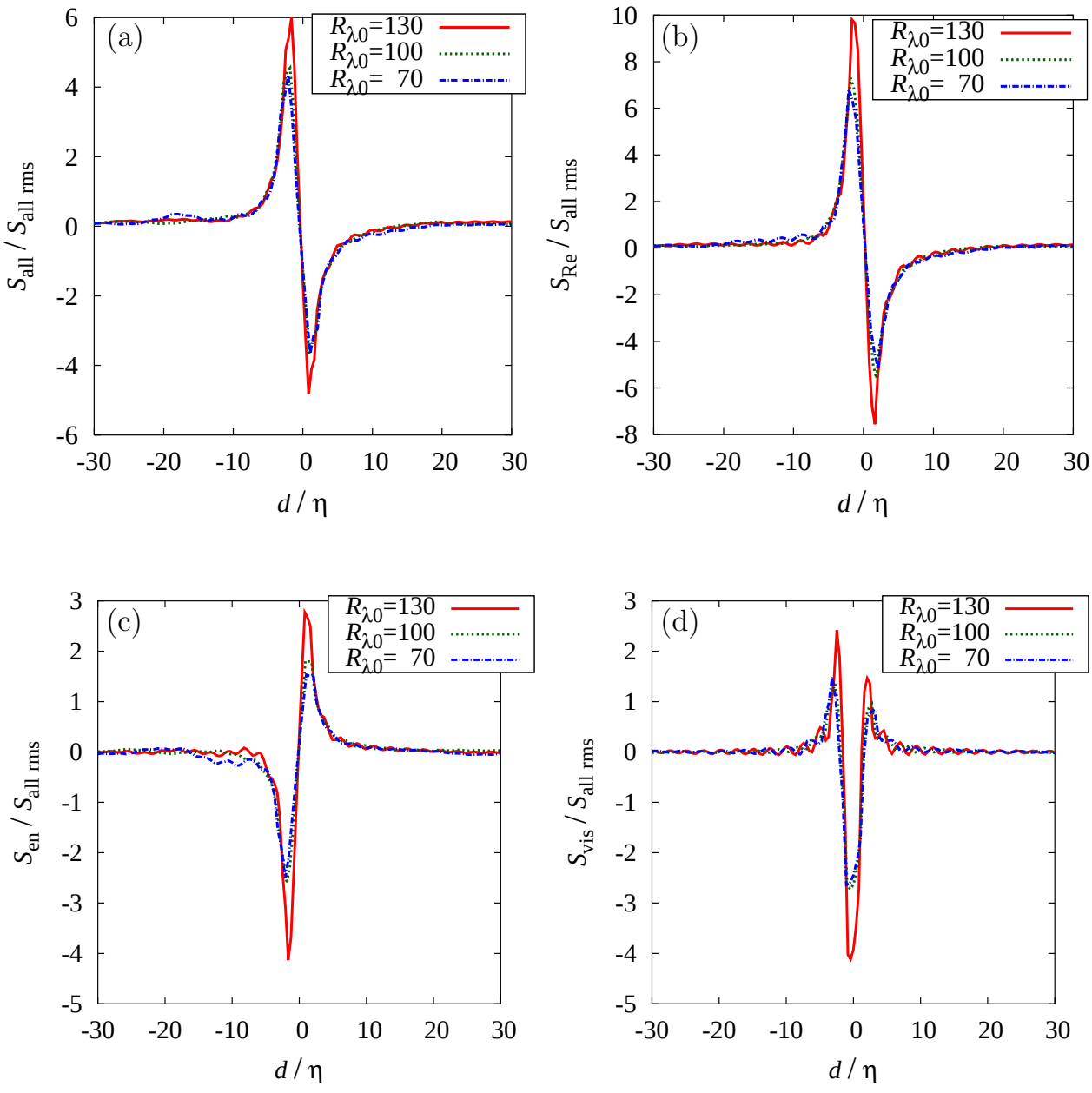

Figure 4.21: Reynolds number dependence on sound sources across shocklets for $M_{t0} = 1.0$: —, $R_{\lambda 0} = 130$; ···, $R_{\lambda 0} = 100$; –·–, $R_{\lambda 0} = 70$. (a) Term total $S_{\rm all}$, (b) Reynolds stress term $S_{\rm Re}$, (c) entropy term $S_{\rm en}$ and (d) viscous term $S_{\rm vis}$. The values are normalized by rms value of term total $S_{\rm all\ rms}$. The positive d and the negative d show the upstream and the downstream of shocklets.

4.5 Summary of this chapter

In this chapter, sound source characteristics in the isotropic compressible turbulence were analyzed to understand the effects of the turbulent Mach numbers. It was shown that two sound sources appear depending on the turbulent Mach numbers.

In the lower turbulent Mach number flows, vortices are the main sound sources, so that the Reynolds stress term is one of the main sound sources in the lower turbulent Mach numbers as expected. In addition, the entropy term cannot be negligible even in the lower turbulent Mach numbers. This is because the terms ($\kappa\nabla^2 T$ and ε) related with the diffusion processes (and so temperature) cause non-uniform entropy field. Only density is affected by the change in temperature, because the pressure contribution of the entropy term is determined by velocity field in the form of Poisson equation in nearly incompressible flows. As the distributions of density contributions of the entropy term and the Reynolds stress term become partially similar, the Reynolds stress term and the entropy term are partially intensified each other. Note, however, that the contributions of the entropy term would become smaller for the higher Reynolds number flows due to the smaller values of the thermal conductivity and the viscosity, though the trend was not observed in the present range of the Reynolds number. Also, the smaller scales and larger peak values in sound sources appear with increasing the Reynolds number due to more active turbulent motion.

In the higher turbulent Mach numbers, on the other hand, eddy-shocklets become important sound sources in addition to vortices. All source terms show strong values across or on shocklets. It is, however, noted that the contribution of the viscous term for the higher Reynolds number would become smaller, because of the smaller viscosity, though the trend also did not appear in the range of the present Reynolds number. The Reynolds stress term and the entropy term are canceled out each other near shocklets region. By using one-dimensional shock relation, the reason why the canceling out of those two terms were explained. In addition, the distribution of the viscous term across shocklets were explained as well. The higher turbulent Mach number and the Reynolds number lead to the stronger shocklets, and then stronger sound sources.

Chapter 5

Sound source characteristics in temporally evolving compressible mixing layer

In this chapter, the convective Mach number and the density (temperature) ratio dependence on sound sources and generated acoustic wave characteristics are investigated by DNS of the temporally evolving compressible mixing layer. Simulation parameters are shown in Tab. 5.1. We compute total 7 cases. The series TA corresponds to the isothermal mixing layer in which densities at the upper and lower streams are the same, whereas the series TB is for the variable density ratio cases. The case TB03 is used for the purpose of validation. The normalization is conducted by the averaged value of density $\rho_{\mathrm{ave}} = 1/2(\rho_1 + \rho_2)$, the velocity difference Δu and the momentum thickness δ_θ, unless otherwise noted.

5.1 Validation

In the temporally evolving compressible mixing layer simulations, the validation study was conducted by using nearly incompressible cases[6, 72, 85, 8] due to the existence of some DNS databases and the corresponding experiments. We also follow the way to validate the present computation. Fig. 5.1 shows the time history of the momentum thickness (Eq. 2.16) for the validation case of TA03. The time is normalized by the velocity difference Δu and the initial momentum thickness $\delta_{\theta 0}$. After a transient, the plot shows almost linear growth at $\delta_\theta/\delta_{\theta 0} = 6 - 11$. The linear growth indicates that the flow reaches the self-similar state, so that the validation study is conducted using

Case	M_c	s	M_t	Re_θ	$L_x \times L_y \times L_z$	$N_x \times N_y \times N_z$	$\eta/\Delta x$
TA03	0.3	1	0.13	1741	$343 \times 692 \times 86$	$512 \times 1025 \times 128$	0.27
TA12	1.2	1	0.37	3106	$343 \times 692 \times 86$	$512 \times 1025 \times 128$	0.42
TA15	1.5	1	0.53	3150	$343 \times 692 \times 86$	$512 \times 1025 \times 128$	0.45
TA18	1.8	1	0.56	3167	$343 \times 692 \times 86$	$512 \times 1025 \times 128$	0.59
TB02	1.5	2	0.48	3116	$343 \times 692 \times 86$	$512 \times 1025 \times 128$	0.55
TB04	1.5	4	0.37	3073	$343 \times 692 \times 86$	$512 \times 1025 \times 128$	0.71
TB08	1.5	8	0.37	2651	$343 \times 692 \times 86$	$512 \times 1025 \times 128$	0.77

Table 5.1: Parameters used in the direct numerical simulation. M_c is the convective Mach number, s is the density ratio, M_t is the turbulent Mach number computed at the center of the mixing layer, $L_x \times L_y \times L_z$ is the computational domain based on the initial momentum thickness $\delta_{\theta 0}$, $N_x \times N_y \times N_z$ is the resolution, Δx is the grid spacing in the x direction, and η is the Kolomogorov length scale. Values for the Reynolds number based on the momentum thickness Re_θ, the turbulent Mach number M_t, and the resolution parameter $\eta/\Delta x$ are those at the final time of the computations.

the averaged values at the time period. The mean streamwise velocity with previous DNS data and an experimental data are shown in Fig. 5.2. The result of the present DNS shows very good agreement with the previous works. To discuss the validity for the turbulent statistics, the Reynolds stress is considered. The Reynolds stress is defined as follows:

$$R_{ij} = \frac{\overline{\rho u_i'' u_j''}}{\bar{\rho}}, \tag{5.1}$$

where $()''$ denotes the Favre fluctuation. In Fig. 5.3 and Fig. 5.4, various components of the Reynolds stress are shown with the previous studies. Again, the trend and the peak values in the present DNS are in good agreement with the previous studies. Also, the resolution parameter defined by the grid spacing and the Kolmogorov length scale $\eta/\Delta x$ is the order of unity for all cases, so that the criteria of the DNS simulation is satisfied in the present computation. Therefore, the present computation is well validated.

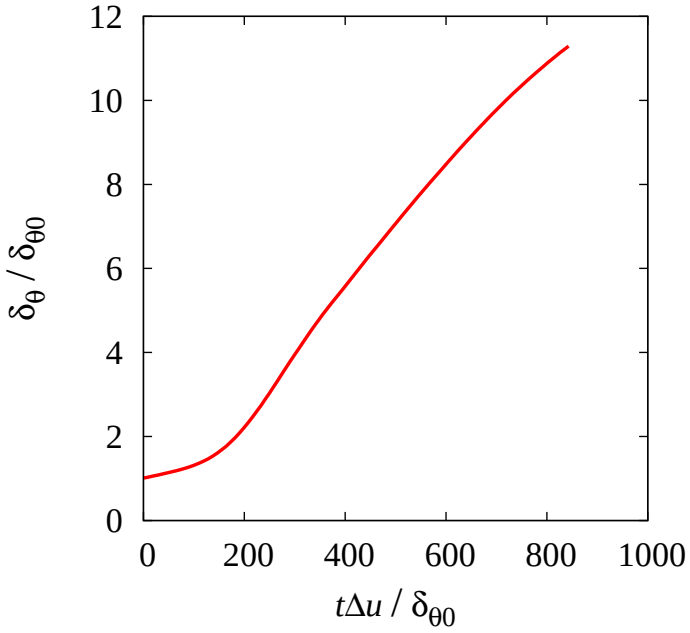

Figure 5.1: Time history of the momentum thickness for TA03.

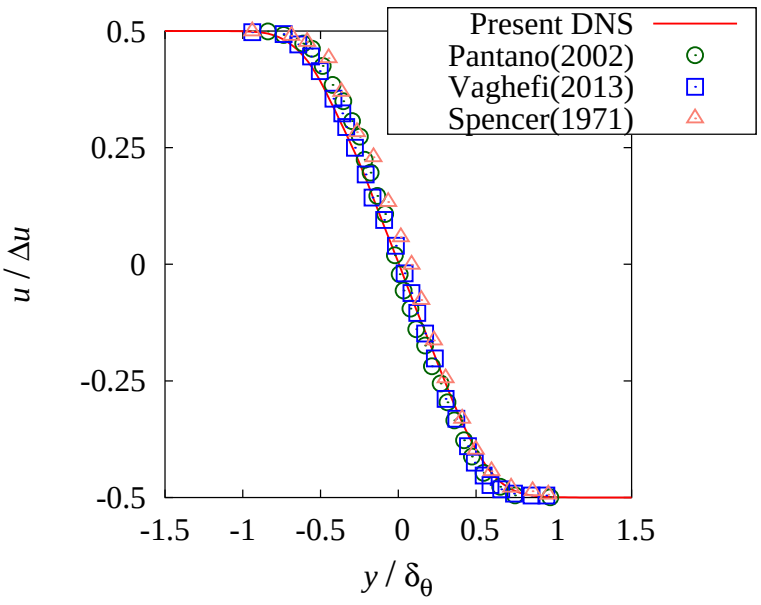

Figure 5.2: Normalized mean streamwise velocity $u/\Delta u$ for TA03: —, present DNS; ◯, previous DNS by Pantano and Sarkar[6]; □, previous DNS by Vaghefi *et al.*[8]; △, previous experiment by Spencer and Jones[9].

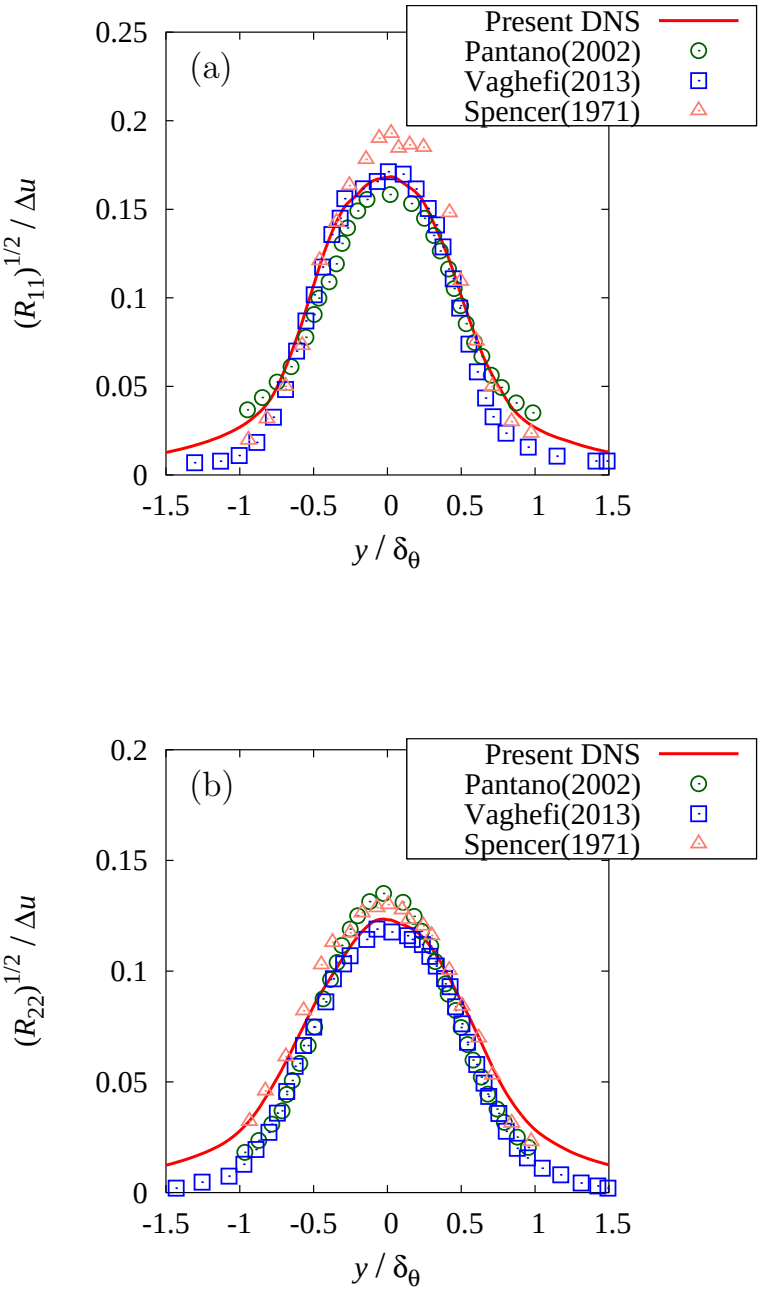

Figure 5.3: Normalized Reynolds stress components of (a) $\sqrt{R_{11}}/\Delta u$ and (b) $\sqrt{R_{22}}/\Delta u$ for TA03: —, present DNS; ◯, previous DNS by Pantano and Sarkar[6]; □, previous DNS by Vaghefi *et al.*[8]; △, previous experiment by Spencer and Jones[9].

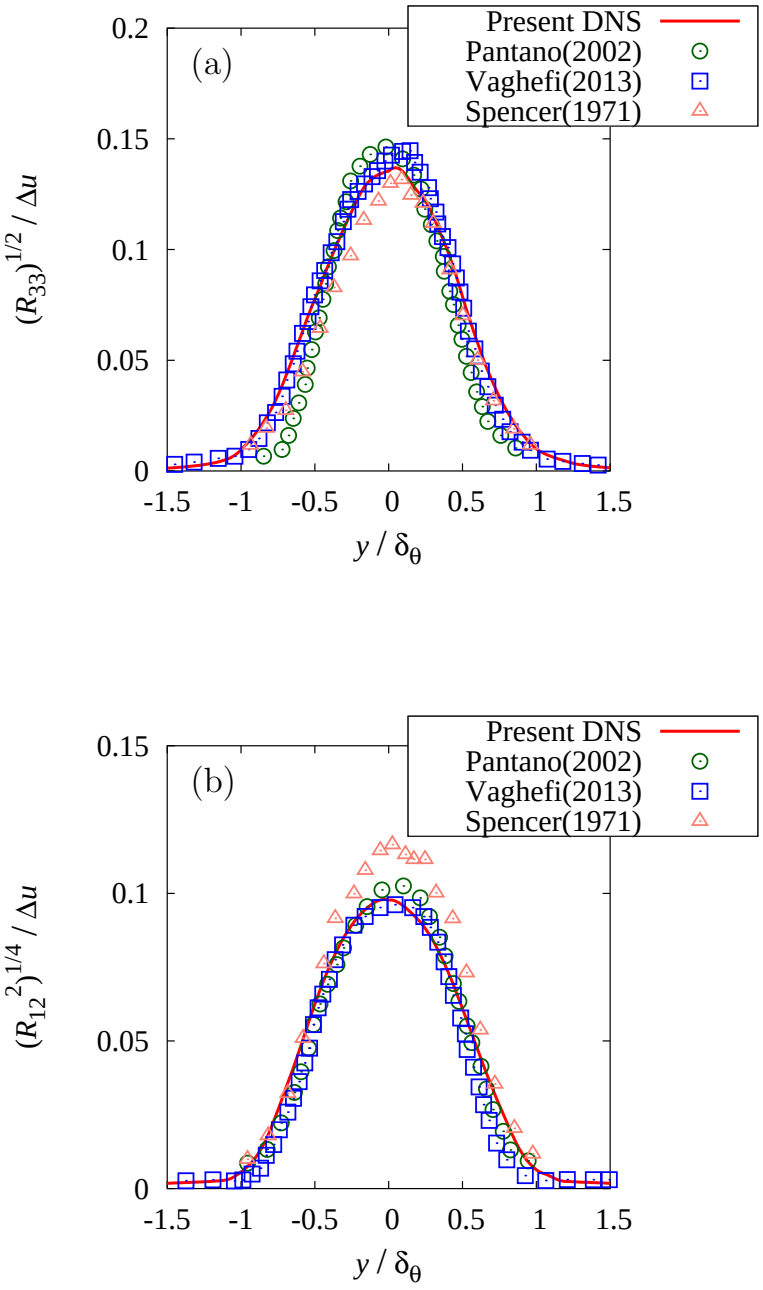

Figure 5.4: Normalized Reynolds stress components of (a) $\sqrt{R_{33}}/\Delta u$ and (b) $\sqrt{R_{12}}/\Delta u$ for TA03: —, present DNS; ◯, previous DNS by Pantano and Sarkar[6]; □, previous DNS by Vaghefi *et al.*[8]; △, previous experiment by Spencer and Jones[9].

5.2 Convective Mach number dependence on sound sources

In this subsection, the convective Mach number dependence is analyzed. As the first topic of this subsection, the development flow is discussed. Fig. 5.5 shows the time history of the momentum thickness for the isothermal mixing layer. The lines show almost linear trend after $\delta_\theta/\delta_{\theta 0} = 14$ which implies flow reaches a quasi-steady state. Flow visualization also confirms the fact (Fig 5.6). In this figure, we show the iso-surface of the second invariant of the velocity gradient tensor and a cross section of the dilatation at $\delta_\theta/\delta_{\theta 0} = 6, 8, 16$. Note that the incompressible version of the second invariant of the velocity gradient tensor (Eq. 4.8) is used to extract only the strong rotational motion of fluids. This configuration can remove the uncertainties to extract the highly compression (i.e. shocklets) or expansion of fluids by the original version (Eq. 4.7), so that it enables us to focus only on the vortical structure. Although, the time of transient has some dependence on cases, the results show that the turbulent transition occur at around $\delta_\theta/\delta_{\theta 0} = 6 - 8$ for all cases, and then the flows become fully turbulent state. At the fully turbulent state, some differences are observed. For flow field, vortices become sparser with increasing the convective Mach number. For acoustic waves, two remarkable differences are observed. One is the weaker acoustic waves at the far field with increasing the convective Mach number. The other is is that the near field dilatation for $M_c = 1.5, 1.8$ shows rather fluctuated properties than the case of $M_c = 1.2$. The detail discussion for the difference is conducted in the following. Firstly, the characteristics of flow field is analyzed by the energy spectra, and then, the characteristics of sound sources and the generated acoustic waves are investigated.

5.2.1 Energy spectra

Fig. 5.6 showed that vortices become sparser with increasing the convective Mach number. Here, the flow field is analyzed by the energy spectra. The spectra are computed at the center of the mixing layer and averaged at the time period $\delta_\theta/\delta_{\theta 0} = 14 - 20$. Note that the center of the mixing layer is defined as the position of $\overline{u}_1 = 0$. Fig. 5.7 (a) shows the streamwise energy spectra normalized by the momentum thickness. The spectra at the higher wave numbers do not collapse between cases. Kleinman *et al.*[65] showed that the energy spectra of different Reynolds number cases collapse well with the scaling of the Taylor micro scale (see App. C for the derivation of the Taylor micro scale) in their $M_c = 0.45$ simulation. The same scaling is conducted here. The Taylor micro scale in

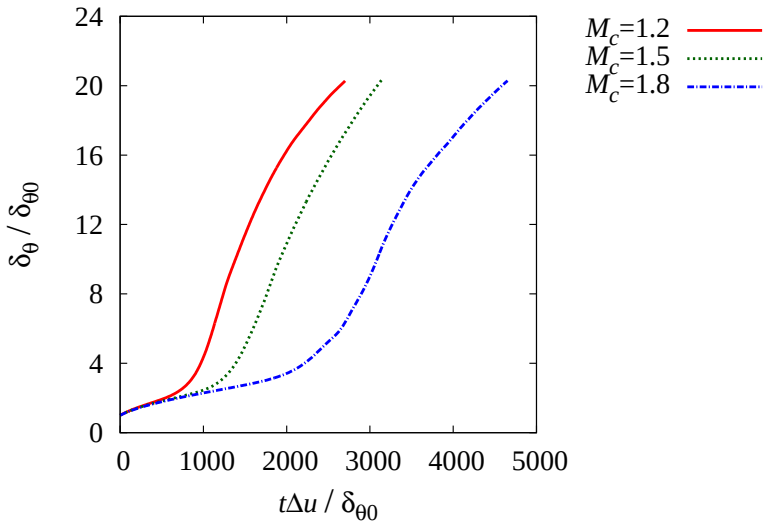

Figure 5.5: Time history of momentum thickness for isothermal mixing layer:—, TA12; ···, TA15; – · –, TA18.

the x direction is defined as;

$$\lambda_x = \sqrt{\frac{\overline{u_1'' u_1''}}{\overline{\frac{\partial u_1''}{\partial x_1}\frac{\partial u_1''}{\partial x_1}}}}, \tag{5.2}$$

and in the z direction is defined as;

$$\lambda_z = \sqrt{\frac{\overline{u_3'' u_3''}}{\overline{\frac{\partial u_3''}{\partial x_3}\frac{\partial u_3''}{\partial x_3}}}}. \tag{5.3}$$

The streamwise energy spectra scaled with the Taylor micro scale are shown in Fig. 5.7 (b). The spectra collapse well between cases, so that the scaling with the Taylor micro scale is also applicable for the scaling of the different convective Mach number cases. The spanwise energy spectra show the same trend as that of the streamwise spectra (Fig. 5.8).

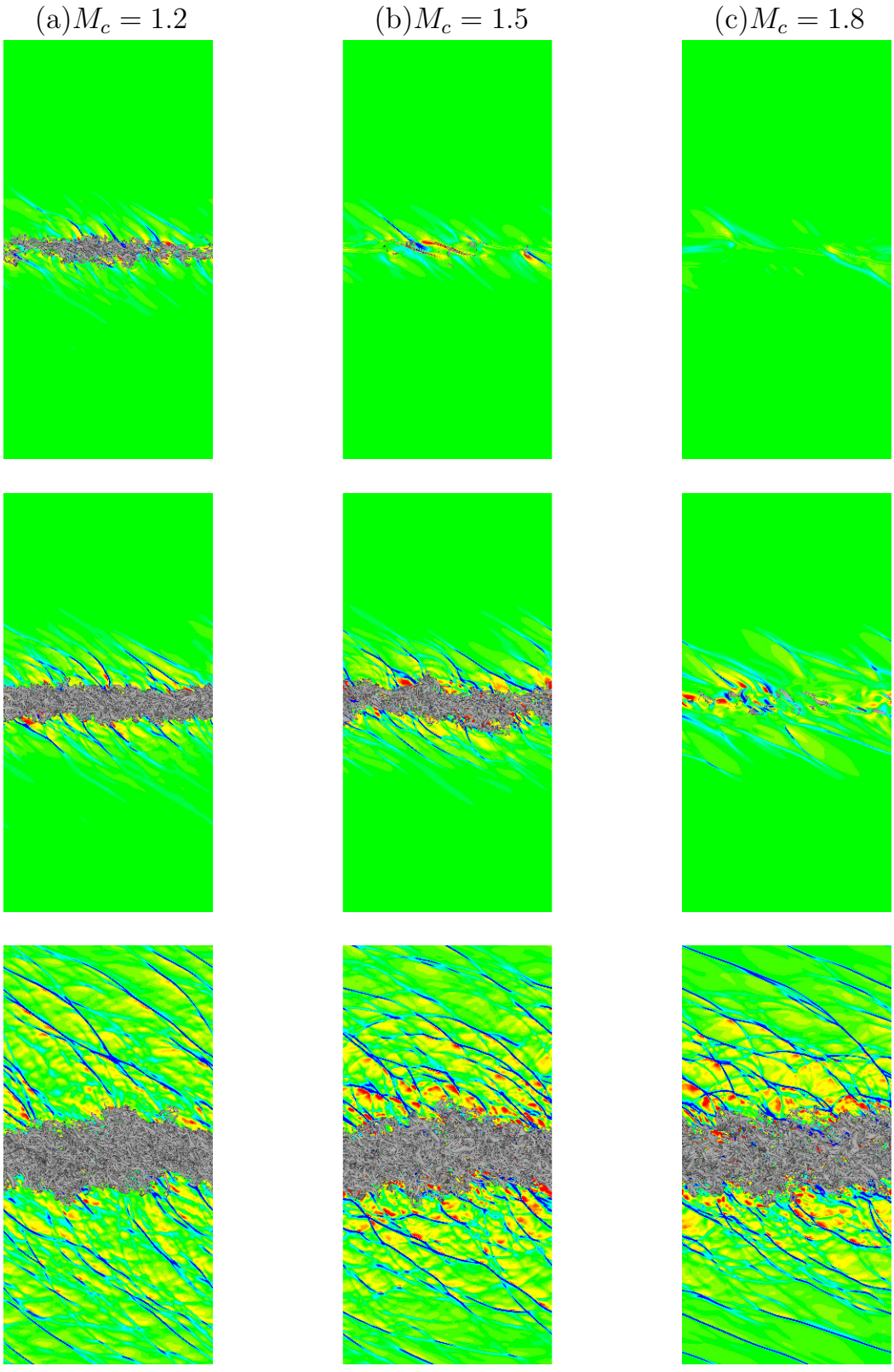

Figure 5.6: Normalized iso-surface of incompressible second invariant of the velocity gradient tensor $Q_{\text{inc}}/\Delta u^2 \times \delta_\theta^2 = 0.05$ and normalized dilatation $\nabla \cdot \mathbf{u}/\Delta u \times \delta_\theta$ at $z = z_{\max}$ for (a) TA12, (b) TA15 and (c) TA18. The contour range of dilatation is from -0.1 to 0.1. The corresponding times from top to bottom are $\delta_\theta/\delta_{\theta 0} = 6$, $\delta_\theta/\delta_{\theta 0} = 8$ and $\delta_\theta/\delta_{\theta 0} = 16$, respectively.

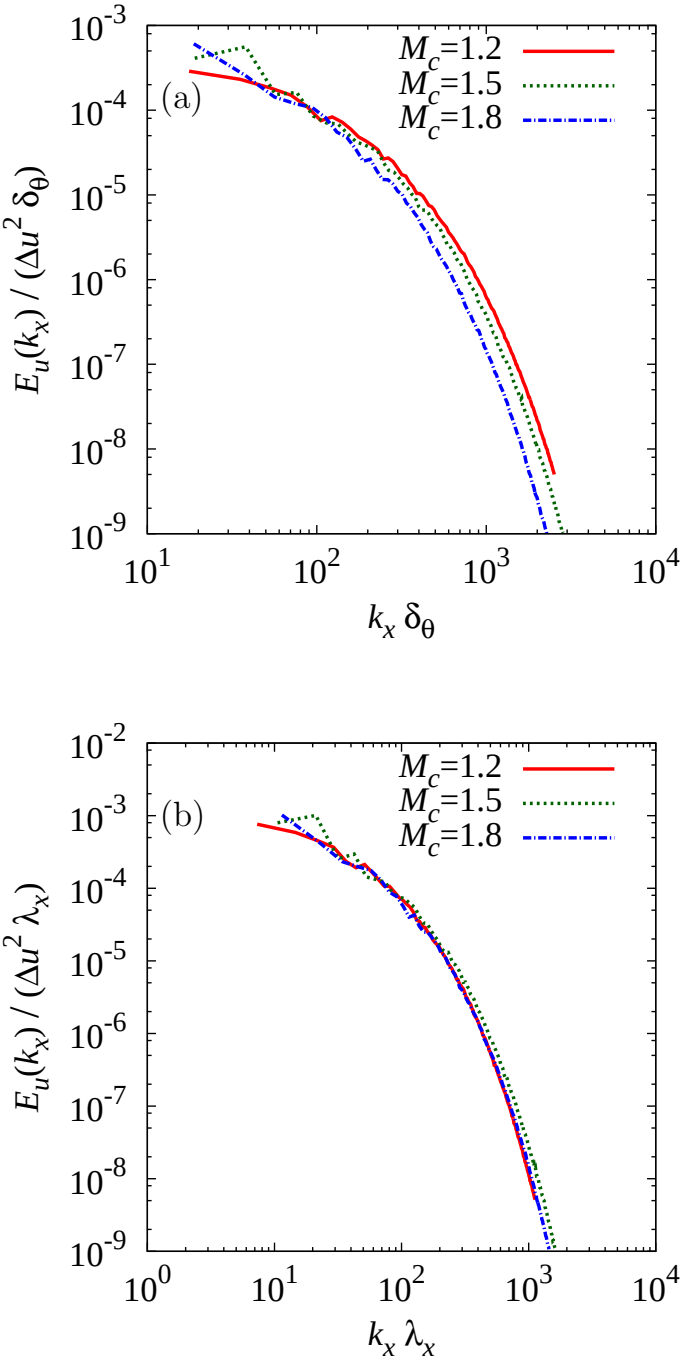

Figure 5.7: Scaled streamwise energy spectra at the center of mixing layer:—, TA12; ···, TA15; – · –, TA18. The spectra are scaled with (a) momentum thickness and (b) Taylor micro scale.

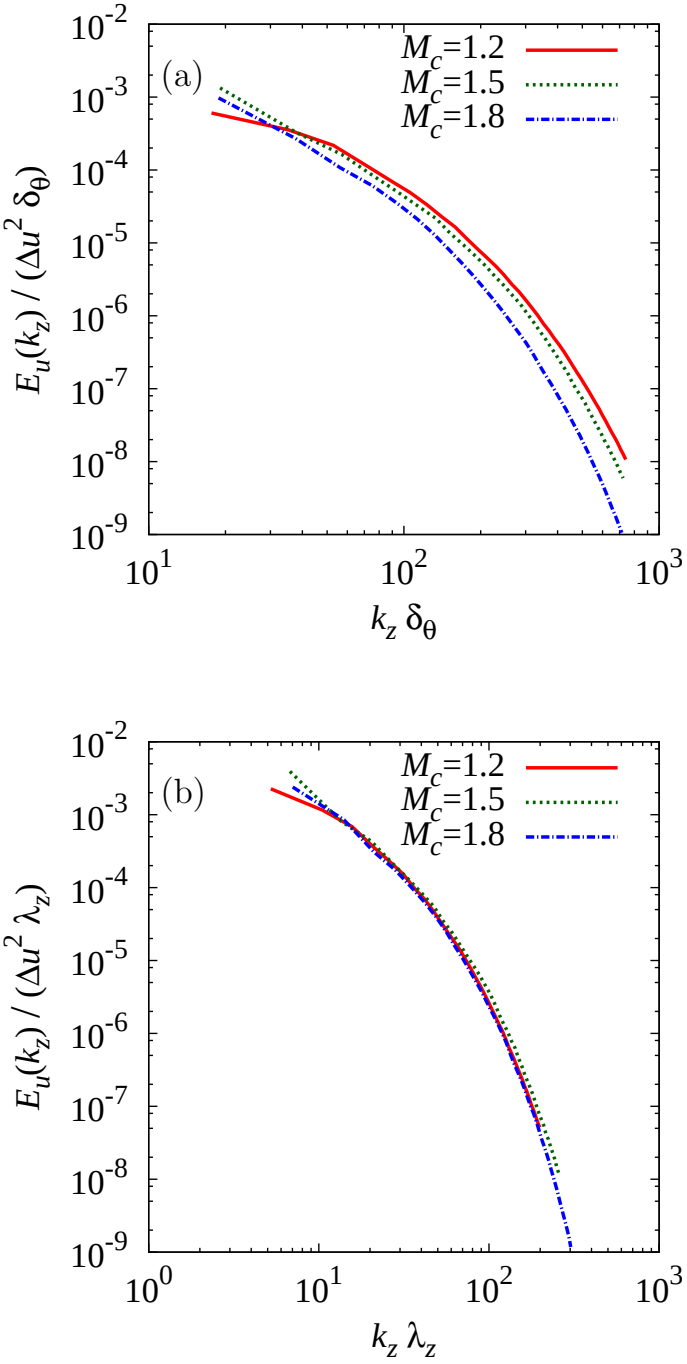

Figure 5.8: Scaled spanwise energy spectra at the center of mixing layer:—, TA12; ···, TA15; – · –, TA18. The spectra are scaled with (a) momentum thickness and (b) Taylor micro scale.

5.2.2 Acoustic waves and sound sources

The visualization in Fig. 5.6 showed highly fluctuated dilatation at the near field for $M_c \geq 1.5$. Also, the weaker dilatation level at the far field was observed with increasing the convective Mach number. In this subsection, the characteristics of acoustic waves are analyzed with the source terms of the Lighthill equation. The source terms of the Lighthill equation in the isothermal mixing layer is written as;

$$\begin{aligned} S_{\mathrm{Re}} &= \frac{\partial \rho u_i u_j}{\partial x_i \partial x_j}, \\ S_{\mathrm{en}} &= \frac{\partial(\delta_{ij}[p - p_{\mathrm{ave}} - c^2_{\mathrm{ave}}(\rho - \rho_{\mathrm{ave}})])}{\partial x_i \partial x_j}, \\ S_{\mathrm{vis}} &= \frac{\partial\left(\mu\left(\frac{\partial u_i}{\partial x_j}\frac{\partial u_j}{\partial x_i} - \frac{2}{3}\delta_{ij}\frac{\partial u_k}{\partial x_k}\right)\right)}{\partial x_i \partial x_j}, \\ S_{\mathrm{all}} &= S_{\mathrm{Re}} + S_{\mathrm{en}} + S_{\mathrm{vis}}, \end{aligned} \tag{5.4}$$

where $()_{\mathrm{ave}}$ denotes the averaged value of the upper and lower streams. Before the discussion of the sound sources, we show the averaged pressure fluctuations with three different Mach number cases in Fig. 5.9. Far field acoustic waves become weaker with increasing the Mach number. The trend of the overall sound sources (Fig. 5.10), the Reynolds stress term (Fig.5.11 (a)) and the entropy term (Fig. 5.11 (b)) is the same as that of far field pressure. Note that the viscous term is omitted due to its negligible value. The results imply that the decrease of sound source strength is a cause for the weaker far field acoustic waves.

One reason for the weaker sound source strength with increasing the convective Mach number would be caused by the change in vortices. The visualization in Fig. 5.6 showed that vortices become sparser structures with increasing the convective Mach number. For the statistics, Fig. 5.12 shows that the rms values of the incompressible second invariant of the velocity gradient tensor. The trend is the same as that of sound sources in which the values become smaller with increasing the convective Mach number. Thus, the suppression of the vortices with increasing the convective Mach number is a cause for the weaker sound sources, and then weaker far field acoustic waves. Note that the slight difference near zero position between the incompressible second invariant and the source terms is observed. This is because the density at the center of the mixing layer becomes smaller with increasing the convective Mach number.

After understanding the acoustic wave strength, we focus on the characteristics of spectra. The averaged far field spectra obtained at $y/\delta_{\theta 0} = \pm 346$ are used for the

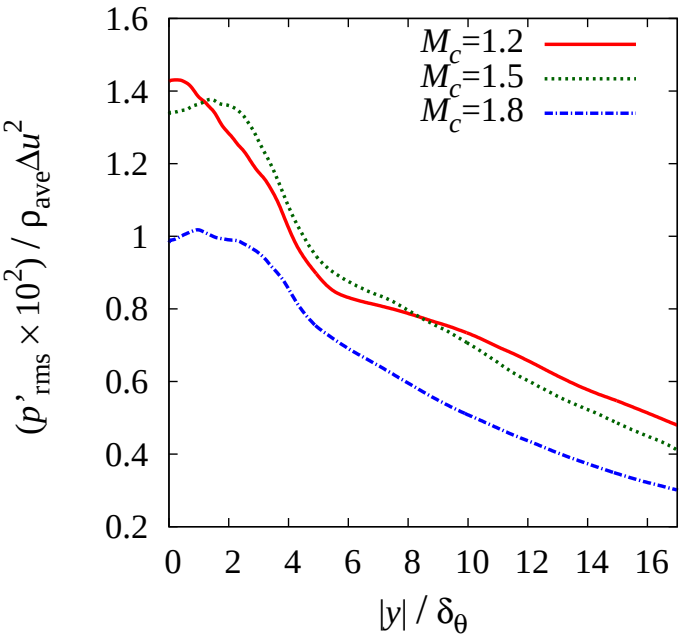

Figure 5.9: Averaged pressure fluctuations in the y direction for three different convective Mach numbers:—, $M_c = 1.2$; ···, $M_c = 1.5$; – · –, $M_c = 1.8$. The values are obtained by averaging the values of both upper and lower directions.

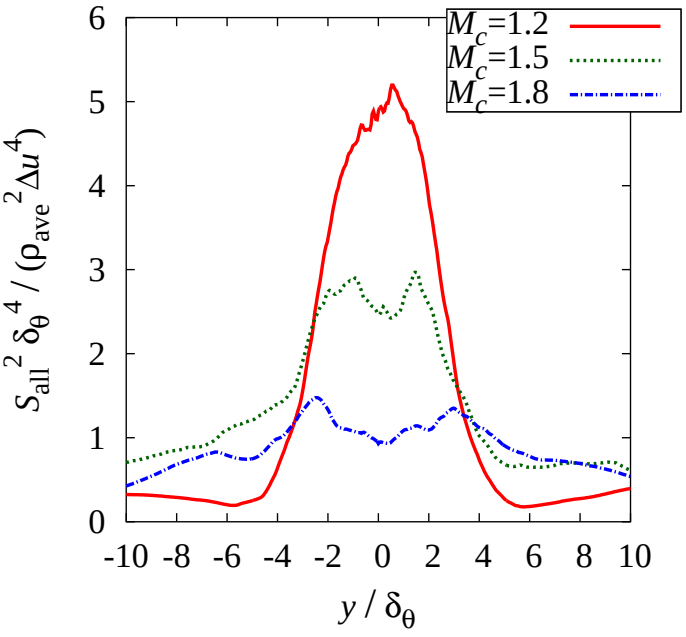

Figure 5.10: Averaged overall sound source strength in the y direction for three different convective Mach numbers:—, $M_c = 1.2$; ···, $M_c = 1.5$; – · –, $M_c = 1.8$.

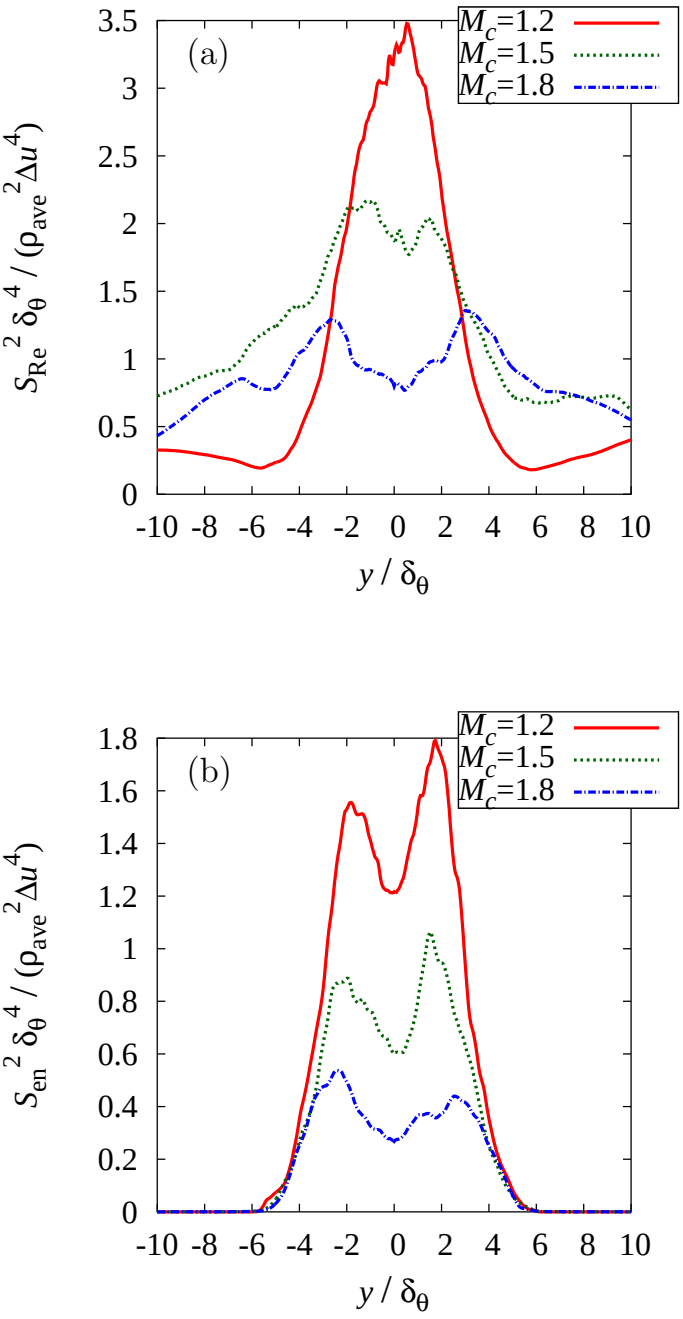

Figure 5.11: Averaged sound source strength of (a) Reynolds stress term and (b) entropy term in the y direction for three different convective Mach numbers:—, $M_c = 1.2$; $\cdots$, $M_c = 1.5$; $-\cdot-$, $M_c = 1.8$.

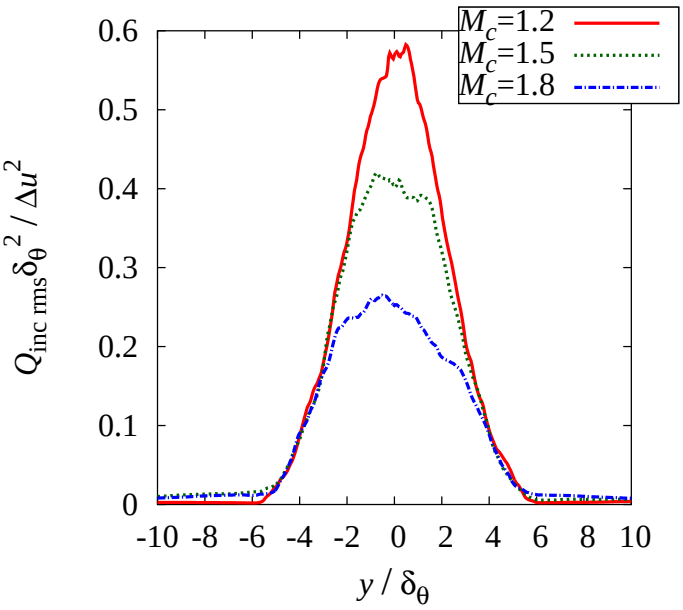

Figure 5.12: Averaged incompressible second invariant of the velocity gradient tensor in the y direction for three different convective Mach numbers:—, $M_c = 1.2$; $\cdots$, $M_c = 1.5$; $-\cdot-$, $M_c = 1.8$.

discussion. How the averaging is conducted is briefly mentioned here. The averaged values of spectra are obtained by averaging the acoustic waves generated after $\delta_\theta/\delta_{\theta 0} = 10$ by considering the retarded time. Here, the similar scalings of the energy spectra with the momentum thickness and the Taylor micro scale are also applied to the pressure spectra. Fig. 5.13 shows the scaled far field pressure spectra with the momentum thickness and the Taylor micro scale. The scaling with the Taylor micro scale also collapse well in a wide range of wave numbers. However, some differences appear in the higher wave numbers in Fig. 5.13 (b) for $M_c \geq 1.5$, so that the smaller scale acoustic waves (based on the Taylor micro scale) appear in those cases. The same trend also appears for the spanwise pressure spectra (Fig. 5.14). There are two possible reasons for the higher wave number components to appear in the far field pressure spectra. One is the non-linear propagation effects, and the other is the appearance of the smaller scale sound sources. The former needs some distance for affecting the spectra significantly[57, 38, 66], so that the significant effects by the non-linear propagation could not be possible due to the limited computational domain of the present simulation. Thus, we focus on the other possibility of the change in the scales of sound sources. Figs. 5.15 and 5.16 show sound source spectra scaled with the Taylor micro scale in the streamwise and the spanwise directions, respectively. The smaller wave number components clearly appear in almost all figures. Only the spanwise spectra of the term total and the entropy term do not show clear smaller wave number components. The trend, however, is very similar to the

flows with shocklets in the isotropic compressible turbulence (Fig. 4.5). The spectra of the term total and the entropy term are less affected by shocklets than that of the Reynolds stress term and the viscous term. Thus, the effects of shocklets would be a possible explanation for the change in the acoustic wave characteristics. One of the important characteristics of sound sources by shocklets is that the canceling out between the Reynolds stress term and the entropy term. To analyze it, the averaged values of the term total in sound source strength are obtained by the integration of the profiles of Fig. 5.10. In a similar way, we have the the strength of the other terms. By using the obtained sound source strength, the contribution of the each term to the overall sound source strength is shown in Fig. 5.17. The contribution of the Reynolds stress term for $M_c = 1.8$ reaches almost unity. This implies that the canceling out between the Reynolds stress term and the entropy term for the case, because the value of the entropy term contribution has non-negligible value and the contribution of viscous term is negligible. This results support that, at least, the case $M_c = 1.8$ shows the characteristics of sound sources by shocklets (Fig. 4.2). The averaged rms of dilatation (Fig. 5.18) with three different convective Mach numbers also shows the trend of the occurrence of shocklets. The results clearly show that the higher values of dilation for $M_c \geq 1.5$. The scaled (with Taylor micro scale) streamwise and spanwise spectra of dilatation at the center of the mixing layer (Fig. 5.19) show that the higher wave number components for the higher convective Mach numbers. These also suggest that the occurrence of shocklets in the flow field for the higher convective Mach numbers.

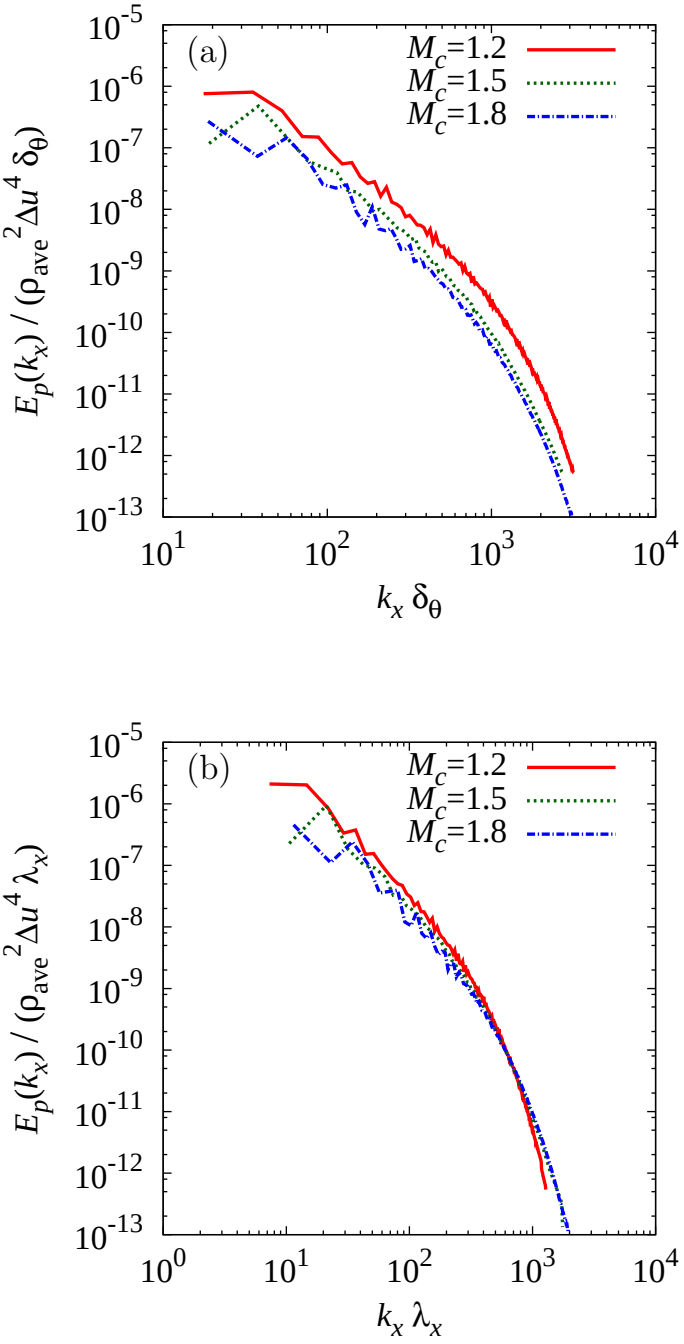

Figure 5.13: Scaled streamwise pressure spectra at $y/\delta_{\theta 0} = \pm 346$ for three different convective Mach numbers:—, TA12; ···, TA15; – · –, TA18. The values are scaled with (a) momentum thickness and (b) Taylor micro scale.

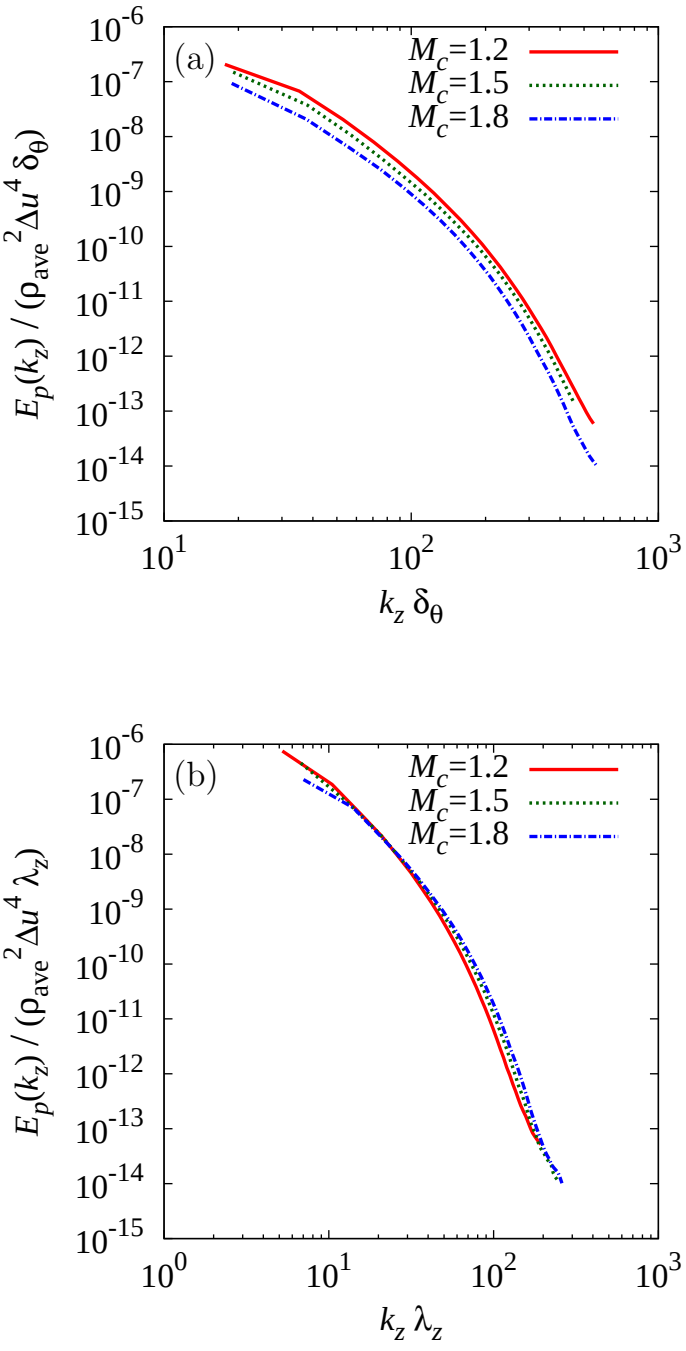

Figure 5.14: Scaled spanwise pressure spectra at $y/\delta_{\theta 0} = \pm 346$ for three different convective Mach numbers:—, TA12; ···, TA15; – · –, TA18. The spectra are scaled with (a) momentum thickness and (b) Taylor micro scale.

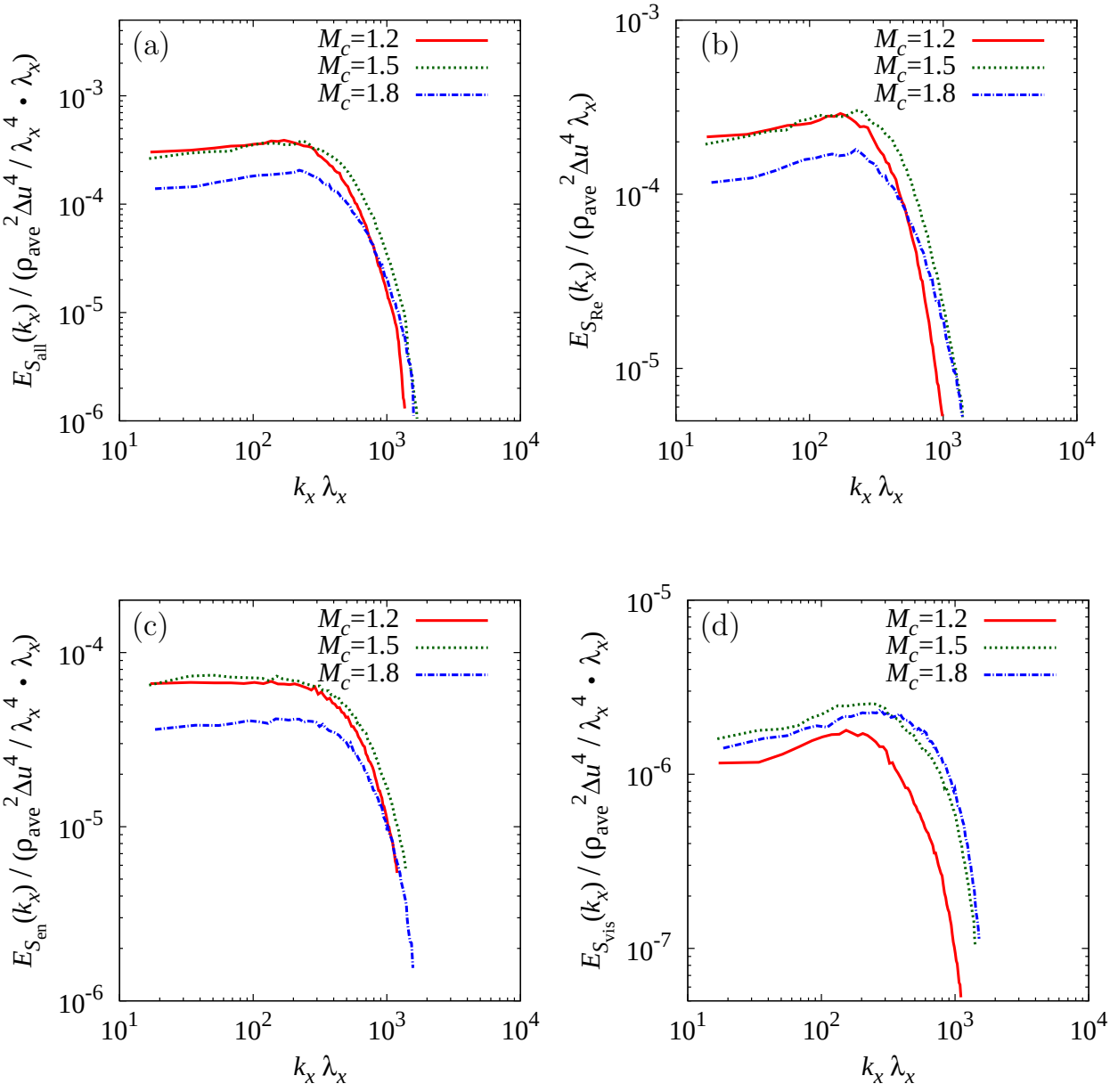

Figure 5.15: Scaled streamwise spectra of (a) term total, (b) Reynolds stress term, (c) entropy term and (d) viscous term at the center of the mixing layer for three different convective Mach numbers:—, TA12; ···, TA15; – · –, TA18. The spectra are scaled with the Taylor micro scale.

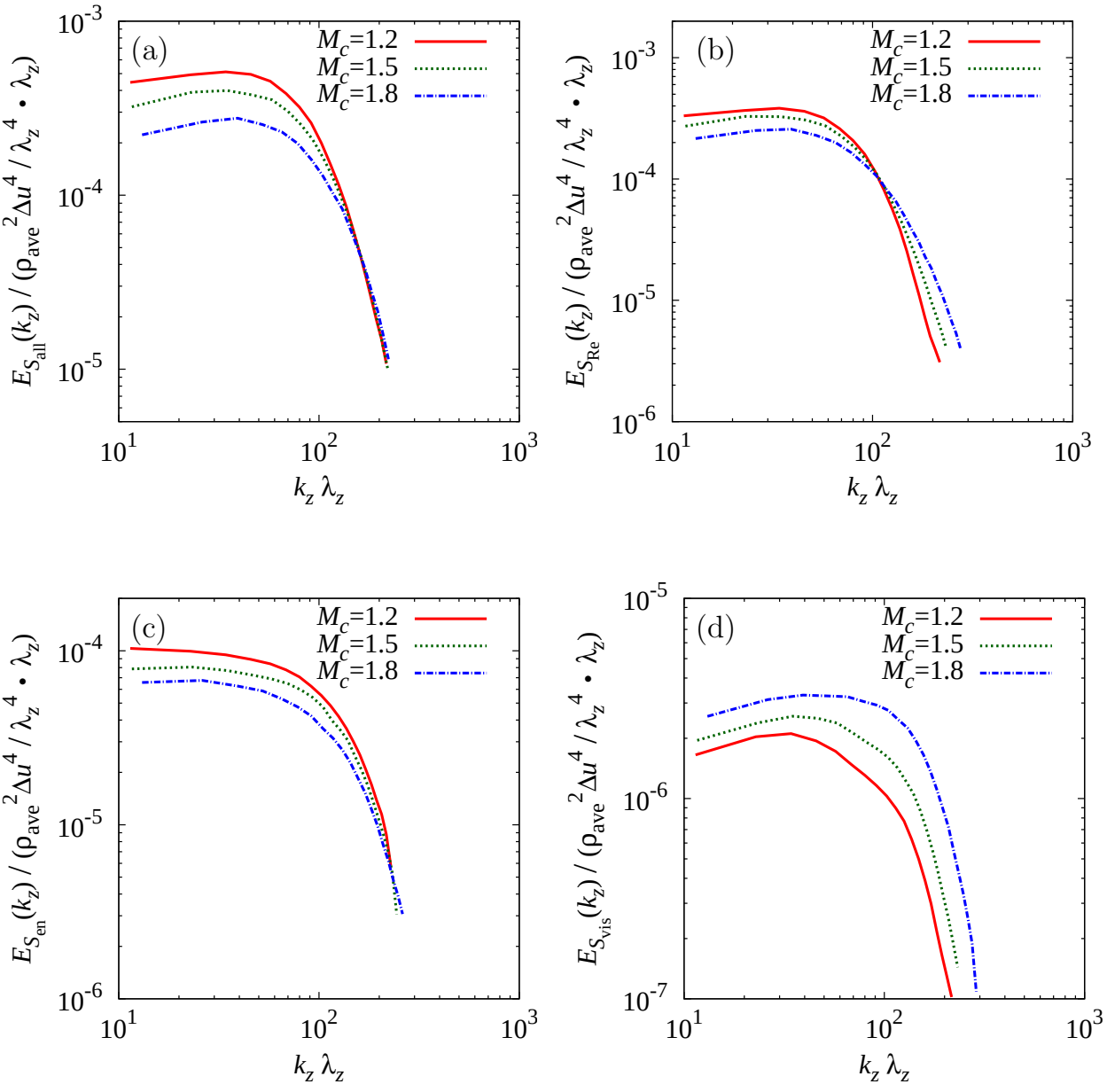

Figure 5.16: Scaled spanwise spectra of (a) term total, (b) Reynolds stress term, (c) entropy term and (d) viscous term at the center of the mixing layer for three different convective Mach numbers:—, TA12; ···, TA15; – · –, TA18. The spectra are scaled with the Taylor micro scale.

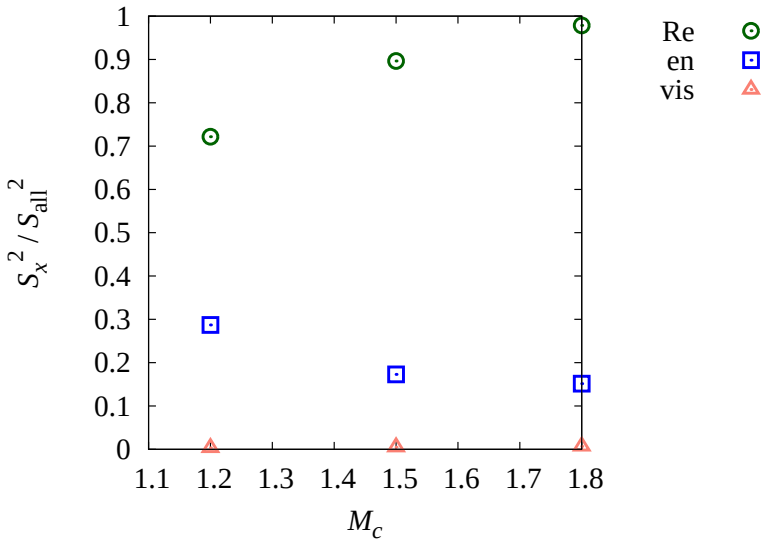

Figure 5.17: The ratio of each term to the overall sound source in the sound source strength for three different convective Mach numbers:◯, Reynolds stress term; □, entropy term; △, viscous term.

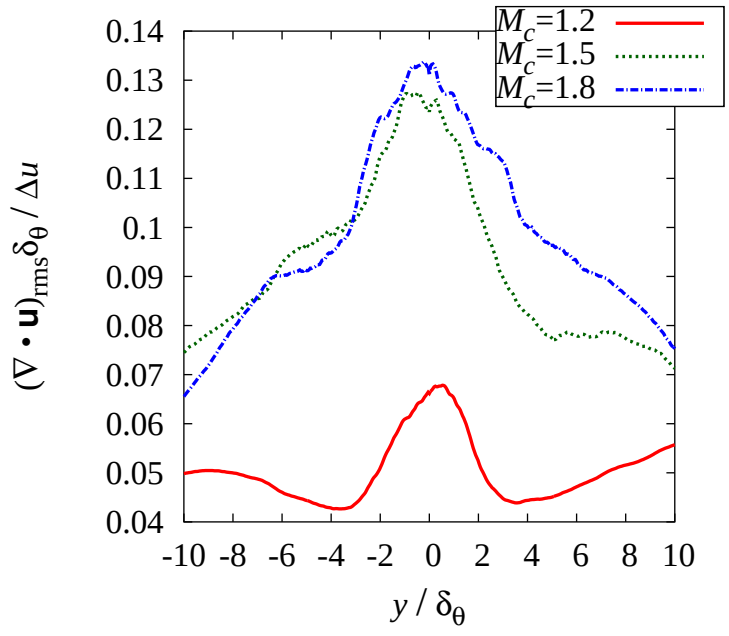

Figure 5.18: Averaged dilatation in the y direction for three different convective Mach numbers:—, $M_c = 1.2$; ···, $M_c = 1.5$; – · –, $M_c = 1.8$.

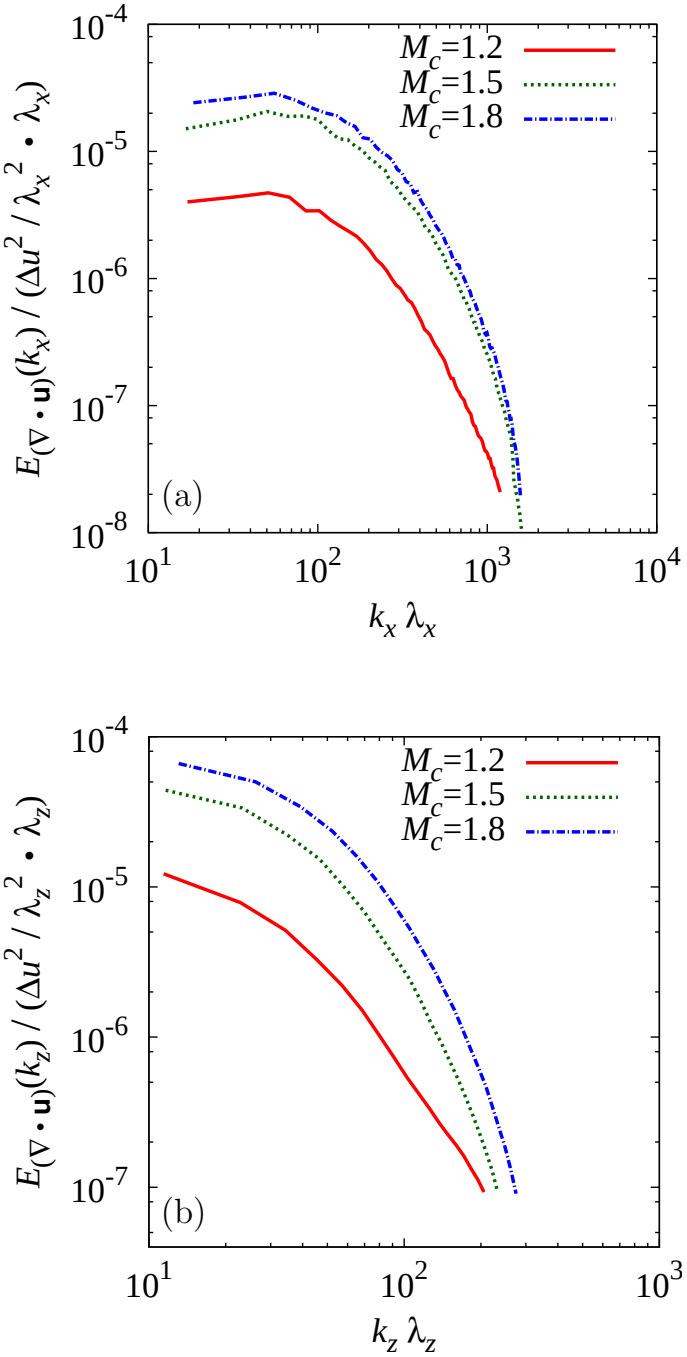

Figure 5.19: Scaled spectra of dilatation in (a) streamwise direction and (b) spanwise direction at the center of mixing layer for three different convective Mach numbers:—, TA12; ···, TA15; – · –, TA18. The spectra are scaled with the Taylor micro scale.

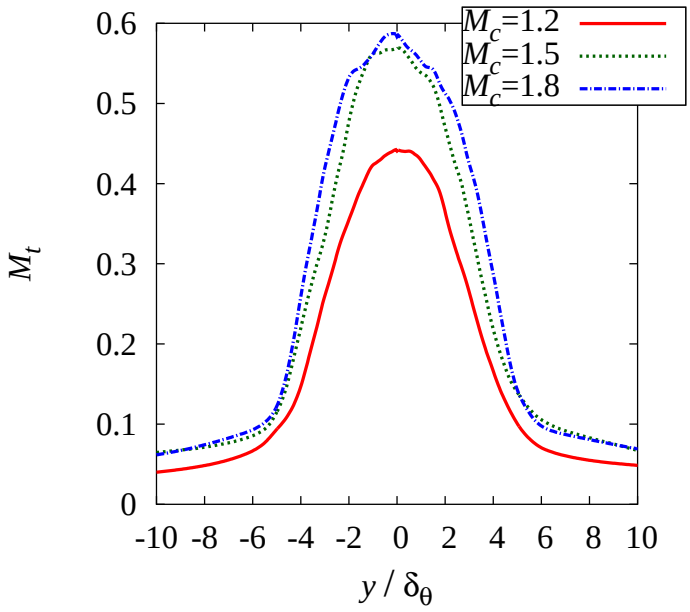

Figure 5.20: Averaged turbulent Mach number in the y direction for three different convective Mach numbers:—, $M_c = 1.2$; $\cdots$, $M_c = 1.5$; $-\cdot-$, $M_c = 1.8$..

The turbulent Mach number is one of the indicators for the occurrence of shocklets[48], so that the difference in the turbulent Mach number between cases is analyzed here. The turbulent Mach number in the compressible mixing layer is computed as follows:

$$M_t = \frac{\sqrt{u_i'' u_i''}}{< c >}. \tag{5.5}$$

Fig. 5.20 shows the averaged turbulent Mach number distributions for three different Mach number cases. In the previous chapter, the higher turbulent Mach number cases $M_{t0} = 0.8 - 1.0$ (corresponding to the steady state turbulent Mach number $M_{t\ \mathrm{steady}} = 0.42 - 0.48$ (Tab. 4.1)) showed that non-negligible effects of schoklets on sound sources. Especially, the highest turbulent Mach number case $M_{t0} = 1.0$ ($M_{t\ \mathrm{steady}} = 0.48$) showed the significant effects by shocklets. Cases $M_c \geq 1.5$ exceed the values in a wide range of flows, so that it is expected that the relatively large number of shocklets occur and affect the sound sources and the generated acoustic waves. The occurrence of shocklets could be possible also for $M_c = 1.2$ due to the maximum turbulent Mach number exceeds 0.42, but the regions of exceeding the threshold are very limited compared with the higher convective Mach number cases. Thus, even if shocklets could occur, the effects should be very limited.

It has been shown that shocklets in the higher convective Mach numbers seem to change the characteristics of far field pressure spectra. Here, the effects on the directivity

are investigated. The Mach angle can be calculated using the value of pressure gradient ∇p which corresponds to the normal direction of Mach waves (Fig. 5.21). The angle ϕ is computed in the following steps[20]. The unit vector of the shock normal direction $\mathbf{n}$ is computed as follows:

$$\mathbf{n} = \frac{\nabla p}{|\nabla p|}. \tag{5.6}$$

The angle ϕ between the y axis and the unit vector is calculated by;

$$\phi = \cos^{-1}(n_y), \tag{5.7}$$

where n_y is the component in the y direction of the unit vector $\mathbf{n}$. The angle is sampled conditionally using the following relation:

$$\frac{(\nabla \cdot \mathbf{u})\delta_\theta}{\Delta u} < d_c, \tag{5.8}$$

where d_c is set to be -0.0125 which is the same value as in the previous study[20]. Fig. 5.22 shows the averaged Mach angle distributions in the y direction for three different Mach numbers. The angle decreases with increasing the Mach number as expected. Also, the values are not saturated for the higher Mach numbers of $M_c \geq 1.5$. Note that the value should be saturated if the characteristics are governed by only the Mach waves. In addition, the same plots with standard deviation show that the deviation become larger with increasing the Mach number (Fig. 5.23). Note that the standard deviation is computed based on the spatially averaged values in which those are values for before ensemble averaging in time. Those suggest that the sound generation by shocklets would change the properties of directivity.

The other measure of the properties of the acoustic waves is the deviation from the assumed isentropic pressure fluctuation $p'_{s=0}$[20]:

$$p'_{s=0} = \frac{\gamma \rho' \bar{p}}{\bar{\rho}}. \tag{5.9}$$

Fig. 5.24 shows the deviation of pressure fluctuation from the isentropic pressure with three different convective Mach numbers. The trend is changed at between $M_c = 1.2$ and $M_c \geq 1.5$ (in which occurrence of relatively large amount of shocklets is expected), so that the results suggest that shocklets increase the non-linearity of the acoustic waves. Note, however, that the values are still small, and the non-linearity is not significant even in $M_c \geq 1.5$.

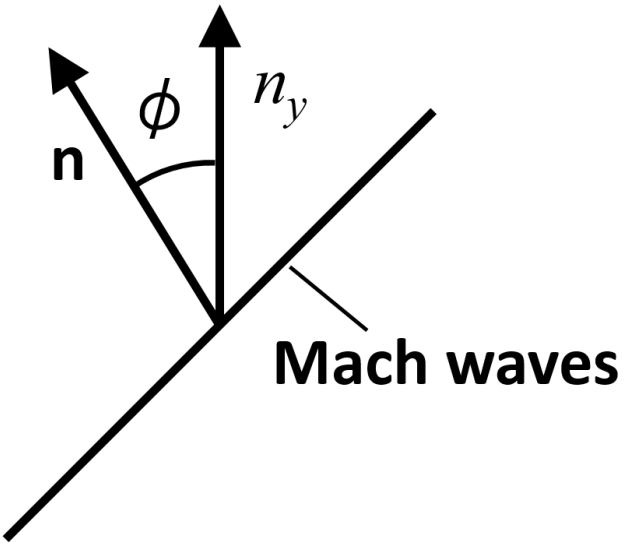

Figure 5.21: Schematic of computed Mach angle.

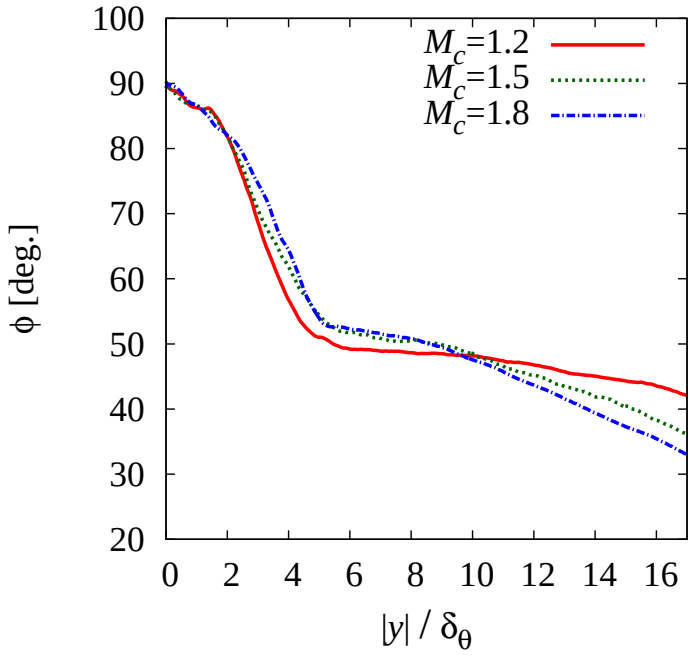

Figure 5.22: Averaged Mach angle in the y direction for three different convective Mach numbers:—, $M_c = 1.2$; $\cdots$, $M_c = 1.5$; $-\cdot-$, $M_c = 1.8$. The values are obtained by averaging the values of both upper and lower directions.

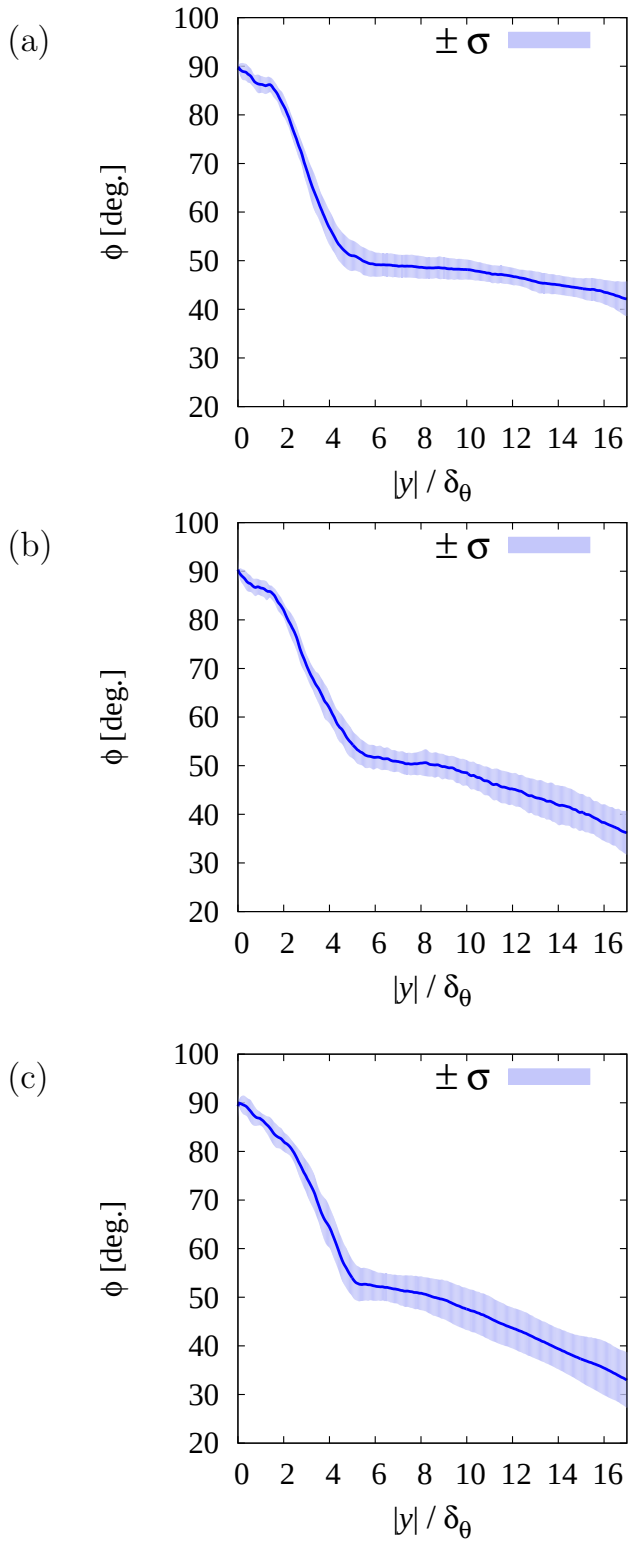

Figure 5.23: Averaged Mach angle with standard deviation (pale color) in the y direction for (a) $M_c = 1.2$, (b) $M_c = 1.5$ and (c) $M_c = 1.8$. The values are obtained by averaging the values of both upper and lower directions.

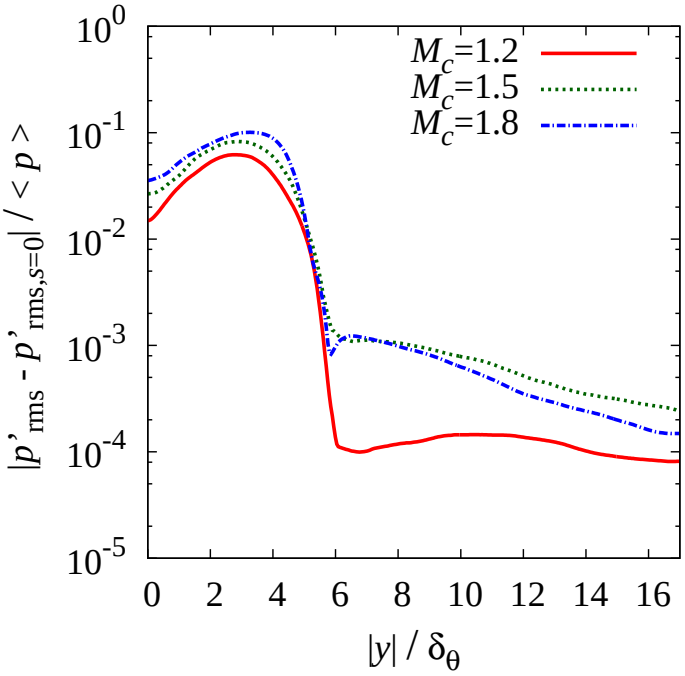

Figure 5.24: Deviation from the isentropic pressure fluctuation $p'_{s=0}$ in the y direction for three different convective Mach numbers:—, $M_c = 1.2$; $\cdots$, $M_c = 1.5$; $-\cdot-$, $M_c = 1.8$. Note that $< \cdot >$ denotes the averaged values at the plane. The values are obtained by averaging the values of both upper and lower directions.

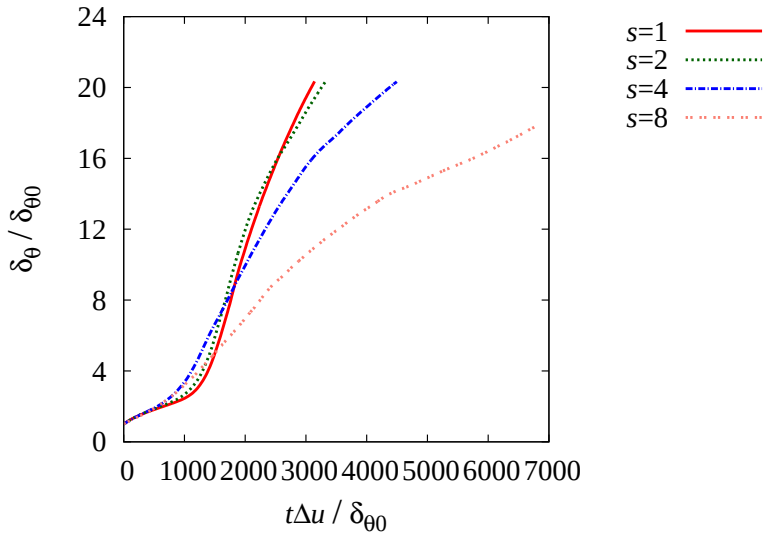

Figure 5.25: Time history of momentum thickness for the variable density mixing layer:—, TA15; ···, TB02; – · –, TB04; ·· ··, TB08.

5.3 Density ratio dependence on sound sources

In this subsection, density ratio dependence is investigated by fixing the convective Mach number to be 1.5. Four different density ratios $s = 1, 2, 4, 8$ are compared. Fig. 5.25 shows the time history of the momentum thickness for the variable density ratio cases. After the turbulent transition, the momentum thickness shows the linear, self-similar growth. The linear growth starts at $\delta_\theta/\delta_{\theta 0} = 14$ for $s = 1, 2, 8$ and at $\delta_\theta/\delta_{\theta 0} = 16$ for $s = 4$, so that the averaging for the most statistics are conducted after the times. Fig. 5.26 also confirms that the flows become fully turbulent state at $\delta_\theta/\delta_{\theta 0} = 16$. At the fully turbulent state, the properties of the flow structures and the acoustic waves between cases are significantly different. The turbulent structures become sparser with increasing the density ratio. Also, the turbulent structures at the lower density side (upper side) show larger structures than the other side for the higher density ratio cases. For the acoustic waves, the weaker fluctuation of dilatation is observed for both the upper and lower sides with increasing the density ratio. We focus on the acoustic wave characteristics at the higher density side in the following discussion due to the importance of the higher density side (corresponding to the outer side in hot jets). The discussion in this subsection proceeds in the same way as in the previous subsection for the convective Mach number dependence. The energy spectra are used for discussing the change in flow structures. After that the characteristics of sound sources and acoustic waves are analyzed.

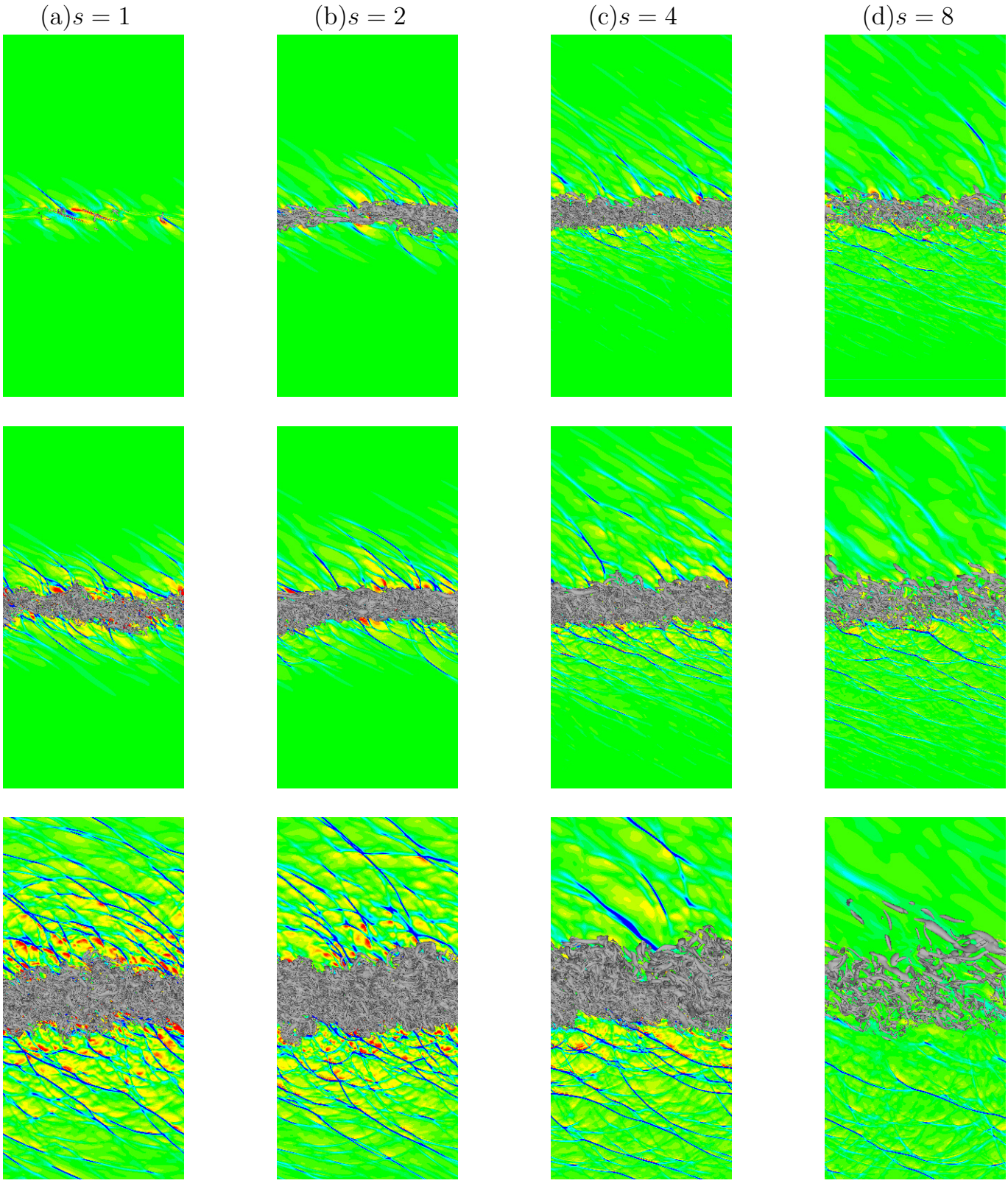

Figure 5.26: Normalized iso-surface of incompressible second invariant of the velocity gradient tensor $Q_{\text{inc}}/\Delta u^2 \times \delta_\theta^2 = 0.05$ and normalized dilatation $\nabla \cdot \mathbf{u}/\Delta u \times \delta_\theta$ at $z = z_{\max}$ for (a) TA15, (b) TB02, (c) TB04 and (d) TB08. The contour range of dilatation is from -0.1 to 0.1. The corresponding times from top to bottom are $\delta_\theta/\delta_{\theta 0} = 6$, $\delta_\theta/\delta_{\theta 0} = 8$ and $\delta_\theta/\delta_{\theta 0} = 16$, respectively.

5.3.1 Energy spectra

In the previous subsection, the energy spectra of different convective Mach numbers were scaled well with the Taylor micro scale. We also apply the Taylor micro scaling to the energy spectra in this subsection. The streamwise energy spectra scaled with the momentum thickness and the Taylor micro scale are shown in Figs.5.27 (a) and 5.27 (b), respectively. The energy spectra also collapse well with the Taylor micro scale. Note, however, that only the highest density ratio case $s = 8$ decays a little faster even after the Taylor micro scaling. This is due to the limited range of the inertial range for the case and implies that the flows behave as more like lower Reynolds number than the remaining cases. The trend is the same also for the spanwise spectra (Fig. 5.28). In addition, the different scales of structure are observed between the upper and lower sides for the variable density ratio cases (Fig. 5.26) and the trend is observed most clearly in case $s = 8$. Thus, the characteristics of the energy spectra at the different positions are investigated using case $s = 8$. Two planes are selected as the representative planes. One is $y/\delta_\theta = -1$ and the other is $y/\delta_\theta = 3$ where $y/\delta_\theta = 3$ is near the center of the mixing layer. Those planes are visualized in Fig. 5.29. We show the averaged streamwise energy spectra at two different planes scaled with the momentum thickness and the Taylor micro scale in Fig. 5.30. Although the spectra collapse better with the Taylor micro scale than the momentum thickness, the deviation still exists at the lower wave numbers. The same trend is observed in the spanwise spectra (Fig. 5.31). To understand the characteristics further, an additional scaling is conducted for the spectra using the Kolmogorov length scale $\eta = (\nu^3/\varepsilon)^{1/4}$, the energy dissipation ε, and the kinematic viscosity ν. Note that the dissipation in the temporally evolving compressible mixing layer is defined by;

$$\varepsilon = \frac{1}{\bar{\rho}}\Big(\overline{\tau'_{jk}\frac{\partial u''_i}{\partial x_k} + \tau'_{ik}\frac{\partial u''_j}{\partial x_k}}\Big), \tag{5.10}$$

where

$$\tau'_{ij} = \mu\Big(\frac{\partial u'_i}{\partial x_j} + \frac{\partial u'_j}{\partial x_i} - \delta_{ij}\frac{2}{3}\mu\frac{\partial u'_k}{\partial x_k}\Big). \tag{5.11}$$

Here, $()'$, $()''$ and $\bar{()}$ denote the Reynolds fluctuation, the Favre fluctuation and the Reynolds average. It is well known that the scaling with those quantities collapse lines of energy spectra between the different Reynolds number turbulent flows. The spectra with those quantities in both streamwise and spanwise directions are shown in Fig. 5.32. The spectra collapse well and the spectra at $y/\delta_\theta = 3$ shifts to the higher wave number

side. These results show that the change in flow structures is caused by the different Reynolds number. Note that the scaled spectra with the momentum thickness decay faster at $y/\delta_\theta = 3$ than at $y/\delta_\theta = -1$ indicate that the flows at $y/\delta_\theta = 3$ behaves more like the lower Reynolds number flow than those at $y/\delta_\theta = -1$. Also, the results indicate that the flows even at the lower Reynolds number side $y/\delta_\theta = 3$ still keep the properties of turbulence. The change of the Reynolds number should be affected by the temperature difference (and so viscosity) across the mixing layer. Fig. 5.33 shows the averaged viscosity for the four different density ratio cases. The values are scaled with the average viscosity between two streams $\mu_{\text{ave}} = (\mu_1 + \mu_2)/2$. The highest density ratio case shows around four times difference in the viscosity between two streams. Thus, the Reynolds number at the lower density side is four times smaller than that at the higher density side. The difference in the Reynolds number across the mixing layer leads to the different scales of flow structure between lower and higher density sides.

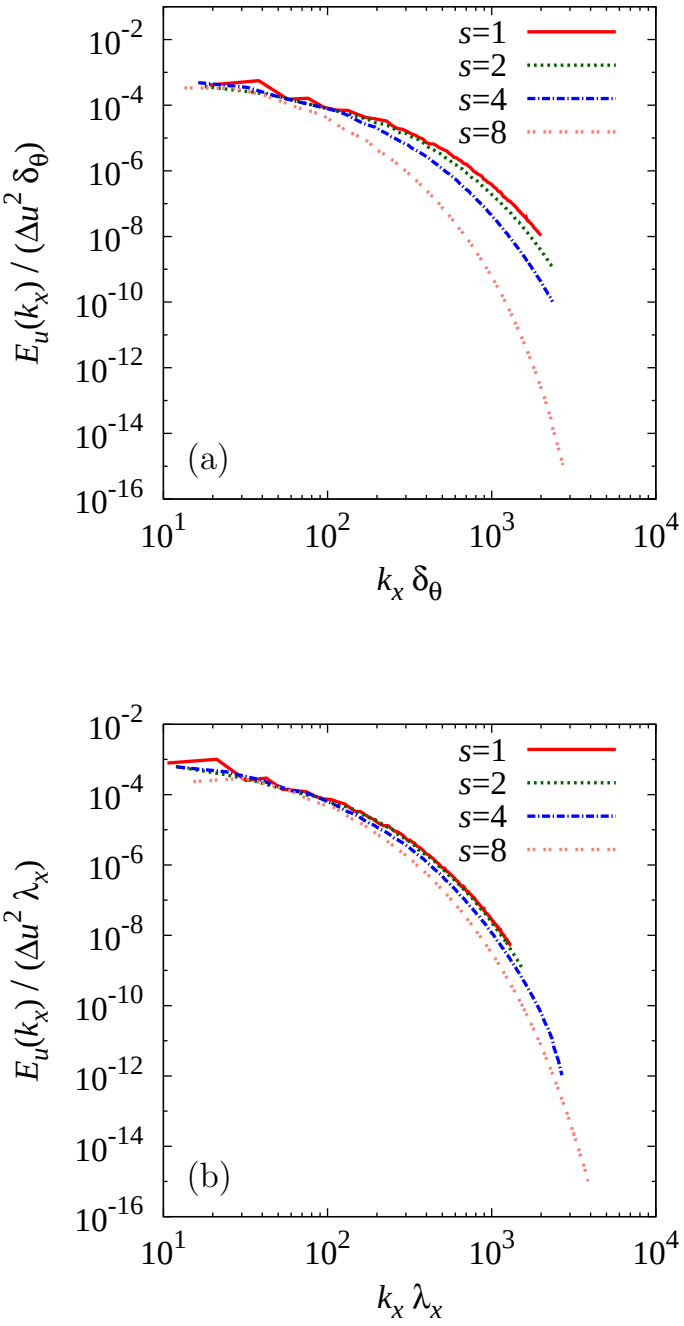

Figure 5.27: Scaled streamwise energy spectra at the center of mixing layer:—, TA15; ···, TB02; – · –, TB04; ·· ··, TB08. The spectra are scaled with (a) momentum thickness and (b) Taylor micro scale

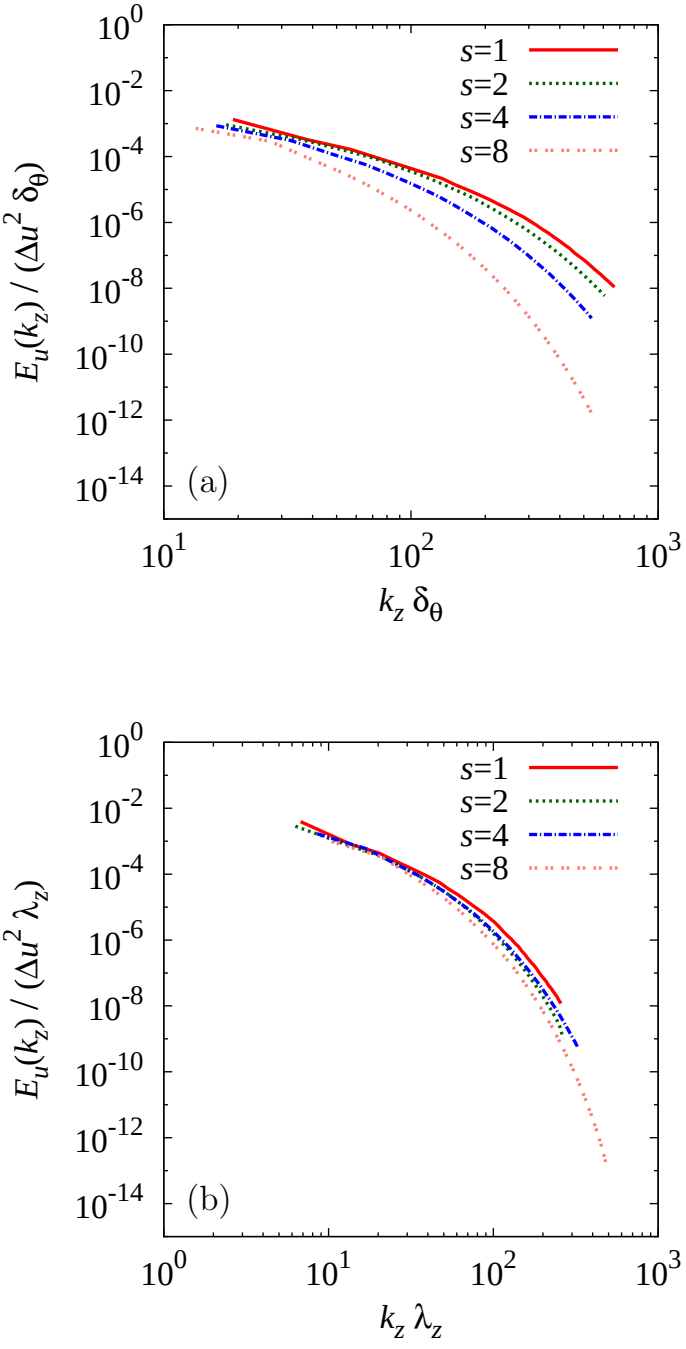

Figure 5.28: Scaled spanwise energy spectra at the center of mixing layer:—, TA15; ···, TB02; – · –, TB04; ·· ··, TB08. The spectra are scaled with (a) momentum thickness and (b) Taylor micro scale.

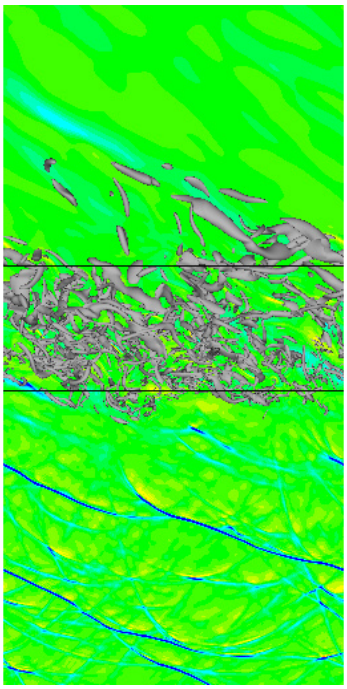

Figure 5.29: The computed planes for comparing the energy spectra at the different positions. The upper plane is $y/\delta_\theta = 3$, and the lower plane is $y/\delta_\theta = -1$.

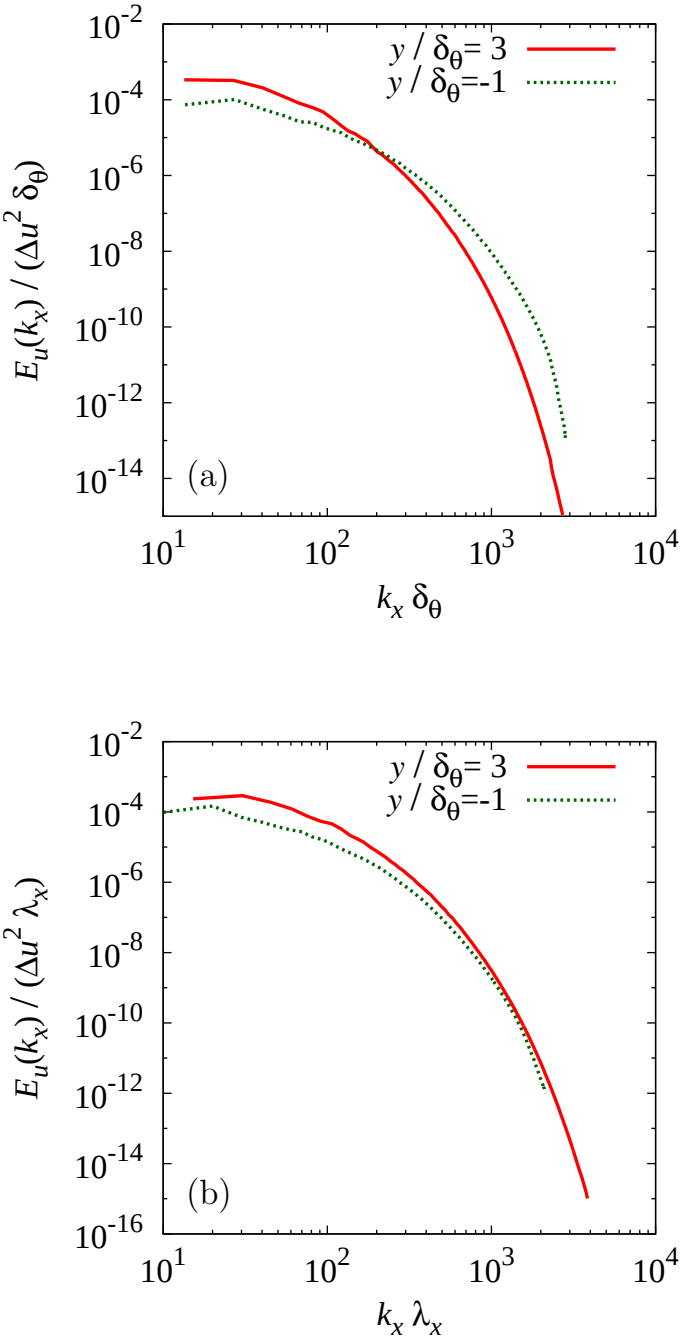

Figure 5.30: Scaled streamwise energy spectra for $s = 8$ at :—, $y/\delta_\theta = -1$; ···, $y/\delta_\theta = 3$. The values are scaled with (a) momentum thickness and (b) Taylor micro scale.

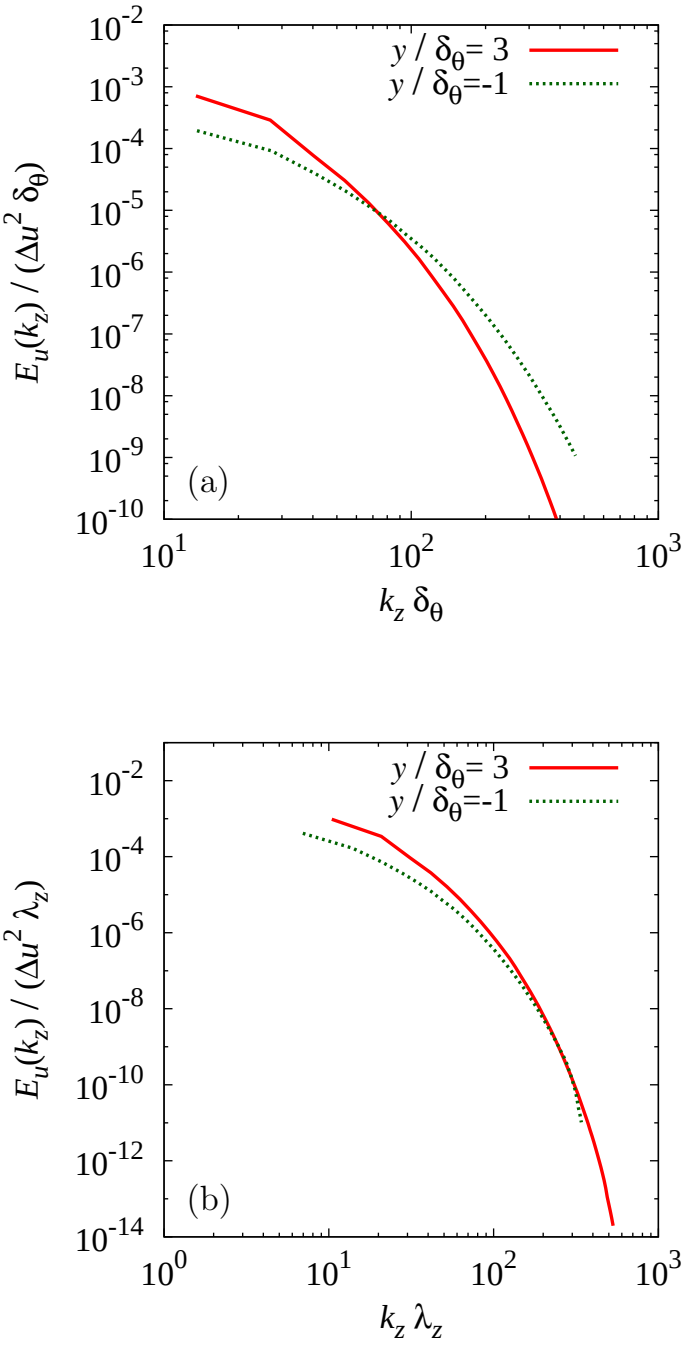

Figure 5.31: Scaled spanwise energy spectra for $s = 8$ at :—, $y/\delta_\theta = -1$; ···, $y/\delta_\theta = 3$. The values are scaled with (a) momentum thickness and (b) Taylor micro scale.

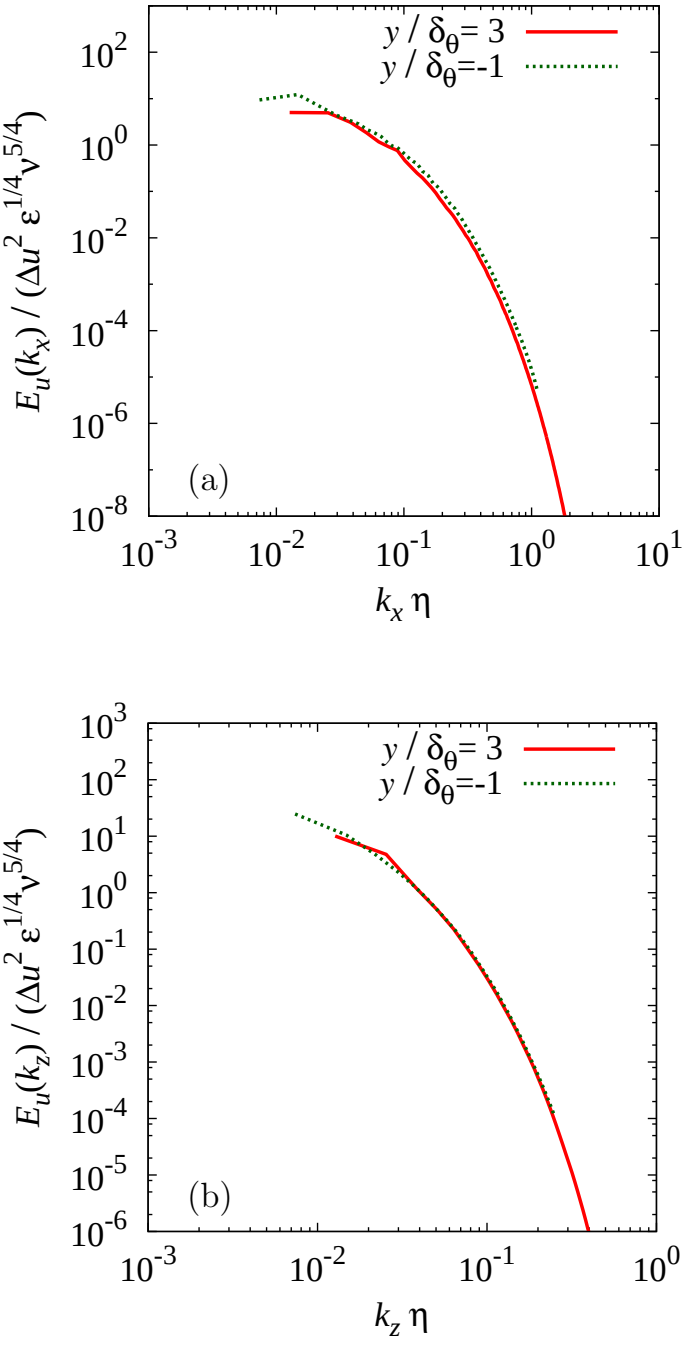

Figure 5.32: Scaled energy spectra in (a) streamwise direction and (b) spanwise direction for $s = 8$ at :—, $y/\delta_\theta = -1$; ···, $y/\delta_\theta = 3$. The values are scaled with Kolmogorov length scale η, energy dissipation ε, and kinematic viscosity ν.

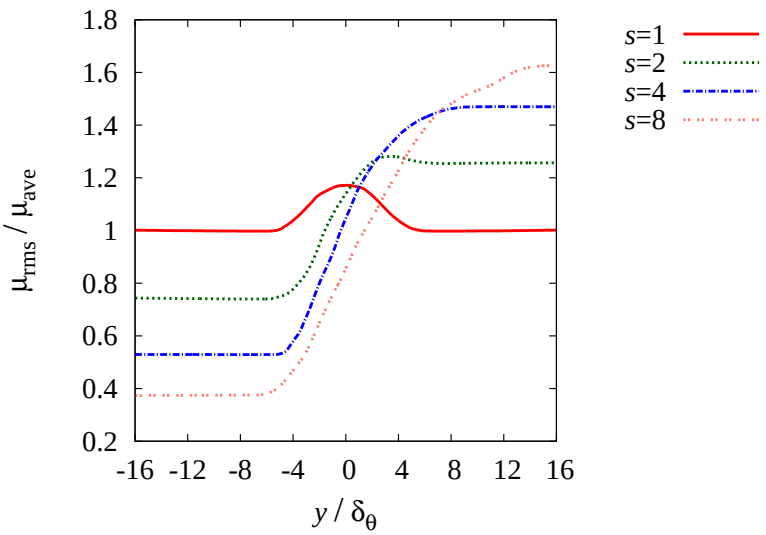

Figure 5.33: Averaged viscosity in the y direction for four different density ratios:—, TA15; · · ·, TB02; – · –, TB04; ·· ··, TB08. Note that the values are normalized by the averaged values of upper and lower streams.

5.3.2 Acoustic waves and sound sources

It has been shown that the flow structures are changed significantly for the variable density ratio cases. In this subsection, how those change in flows affect the characteristics of sound sources and acoustic waves are analyzed. Note, again that our focus is on the higher density side due to the importance for the application of hot jets, so that the discussion is conducted for that side hereafter. (See App. B for lower density side.) The Lighthill equation in the variable density ratio cases needs careful treatment of the constant values of density and the speed of sound, because the entropy term is highly affected by the selection of the constant values. Our focus is the higher density side, so that the constant values at the higher density side should be used. Note that, for the normalization, density at the higher density side is used for the same reason above. Then, we introduce the source terms of the Lighthill equation for the higher density side as follows:

$$\begin{aligned} S_{\mathrm{Re}} &= \frac{\partial \rho u_i u_j}{\partial x_i \partial x_j}, \\ S_{\mathrm{en}} &= \frac{\partial (\delta_{ij}[p - p_{\mathrm{ave}} - c_2^2(\rho - \rho_2)])}{\partial x_i \partial x_j}, \\ S_{\mathrm{vis}} &= \frac{\partial \left(\mu \left(\frac{\partial u_i}{\partial x_j} \frac{\partial u_j}{\partial x_i} - \frac{2}{3} \delta_{ij} \frac{\partial u_k}{\partial x_k} \right) \right)}{\partial x_i \partial x_j}, \\ S_{\mathrm{all}} &= S_{\mathrm{Re}} + S_{\mathrm{en}} + S_{\mathrm{vis}}, \end{aligned} \tag{5.12}$$

where $()_2$ denotes the values of the higher density side. Before the discussion of the sound source characteristics, we discuss the averaged rms values of the pressure fluctuations (Fig. 5.34). Note again that the values are for the higher density side. The acoustic waves at the far field become weaker with increasing the density ratio. The trend is the same as that of overall sound sources (Fig. 5.35). In addition, the mean density difference also affects the source positions. The source positions move to the higher density side. On the other hand, the maximum positions of vortices move to the different side with increasing the density ratio (Fig. 5.36) as is reported in the previous study[6]. Thus, the other phenomena than vortices should affect the source position in the variable density ratio cases. To understand the reasons, the averaged density distributions are shown in Fig. 5.37. The maximum source positions correspond to the positions where the mean density is reaching to the values of the higher density side. This is due to the form of the source terms of the Lighthill equation. Both the Reynolds stress term and the entropy term have the contributions of density (Eq. 5.12), so that the source

terms are affected significantly by the mean density profile. Thus, the higher density increases the level of source terms of the Reynolds stress term and the entropy term, and then, the values of sound sources at the higher density side become larger. The discussion above is supported by the similar maximum positions of the overall sound source (Fig. 5.35), the Reynolds stress term (Fig. 5.38 (a)) and the entropy term (Fig. 5.38 (b)). To summarize, the values of sound sources are highly affected by the mean density profile due to the existence of the density contribution in the source terms, so that the maximum source positions move to the higher density side. Next, we discuss the term to term relationship. Bodony and Lele [29] suggested that the canceling out of the Reynolds stress term and the entropy term would be a cause of weaker acoustic waves in heated jets. We check whether the canceling out exists or not in the present computation in the following analysis. To analyze it, the ratio of sound source strength of each term to the overall sound source is discussed. Those sound source strength are obtained by the integral of the profiles of Figs. 5.35 (for overall sound source) and 5.38 (for the Reynolds stress term and the entropy term). Note that the strength of the viscous term is obtained in the similar way. The ratio of each term to the overall sound source strength is shown in Fig. 5.39. The results show that the contributions of the Reynolds stress term exceeds unity for $s > 1$, so that it leads to the canceling out of the Reynolds stress term and the entropy term. This is because the entropy term shows non-negligible value, whereas the viscous term is negligible. The canceling out can be explained by the simple discussion of the mean profiles of the Reynolds stress contribution ($\rho u_i u_j$) and the entropy contribution ($p - p_{\mathrm{ave}} - c_2^2(\rho - \rho_2)$) of the Lighthill's turbulent stress tensor. Those profiles are also highly affected by the mean profile of density. As the effects of mean pressure is small compared with density, the effect of pressure can be neglected. Thus, we focus only on the mean profile of density for the discussion of the entropy contribution of the Lighthill's turbulent stress tensor. The averaged distribution of $\rho u_i u_j$ in the y direction is shown in Fig. 5.40. The distributions for the higher density ratio cases are very similar with that of averaged density (related to the entropy contribution) in Fig. 5.37. The fact that $\rho u_i u_j$ and ρ take similar profiles for the higher density side leads to the canceling out of the Reynolds stress term and the entropy term. This is because the Reynolds stress contribution ($\rho u_i u_j$) and the density contribution of the entropy term ($-c_2^2(\rho - \rho_2) \propto -\rho$) show opposite signs (Eq. 5.12). Note again that the effects of pressure contribution is ignored. Then, we explain the reason why $\rho u_i u_j$ and ρ show similar profiles. The mean distributions are determined by almost one-dimensionally, because the free stream goes to one direction (x direction). Thus, we consider only the component of ρu_1^2 for the discussion. u_1^2 shows the similar

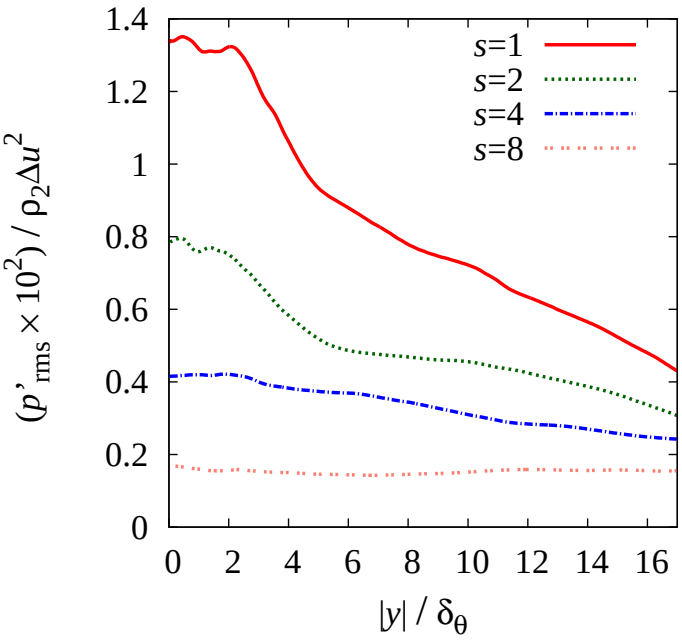

Figure 5.34: Averaged rms values of pressure fluctuation in the y direction for four different density ratios:—, TA15; ···, TB02; – · –, TB04; ·· ··, TB08.

profile of the case $s = 1$ in Fig. 5.40 (The parabola like profile which has the peak at the center of the mixing layer). The profile of u_1^2 for the higher density side shows the similar profile of density ρ, so that ρu_1^2 also shows the similar profile of density. On the other hand, as the density is lower for the lower density side, the multiplication of u_1^2 and ρ leads to the smaller values compared with the higher density side. Therefore, the shape of the profile of ρu_1^2 is approaching to that of density ρ for larger density ratio cases. That is the simple reason that $\rho u_i u_j$ and ρ have similar profiles and lead to the canceling out of the Reynolds stress term and the entropy term for the variable density ratio cases.

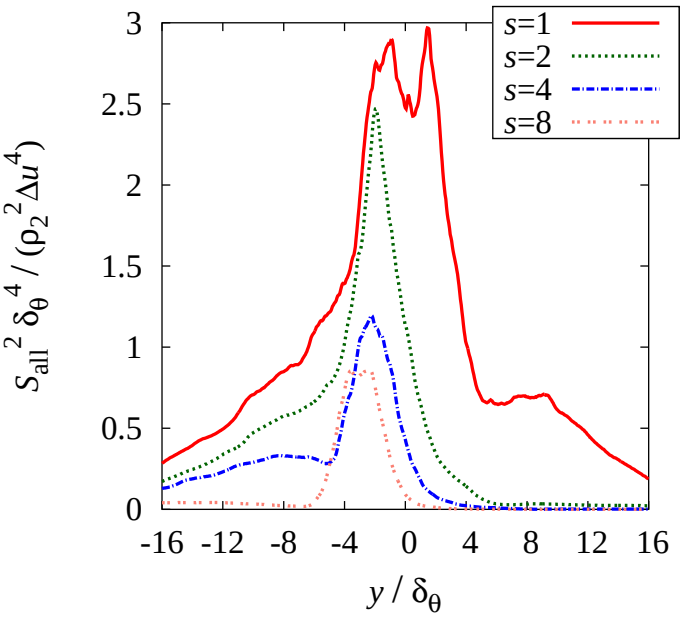

Figure 5.35: Averaged overall sound sources in the y direction for four different density ratio cases:—, TA15; ···, TB02; – · –, TB04; ·· ··, TB08.

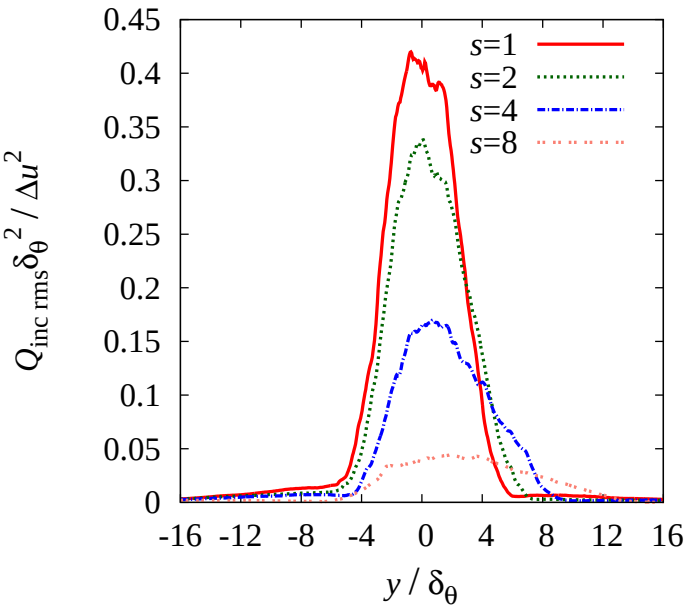

Figure 5.36: Averaged incompressible second invariant of the velocity gradient tensor in the y direction for four different density ratios:—, TA15; ···, TB02; – · –, TB04; ·· ··, TB08.

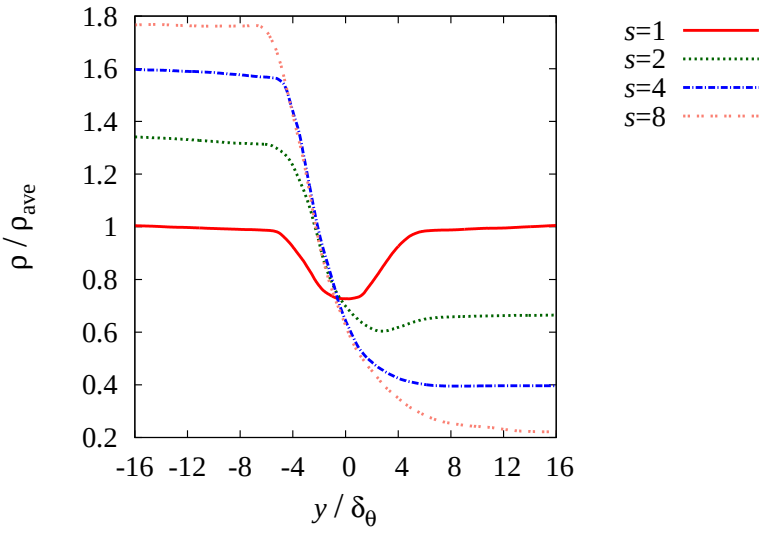

Figure 5.37: Averaged density distributions in the y direction for four different density ratios:—, TA15; $\cdots$, TB02; $-\cdot-$, TB04; $\cdot\cdot\,\cdot\cdot$, TB08.

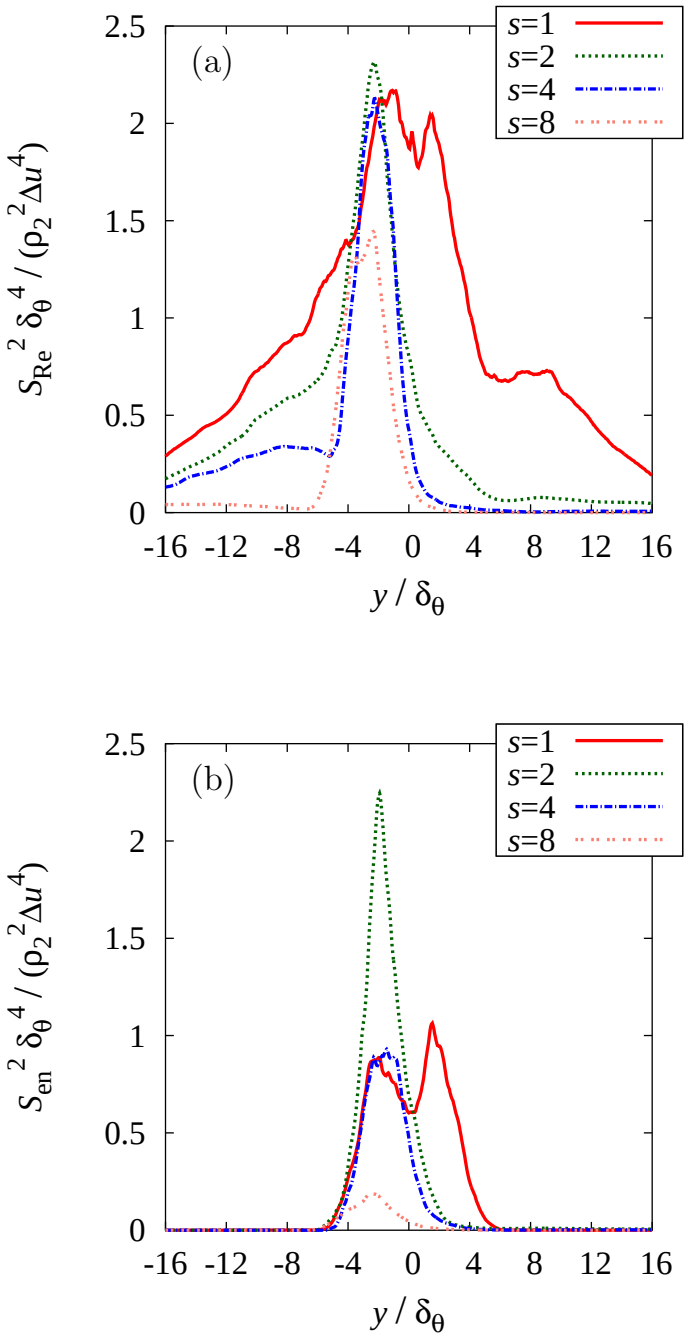

Figure 5.38: Averaged source terms of (a) Reynolds stress term and (b) entropy term in the y direction for four different density ratios:—, TA15; ···, TB02; – · –, TB04; ·· ··, TB08.

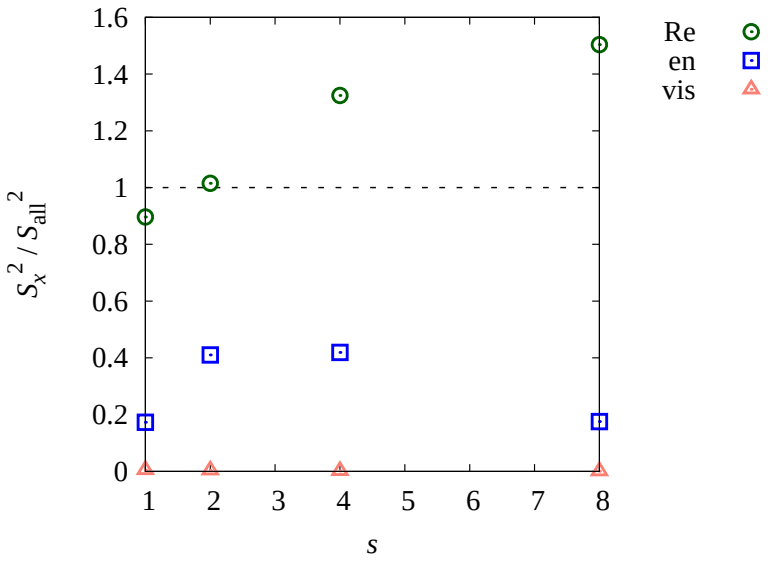

Figure 5.39: The ratio of each term to the overall sound source in the sound source strength for four different density ratios:◯, Reynolds stress term; □, entropy term; △, viscous term.

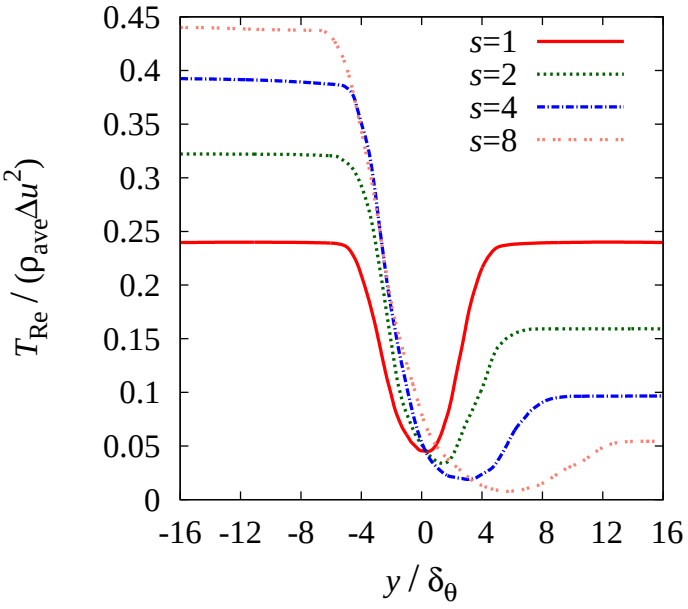

Figure 5.40: Averaged distributions of Reynolds stress component of the Lighthill's turbulent stress tensor $\rho u_i u_j$ in the y direction for four different density ratios:—, TA15; ···, TB02; – · –, TB04; ·· ··, TB08.

Then, we move on the characteristics of the acoustic waves. The scaling of the far field pressure spectra are also investigated in this subsection. Again, the values of spectra are obtained by averaging the acoustic waves generated after $\delta_\theta/\delta_{\theta 0} = 10$ by considering the retarded time. Note that the time $\delta_\theta/\delta_{\theta 0} = 10$ is selected, because all cases have passed the clear transition at that time. Fig. 5.41 shows the pressure spectra scaled with the momentum thickness and the Taylor micro scale. Note that the Taylor micro scale is computed at the maximum sound source position. The spectra do not collapse well with the Taylor micro scale except for the higher wave numbers the trend of which is different from that of the convective Mach number dependence. The trend is the same also for the spanwise spectra (Fig. 5.42). The difference in the far field pressure spectra between the variable density ratio cases and the isothermal cases would be due to the different sound source characteristics of them. In the isothermal cases, the sound source is basically determined by the turbulent motion (including shocklets). On the other hand, in the variable density ratio cases, the mean density profile largely affects the sound source characteristics.

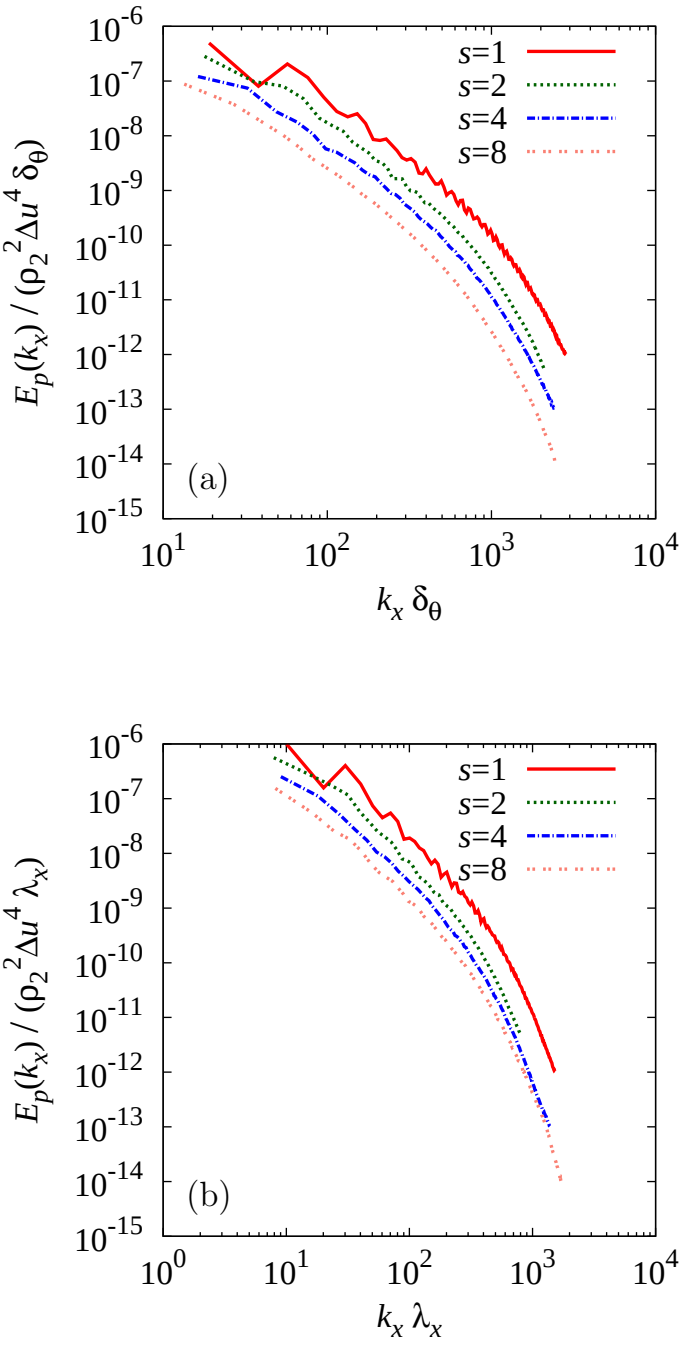

Figure 5.41: Scaled streamwise pressure spectra at $y/\delta_{\theta 0} = \pm 346$:—, TA15; ···, TB02; – · –, TB04; ·· ··, TB08. The spectra are scaled with (a) momentum thickness and (b) Taylor micro scale. Taylor micro scale is computed at the maximum source strength position.

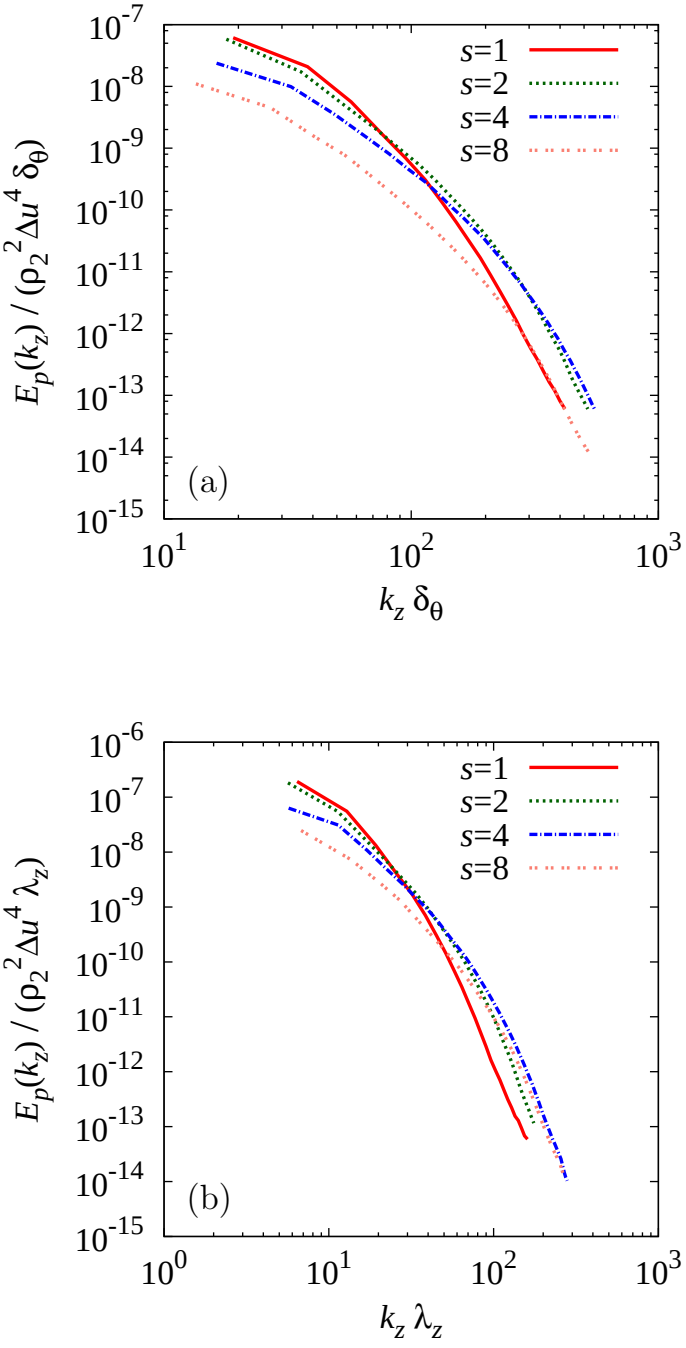

Figure 5.42: Scaled spanwise pressure spectra at $y/\delta_{\theta 0} = \pm 346$:—, TA15; ···, TB02; – · –, TB04; ·· ··, TB08. The spectra are scaled with (a) momentum thickness and (b) Taylor micro scale. Taylor micro scale is computed at the maximum source strength position.

Finally, other properties of the acoustic waves are analyzed. The density ratio dependence on the Mach angle (computed by Eq. 5.7) is shown in Fig. 5.43. For $s = 1, 2$, the wave angle is saturated to the similar values, but, the higher density ratios $s = 4, 8$ show different development. In the development process, the angle shows local minimum at the near field for the higher density ratios ($s = 4, 8$). Also, the Mach angle with standard deviation in Figs. 5.44 ($s = 1, 2$) and 5.45 ($s = 4, 8$). The results show that the deviation become larger with increasing the density ratio. Thus, the randomness of the acoustic waves increases with increasing the density ratio. The results would suggest that the existence of various modes of instability wave moving with different convective Mach number for the higher density ratio cases. Because of the temperature difference over the mixing layer, the speed of sound is also changed across the mixing layer. Thus, the explanation of the existence of the various modes moving with different convective Mach number could be possible. The other probability is that the existence of many different scales in flows due to the different Reynolds number over the mixing layer for the variable density ratio cases as discussed in Sec. 5.3.1. Those scales of turbulence could generate the different acoustic waves. Note, however, that the effect is expected to be smaller in sufficiently high Reynolds number flows, because the Reynolds number difference between upper and lower streams become relatively smaller (based on the Reynolds number of the mixing layer) compared with the lower Reynolds number flows.

Fig. 5.46 shows the deviation of the pressure fluctuations from the isentropic pressure (Eq. 5.9). There are not much difference between cases and the values are still small. Thus, the larger density ratio does not increase the non-linearity significantly at least in the present computational range of the density ratio and the convective Mach number, though the sound source characteristics have some difference between cases as discussed above.

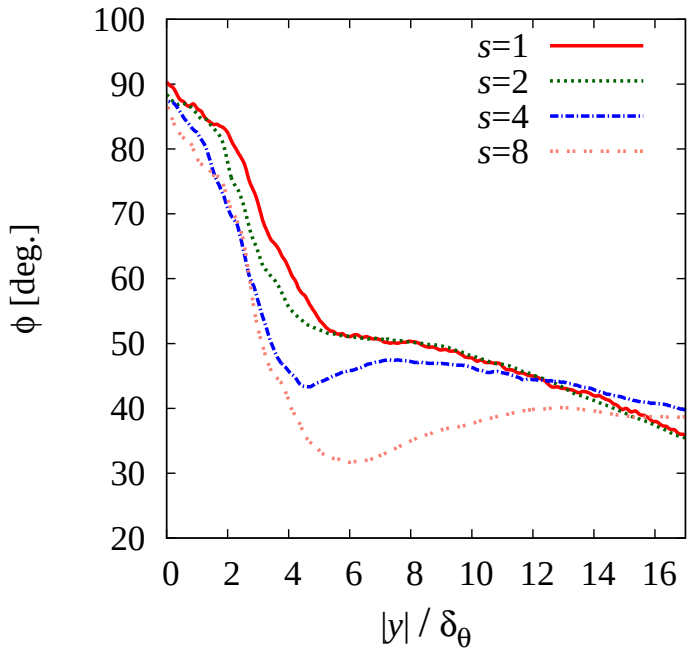

Figure 5.43: Averaged Mach angle in the y direction for four different density ratios:—, TA15; ···, TB02; – · –, TB04; ·· ··, TB08.

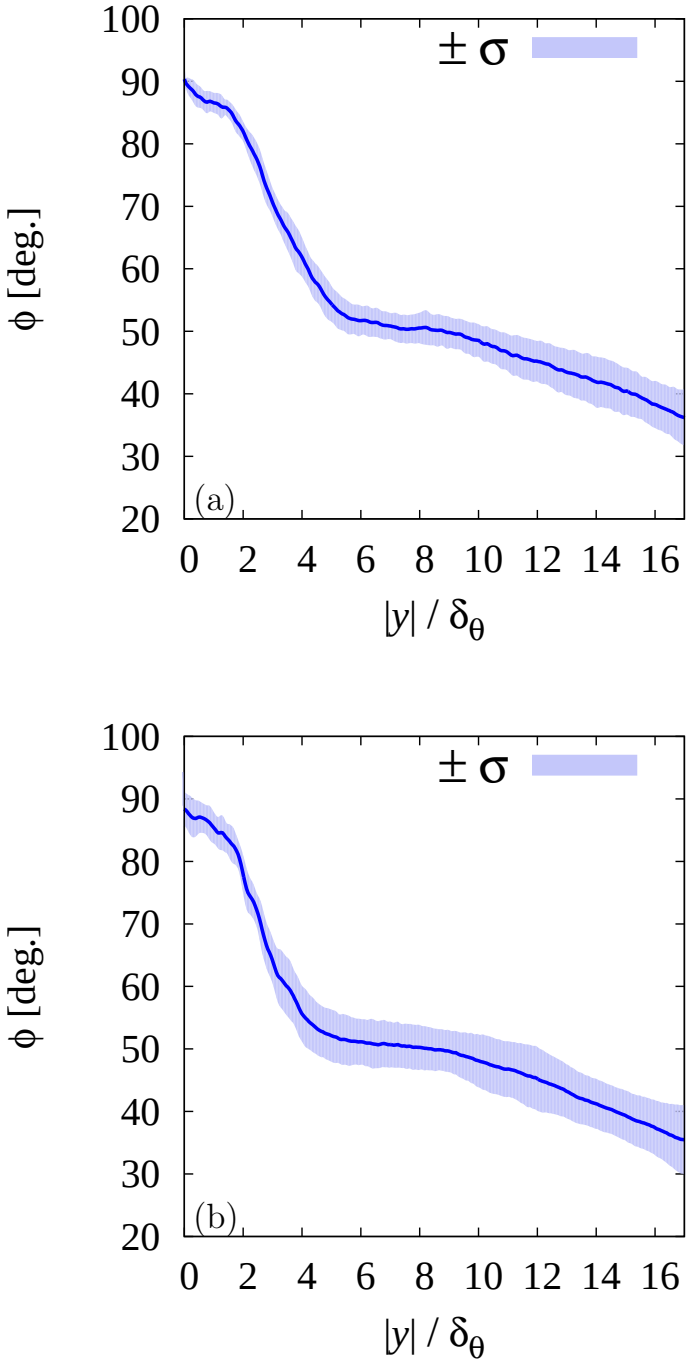

Figure 5.44: Averaged Mach angle with standard deviation (pale color) in the y direction for (a) TA15 ($s = 1$), (b) TB02 ($s = 2$).

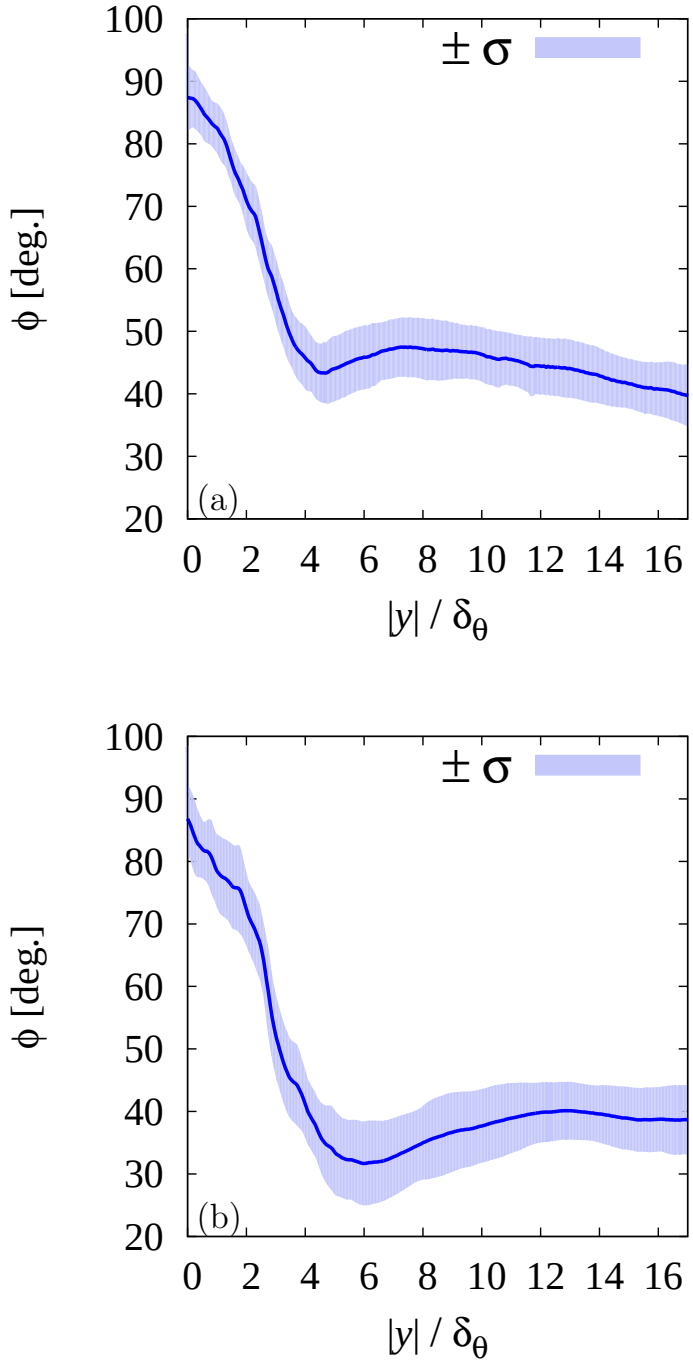

Figure 5.45: Averaged Mach angle with standard deviation (pale color) in the y direction for (a) TB04 ($s = 4$), (b) TB08 ($s = 8$).

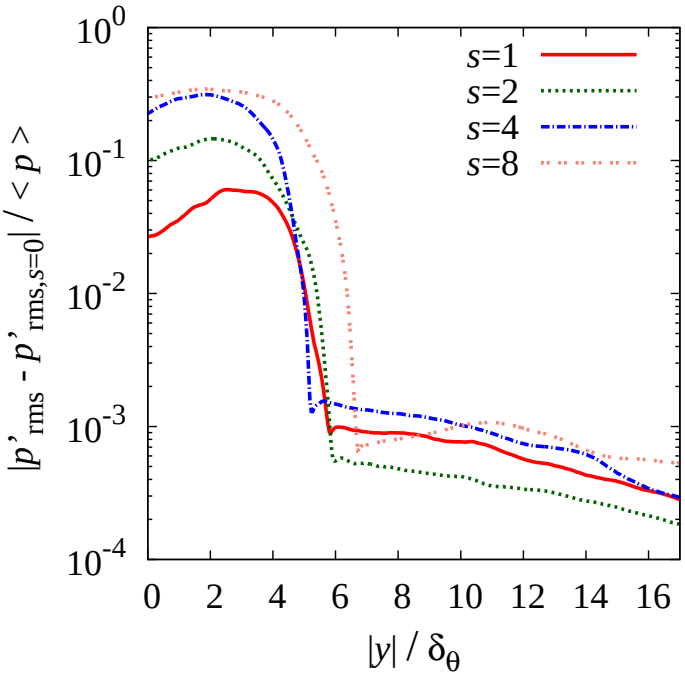

Figure 5.46: Deviation from the isentropic pressure fluctuation $p'_{s=0}$ in the y direction for four different density ratios:—, TA15; $\cdots$, TB02; $-\cdot-$, TB04; $\cdot\cdot\,\cdot\cdot$, TB08. Note that $< \cdot >$ denotes the averaged values at the plane.

5.4 Summary of this chapter

In this chapter, the convective Mach number and the density (temperature) ratio dependence on the sound source and acoustic wave characteristics were analyzed by the direct numerical simulation of the temporally evolving compressible mixing layer.

For the convective Mach number dependence, the strength of the acoustic waves are weakened with increasing the Mach number. This is due to the suppression of the vortices (as important sound sources) by the compressibility. In addition, the far field pressure spectra are scaled well with the Taylor micro scale except for the higher and lower wave numbers. Note that the energy spectra are scaled very well with the Taylor micro scale at the entire wave number range. The results showed that the difference at the higher wave numbers of the scaled far field pressure spectra is due to the appearance of shocklets in flow fields for the higher convective Mach numbers $M_c \geq 1.5$. Those cases show the higher turbulent Mach number compared with the case $M_c = 1.2$. The existence of shocklets in flow fields would affect the acoustic wave characteristics. The non-linearity of the acoustic waves increases for the higher convective Mach numbers (but the degree of the non-linearity is still small). In addition, shocklets would affect the Mach angle, and lead to the more fluctuated characteristics for the Mach angle with increasing the convective Mach number.

For the density (temperature) ratio dependence, the acoustic waves are weakened with increasing the density ratio. There are two possible reasons. One is that the strength of vortices are weakened with increasing the density ratio. The other is the canceling out of the Reynolds stress term and the entropy term for the variable density ratio cases. The combination of those possible reasons leads to the weaker acoustic waves for the higher density ratio cases. The far field pressure spectra are not scaled well with the Taylor micro scale at the maximum sound source position differently from the isothermal case. This would be due to the different sound source characteristics in the variable density ratio cases, which are largely affected by the mean density profile, whereas the sound sources are basically determined by the turbulent motion (including shocklets) in the isothermal mixing layer. Note that the energy spectra are scaled well with the Taylor micro scale at the entire range of wave number except for the small difference at the higher wave numbers. In addition, the randomness of the Mach angle increases with increasing the density ratio. The results would suggest that the existence of various modes of instability wave moving with different convective Mach number and generate different Mach waves. The other possibility is that the appearance of a lot of different scales in flows due to the locally different Reynolds number (affected by the temperature

difference) between upper and lower streams. These different scale of turbulence would generate different acoustic waves. Note, however, that the latter effect should become smaller in sufficiently high Reynolds number flows, because the difference in the Reynolds number between the upper and lower streams become relatively smaller (based on the Reynolds number of the mixing layer) than that in the low Reynolds number flows. Also, regardless of the different sound source characteristics between cases, density ratio does not affect the nonlinearity of acoustic waves significantly at least in the present range of density ratio and the convective Mach number.

Chapter 6

Concluding Remarks

In this thesis, the important parameters of the Mach number and the temperature ratio dependence on the sound sources and generated acoustic waves were investigated toward the accurate prediction of the supersonic jet noise. Direct numerical simulations (DNS) of the isotropic compressible turbulence and the temporally evolving compressible mixing layer were conducted. The former simulation was used to understand the effects of the turbulent Mach number which is closely related with the smaller scale turbulent motion. The latter was used to analyze the convective Mach number and density (temperature) ratio dependence on the sound source and acoustic wave characteristics. To understand the relationship between the change in flows and the sound sources, the source terms of the Lighthill equation which are numerically obtained by DNS results were analyzed. The obtained results for those parameter dependence on the sound source and acoustic wave characteristics are described as follows.

Turbulent Mach number dependence

It was found that two main sound sources are generated by turbulent fluctuations depending on the turbulent Mach number in the isotropic compressible turbulent simulation. One is vortex which exists in all range of turbulent Mach numbers, and the other is eddy shocklet generated only in the higher turbulent Mach numbers. The detail characteristics of sound sources originated by vortices were investigated by using the result of low turbulent Mach number. On the other hand, sound sources generated by shocklets were investigated by extracting shocklets.
The characteristics of sound sources by vortices are as follows:

- The Reynolds stress term is the most contributer to the overall sound sources, because the term is the most affected by vortices. In incompressible flows, the

Reynolds stress term shows the exactly the same distribution as the second invariant of the velocity gradient tensor which is often used to extract vortical structures.

- The entropy term is generated by two terms related with diffusion (and so temperature) in the entropy equation. Only the density contribution of the entropy term is affected by the temperature difference, because the pressure contribution is determined by velocity in nearly incompressible flows. The signs of the density contribution of the entropy term and the Reynolds stress term are the same. Thus, the Reynolds stress term and the entropy term are partially intensified each other. Note, however, that the contribution of the entropy term would become smaller with increasing the Reynolds number due to the smaller thermal conductivity and viscosity for the higher Reynolds numbers, though, the trend was not observed in the present range of the Reynolds numbers.

- Viscous term is negligible.

- For the Reynolds number dependence, the smaller scale and larger peak values appear with increasing the Reynold number, because the turbulent motion become more active for the higher Reynold numbers.

The characteristics of sound sources by eddy shocklets are as follows:

- All source terms of the Lighthill equation show larger values across or on shocklets. Note, however, that the contribution of the viscous term would become smaller for the higher Reynolds numbers because of the smaller viscosity for those flows, though, the trend was not observed in the present range of the Reynolds numbers.

- The Reynolds stress term and the entropy term are canceled out each other across shocklets. This is because, those terms show different jump directions across shocklets.

- Sound sources by shocklets become stronger with increasing the turbulent Mach number and the Reynolds number, because those parameters increase the probability of the occurrence of shocklets and their strength.

- The effects of shocklets are also observed in the isothermal mixing layer simulation for $M_c \geq 1.5$, and show similar characteristics with the sound sources in the isotropic compressible turbulent simulation. The cases affected by shocklets show larger turbulent Mach number than the remaining case.

Convective Mach number dependence

The acoustic waves become weaker with increasing the convective Mach number in the temporally evolving compressible mixing layer simulation. One reason is that the strength of vortices (as important sound sources) decreases with increasing the convective Mach number by the compressibility effects. In addition, the results of the higher convective Mach number cases ($M_c \geq 1.5$) suggested that the shocklets (as the other sound sources) in flows affects the acoustic wave characteristics. The sound source characteristics for those cases are basically the same as those in the isotropic compressible turbulent simulation with shocklets. Note also that those cases showed that the turbulent Mach number is high enough to generate shocklets. The effects of shocklets on the acoustic wave characteristics are suggested in the following:

- Acoustic waves by shocklets increases the non-linearity of the acoustic weaves (but the degree of non-linearity is still small).

- Shocklets increases the randomness of the Mach angle.

Density (temperature) ratio dependence

In the temporally evolving compressible mixing layer simulation, the effects of density (temperature) ratio were also investigated. The results showed that the acoustic waves become weaker with increasing the density ratio. There are two possible reasons. One is that vortices are weakened with increasing the density ratio. The other is that the occurrence of the canceling out of the Reynolds stress term and the entropy term for the variable density ratio cases. This is because the profile of the Reynolds stress is affected by the mean density profile significantly, so that it leads to the similar profiles (but the signs are opposite) of the Reynolds stress component and the entropy component of the Lighhill's turbulent stress tensor and canceling out of the Reynolds stress term and the entropy term. The combination of the two reasons (weaker vortices and the canceling out of the source terms) cause the weaker acoustic waves with increasing the density ratio. In addition, the effects of the density ratio on the acoustic wave characteristics are as follows:

- The non-linearity of the acoustic waves are not affected significantly by the density ratio at least in the present range of the density ratio and the convective Mach number.

- The results of the computed Mach angle showed that the different development of the acoustic waves depending on the density ratio. In addition, the deviation of the Mach angle from the averaged value increases with increasing the density ratio.

The different development and the larger deviation of the Mach angle for the variable density ratio cases suggest the two possible reasons. One is that the appearance of the various modes of instability wave moving with different convective Mach number which generates different Mach wave. This would be due to the temperature difference over the mixing layer which changes the speed of sound, and so, the local Mach number. The other possibility is that the appearance of the different scales of turbulence over the mixing layer due to the locally different Reynolds number affected by the temperature difference. The created different scales of turbulence would generate different acoustic waves and affects the acoustic wave characteristics. Note, however, that the latter effect (the appearance of difference scales over the mixing layer) would be smaller for the higher Reynolds number flows as explained in the following.

Toward the prediction for the actual jets

For the final topic of this thesis, the applicability of the knowledge obtained by this thesis to the actual supersonic jets are discussed. The main discussion is proceeded by focusing on the relationship between the conditions of the temporally evolving compressible mixing layer and the actual jets. A relationship between the convective Mach number M_c and the jet Mach number M_J is considered[71]:

$$M_c = \frac{M_J\sqrt{T_{\text{ratio}}}}{1+\sqrt{T_{\text{ratio}}}}, \tag{6.1}$$

where T_{ratio} is the temperature ratio between the jet and the atmosphere. In the temporally evolving compressible mixing layer, the temperature ratio T_{ratio} is the same as the density ratio s. Thus, we use the relation in the following:

$$M_c = \frac{M_J\sqrt{s}}{1+\sqrt{s}}. \tag{6.2}$$

Note that the discussion above is only applicable to the cases of the isothermal or hot jets. The cold jets can be considered in a similar way, but they are not considered here. Tab. 6.1 shows the corresponding jet conditions of the temporally evolving compressible mixing layer. Firstly, the knowledge which would be independent of the Reynolds number is discussed. After the discussion, the knowledge could be affected by the Reynolds

number is mentioned.

For the Mach number effects, generation of shocklets is one of the important effects, because the results showed that it would affect the acoustic wave characteristics significantly: Increases the non-linearity of the acoustic waves; the larger deviation of the Mach angle; the appearance of the smaller scale acoustic waves (based on the scale of vortices). The effects become larger for $M_c > 1.5$, so that shocklets would take the important role for $M_j > 3.0$ jets. The other important effect is that the weaker acoustic waves with increasing the Mach number. In our simulation results, the degree of the effects seems not to be dependent on the Mach number significantly, so that the effects should be considered equally in all range of the Mach number at least in the range of the computed convective Mach numbers.

For the temperature effects, the acoustic waves are weakened with increasing the temperature (density) ratio. There are two possible reasons. One is the canceling out of the Reynolds stress term and the entropy term for hot jets. The other is the strength of vortices are weakened with increasing the temperature ratio. Those would occur independent of the Reynolds number, so that they should be considered in hot jets. Also, the increase of the randomness of the Mach angle with increasing the temperature ratio would be taken in account. This is because one possible reason is that the appearance of the several unsteady modes moving with different convective Mach number which generates different Mach wave. The effects of temperature discussed above are very crucial for the highest temperature ratio case of $T_{\text{ratio}}(= s) = 8$. If the condition of a liquid rocket motor $T_{\text{ratio}} = 6.48$[3] is recalled, those effects should be very important for the applications of rockets.

Effects of Reynolds number

Finally, the obtained results which could (would) be affected by the Reynolds number are discussed. Here we discuss based on the each computation of the isotropic compressible turbulence and the temporally evolving compressible mixing layer.

In the isotropic compressible turbulent simulation, the entropy term for the lower turbulent Mach numbers should be carefully treated. The generation of the entropy term in the lower turbulent Mach number flows is caused by the diffusion process. This would be smaller for the higher Reynolds number flows due to the smaller viscosity and thermal conductivity, though the trend was not observed in the present range of the Reynolds number. In addition, the viscous term generated by shocklets for the higher turbulent Mach numbers showed non-negligible contribution. This could also

Case	M_c	$s = T_{\text{ratio}}$	M_J
TA12	1.2	1	2.4
TA15	1.5	1	3.0
TA18	1.8	1	3.6
TB02	1.5	2	2.56
TB04	1.5	4	2.25
TB08	1.5	8	2.03

Table 6.1: The relationship between the conditions of the temporally evolving compressible mixing layer and actual jet condition. M_c is the convective Mach number, M_J is the jet Mach number and T_{ratio} is the temperature ratio.

be due to the limited Reynolds number in the present computation. As the viscosity become smaller, the contribution of the viscous term generated by shocklets could become smaller in the higher Reynolds numbers. However, the trend was not also observed in the present range of the Reynolds number. Note that the contribution of the viscous term is negligible in the temporally evolving compressible mixing layer with shocklets, so that the contribution of the viscous term by shocklets is expected to be negligible in the mixing layer (in which large scale structures exist) even in not so high Reynolds number flows.

The temporally evolving compressible mixing layer computation showed that different structures of turbulence over the mixing layer for the higher density (temperature) ratio cases. This is due to the different Reynolds number over the mixing layer. Although the effects are large in the present Reynolds number, the effects would be smaller for the higher Reynolds number. This is because, if we consider the limit of zero viscosity, the effects should be negligible. Thus, the degree of the deviation of the Mach angle from the averaged value for variable density ratio cases could be affected by the Reynolds number.

Appendix A

Velocity dependence on sound source strength in isotropic compressible turbulence

Proposed velocity dependence on the acoustic power has taken an important role, especially, in jet noise research. Firstly, Lighthill[12] showed that the acoustic power is proportional to the 8th power of jet velocity U_J^8 for sub-sonic jets. Proundman[59] showed that the power law is changed to the 5th power in isotropic turbulence. Later, Williams[13] derived the 3rd power law U_J^3 for supersonic jets by applying the Lighthill's idea to the supersonic context. In this appendix, the velocity dependence on the sound source strength (defined by the square of sound sources) is investigated by following those previous studies. Fig A.1 shows that the velocity dependence on sound source strength for all terms. Note that the values are spatially averaged. Three individual source terms indicate that the power law is changed to the higher values for larger velocities (corresponds to the higher turbulent Mach numbers). Term total, however, the slope becomes rather shallower. Those behavior could be explained by the change of the mechanism between the lower turbulent Mach numbers and the higher turbulent Mach numbers as discussed in Chap. 4. In the lower turbulent Mach number flows, only vortices are sound sources, but, in the higher turbulent Mach number flows, eddy shocklets become the other important sound sources. This would lead to change the exponent of the slope in the three individual source terms. The reason why the term total show shallower slope for the higher velocities (turbulent Mach numbers) would be the canceling out of the Reynolds stress term and the entropy term across shocklets in the higher turbulent Mach numbers.

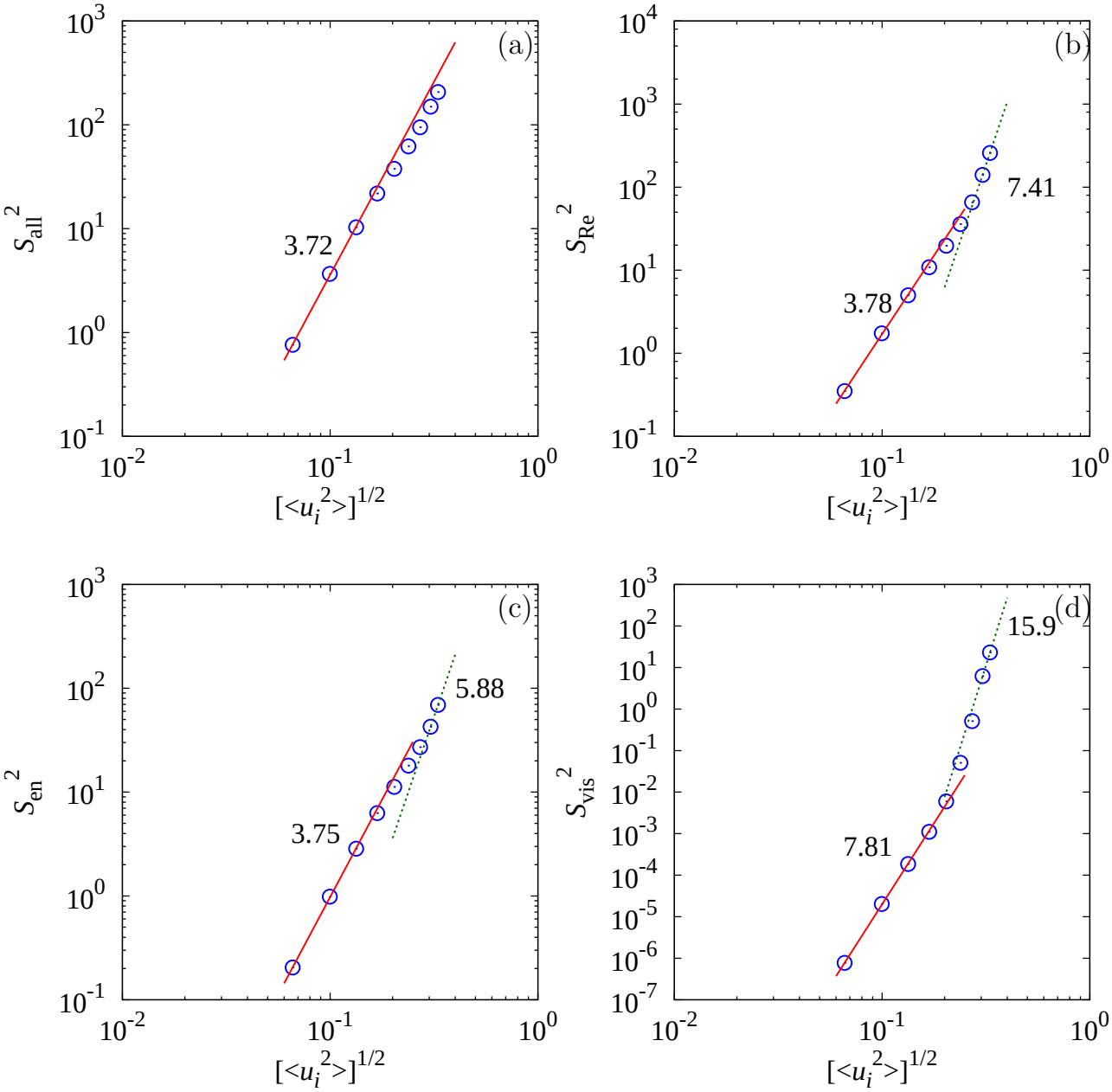

Figure A.1: Velocity dependence on sound sources of (a) term total S_{all}, (b) Reynolds stress term S_{Re}, (c) entropy term S_{en} and (d) viscous term S_{vis} for $R_{\lambda 0} = 130$.

Appendix B

Sound sources for lower density side in temporally evolving compressible mixing layer

In Chap. 5, we focused on the acoustic waves in the higher density side because of the importance in hot jets. In this appendix, the higher density side which is important in cold jets is discussed. The speed of sound and density at the lower density side is used for the constant values in the source terms of the Lighthill equation. The source terms in the variable density mixing layer for the lower density side is written as;

$$\begin{aligned} S_{\mathrm{Re}} &= \frac{\partial \rho u_i u_j}{\partial x_i \partial x_j}, \\ S_{\mathrm{en}} &= \frac{\partial (\delta_{ij}[p - p_{\mathrm{ave}} - c_1^2(\rho - \rho_1)])}{\partial x_i \partial x_j}, \\ S_{\mathrm{vis}} &= \frac{\partial \left(\mu \left(\frac{\partial u_i}{\partial x_j} \frac{\partial u_j}{\partial x_i} - \frac{2}{3} \delta_{ij} \frac{\partial u_k}{\partial x_k} \right) \right)}{\partial x_i \partial x_j}, \\ S_{\mathrm{all}} &= S_{\mathrm{Re}} + S_{\mathrm{en}} + S_{\mathrm{vis}}, \end{aligned} \tag{B.1}$$

where $()_1$ denotes the values of the lower density side. Fig. B.1 shows that the averaged distribution of term total in the y direction. Note that the density at the lower density side ρ_1 is used for the normalization. The sound source strength becomes larger with increasing the density ratio the trend of which is opposite in the discussion of the higher density side (Fig. 5.35). Similar trend except the highest density ratio case $s = 8$ is observed in the far field pressure (Fig. B.2). The results suggest that the discussion of the sound sources still could be a key to understand the far field acoustic waves.

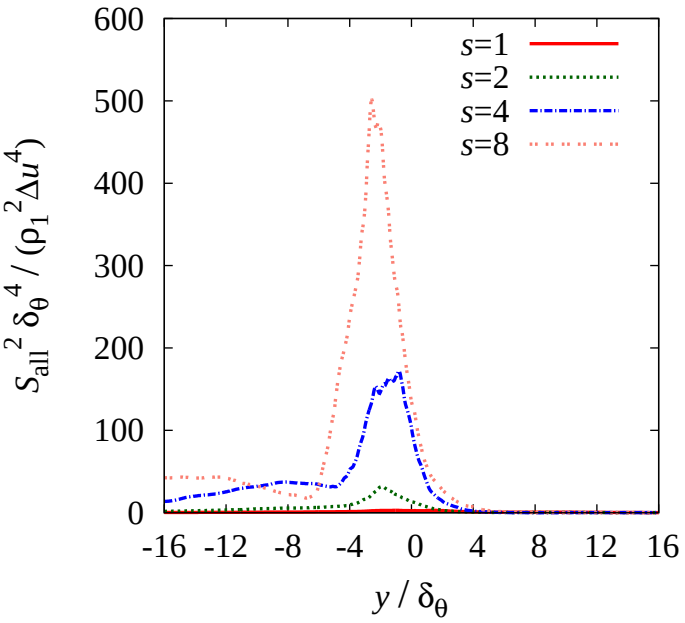

Figure B.1: Averaged overall sound sources for higher density side in the y direction for four different density ratios:—, TA15; ···, TB02; – · –, TB04; ·· ··, TB08.

However, the careful discussion of the difference in trend between the sound sources and the acoustic waves for the highest density ratio case $s = 8$ is necessary. One possible reason for the different trend of the far field pressure with sound source for $s = 8$ could be affected by the flow field, because the flow spreads to the lower density side much further than the other cases. The effects need to be checked by the computation with sufficient computational range to understand the relationship between the sound sources and the acoustic waves for that side correctly. The Reynolds stress term and the entropy term also show different trend with those for the higher density side. Those strength decreases monotonically with increasing the density ratio (cf. Fig. 5.38).

Finally, the contribution of each source term to the overall sound sources are discussed. The sound source strength is computed by the integral of the averaged distributions of term total (Fig. B.1) and the Reynolds stress term and the entropy term (Fig. B.3). The strength of the viscous term is also computed similarly. The results are shown in Fig. B.4. For $s > 1$, the most contributer to the overall sound sources is the entropy term, whereas it was the Reynolds stress term for the sound sources of the higher density side (Fig. 5.39). On the other hand, the canceling out of the Reynolds stress term and the entropy term for the variable density ratio cases remains, because it is determined only by the mean density profile (Sec. 5.3.2).

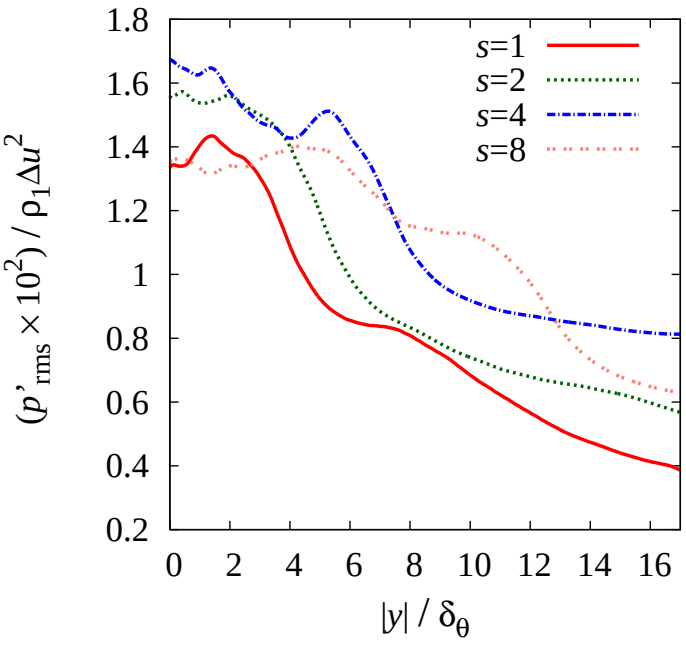

Figure B.2: Averaged rms values of pressure fluctuation for higher density side in the y direction for four different density ratios:—, TA15; ···, TB02; – · –, TB04; ·· ··, TB08.

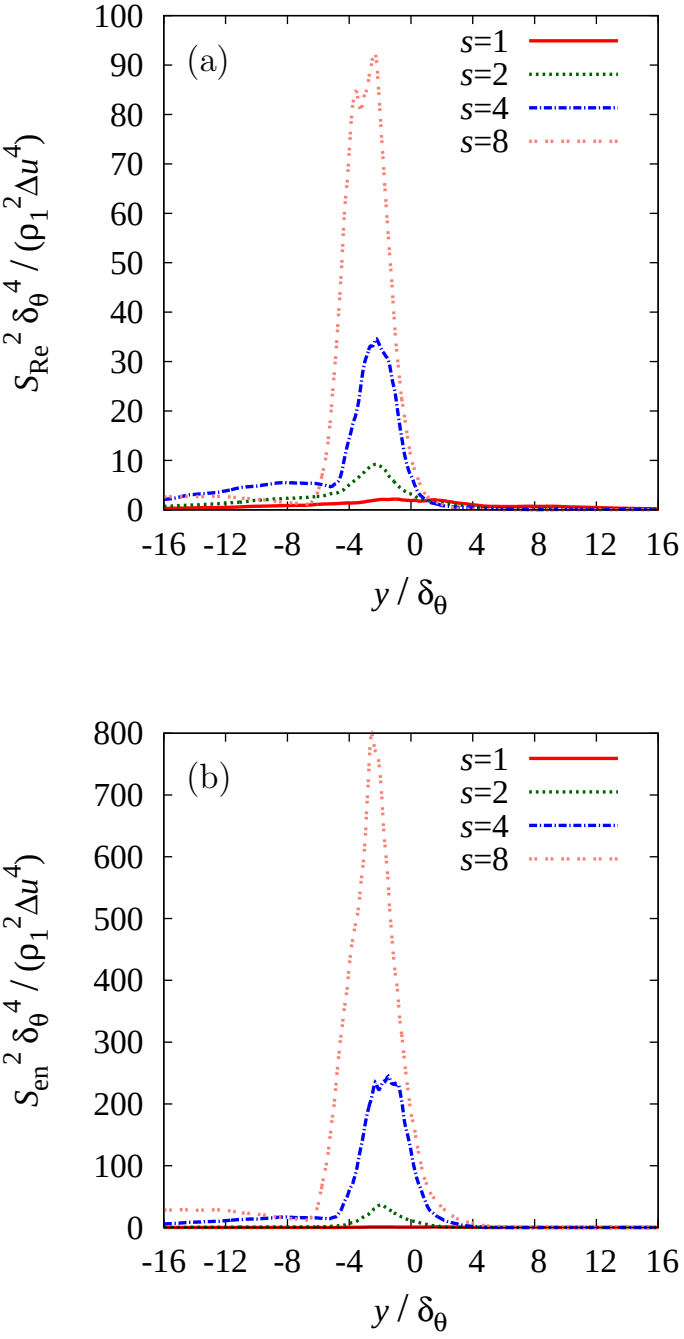

Figure B.3: Averaged source terms for higher density side of (a) Reynolds stress term and (b) entropy term in the y direction for four different density ratios:—, TA15; ···, TB02; – · –, TB04; ·· ··, TB08.

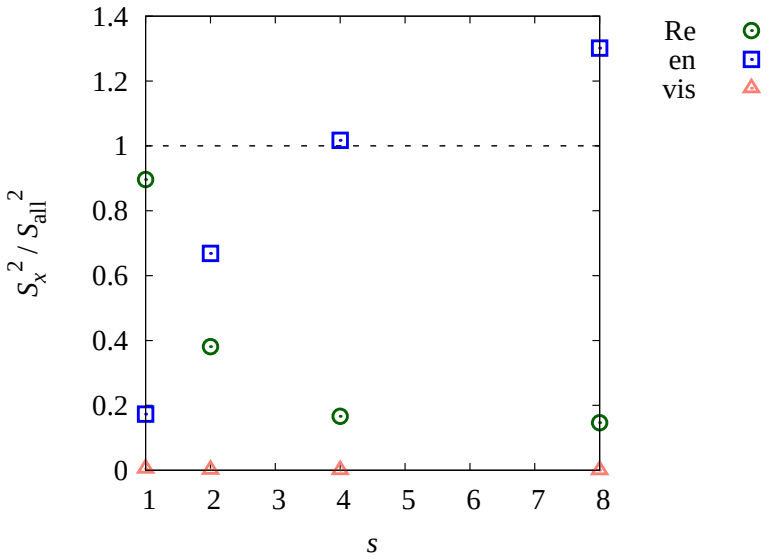

Figure B.4: The ratio of each term to the overall sound source in the sound source strength for higher density side with four different density ratios:◯, Reynolds stress term; □, entropy term; △, viscous term.

Appendix C

Taylor micro scale

In the present study, the Taylor micro scale takes an important role in the analysis, so that the derivation of the Taylor micro scale is briefly described by following the explanation of Pope[10]. The Taylor micro scale is related to the two-point correlation of velocity. The integral scale is also related to the two-point correlation. Thus, both the Taylor micro scale and the integral scale are explained together. Here, isotropic homogeneous turbulence is considered.
We start with two-point correlation of velocity B_{ij}:

$$\begin{aligned} B_{ij}(\mathbf{r}) &= < u_i(\mathbf{x}+\mathbf{r})u_j(\mathbf{x}) >, \\ B_{ij}(0) &= < u_i(\mathbf{x})u_j(\mathbf{x}) >= \delta_{ij}u_{\mathrm{rms}}^2, \end{aligned} \tag{C.1}$$

where $u_{\mathrm{rms}} = \sqrt{< u_i^2/3 >}$ is the root mean square of the velocity and $< \cdot >$ denotes the spatial average. Note that B_{ij} is independent of $\mathbf{x}$. In isotropic turbulence, B_{ij} is written with two scalar functions f and g as follows:

$$B_{ij} = u_{rms}^2\Big(\delta_{ij}g(r) + (f(r) - g(r))\frac{r_i r_j}{r^2}\Big), \tag{C.2}$$

where r is the distance from the origin. If $\mathbf{r} = r\mathbf{e}_1$, f and g is written as;

$$\begin{aligned} f(r) &= \frac{< u_1(\mathbf{x}+\mathbf{e}_1 r)u_1(\mathbf{r}) >}{< u_1^2 >} = \frac{B_{11}}{u_{\mathrm{rms}}^2}, \\ g(r) &= \frac{< u_2(\mathbf{x}+\mathbf{e}_1 r)u_1(\mathbf{r}) >}{< u_2^2 >} = \frac{B_{22}}{u_{\mathrm{rms}}^2}, \end{aligned} \tag{C.3}$$

where $B_{33} = B_{22}$ and $B_{ij} = 0$ for $i \neq j$. From (Eq. C.3), f and g are called as the longitudinal and transverse functions, respectively. Note that $f(0) = g(0) = 1$ are given for the normalization.

From the correlation functions of f and g, two length scales of the integral scale and the Taylor micro scale are derived. Firstly, the integral scale is introduced. The longitudinal and the transverse integral scales are defined by the integral of the correlation functions:

$$\begin{aligned} L_f &= \int_0^\infty f dr, \\ L_g &= \int_0^\infty g dr, \end{aligned} \tag{C.4}$$

where $L_g = L_f/2$ in isotropic turbulence. The integral scales are taken as the representative scale for the large scale of turbulence.

The second length scale derived by the correlation functions is the Taylor micro scale. The longitudinal Taylor micro scale λ_f derived by f is considered here. As f is an even function of $\mathbf{r}$, the first derivative at the origin is zero $\partial f/(\partial r)(0) = 0$. On the other hand, the second derivative $\partial^2 f/(\partial r^2)(0)$ is negative. Thus, the Taylor micro scale is defined using the second derivative as:

$$\lambda_f = \frac{1}{\sqrt{-\frac{1}{2}\frac{\partial^2 f}{\partial r^2}(0)}}. \tag{C.5}$$

To understand the meaning, a parabolic function $p(r)$ which osculates f at the origin (Fig. C.1) is considered:

$$\begin{aligned} p(r) &= 1 + \frac{1}{2}\frac{\partial^2 f}{\partial r^2}(0) r^2, \\ &= 1 - \frac{r^2}{\lambda_f^2}. \end{aligned} \tag{C.6}$$

Thus, λ_f is the length scale at which the osculating parabolic function intersects the horizontal axis (Fig. C.1). The Taylor micro scale is always smaller than the integral scale, so that the scale is used as the representative scale for the smaller scales of turbulence. After some manipulation, the Taylor micro scale is shown to be related with the velocity derivative (See [10] in detail):

$$\begin{aligned} 2\frac{u_{\rm rms}^2}{\lambda_f^2} = -u_{\rm rms}^2 \frac{\partial^2 f}{\partial r^2}(0) &= -u_{\rm rms}^2 \lim_{r\to 0} \frac{\partial^2 f}{\partial r^2}(r), \\ &= -\lim_{r\to 0} \frac{\partial^2}{\partial r^2} < u_1(\mathbf{x} + r\mathbf{e}_1) u_1(\mathbf{x})) >, \\ &\vdots \\ &= \left\langle \left(\frac{\partial u_1}{\partial x_1} \right)^2 \right\rangle. \end{aligned} \tag{C.7}$$

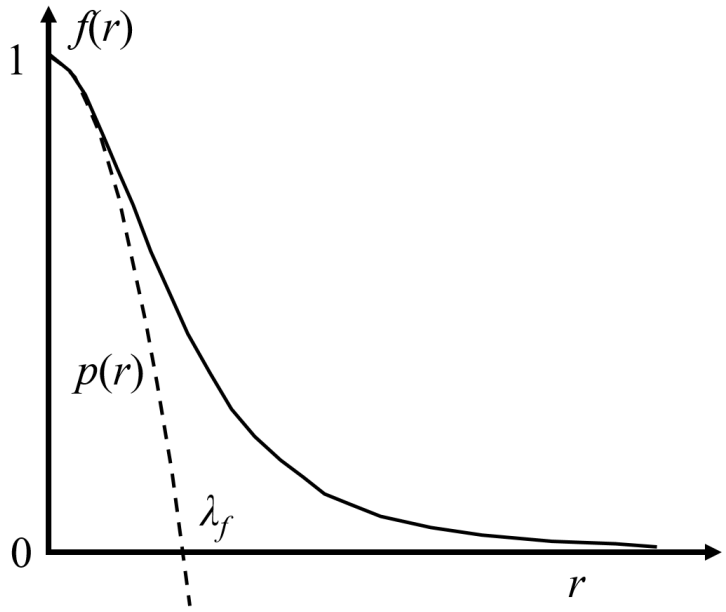

Figure C.1: Definition of the longitudinal Taylor micro scale λ_f. f and p are the longitudinal auto correlation function and the osculating parabola function, respectively[10].

Therefore, the longitudinal Taylor micro scale is written as;

$$\lambda_f = \sqrt{\frac{2u_{\mathrm{rms}}^2}{\frac{\partial u_1}{\partial x_1}}}. \tag{C.8}$$

The transverse Taylor micro scale is also defined as:

$$\lambda_g = \frac{1}{\sqrt{-\frac{1}{2}\frac{\partial^2 g}{\partial r^2}(0)}}, \tag{C.9}$$

where $\lambda_g = \lambda_f/\sqrt{2}$ in isotropic turbulence. Thus, the transverse Taylor micro scale is written as;

$$\lambda_g = \sqrt{\frac{u_{\mathrm{rms}}^2}{\frac{\partial u_1}{\partial x_1}}}. \tag{C.10}$$

References

[1] Tam, C. K., "Supersonic jet noise," *Annu. Rev. Fluid Mech.*, Vol. 27, No. 1, 1995, pp. 17–43.

[2] Suzuki, T. and Lele, S. K., "Shock leakage through an unsteady vortex-laden mixing layer: application to jet screech," *J. Fluid Mech.*, Vol. 490, 2003, pp. 139–167.

[3] Nonomura, T., Morizawa, S., Obayashi, S., and Fujii, K., "Computational Prediction of Acoustic Waves from a Subscale Rocket Motor," *Trans. JSASS Aerospace Tech. Japan*, Vol. 12, No. ists29, 2014, pp. Pe_11–Pe_17.

[4] Zeman, O., "Dilatation dissipation: the concept and application in modeling compressible mixing layers," *Phys. Fluids A*, Vol. 2, No. 2, 1990, pp. 178–188.

[5] Samtaney, R., Pullin, D., and Kosovic, B., "Direct numerical simulation of decaying compressible turbulence and shocklet statistics." *Phys. Fluids*, Vol. 13, No. 5, 2001, pp. 1415–1430.

[6] Pantano, C. and Sarkar, S., "A study of compressibility effects in the high-speed turbulent shear layer using direct simulation," *J. Fluid Mech.*, Vol. 451, 2002, pp. 329–371.

[7] Papamoschou, D. and Roshko, A., "The compressible turbulent shear layer: an experimental study," *J. Fluid Mech.*, Vol. 197, 1988, pp. 453–477.

[8] Vaghefi, N., Nik, M., Pisciuneri, P., and Madnia, C., "A priori assessment of the subgrid scale viscous/scalar dissipation closures in compressible turbulence," *Journal of Turbulence*, Vol. 14, No. 9, 2013, pp. 43–61.

[9] Spencer, B. W. and Jones, B. G., "Statistical investigation of pressure and velocity fields in the turbulent two-stream mixing layer," *AIAA paper*, Vol. 71, 1971, pp. 613.

[10] Pope, S. B., *Turbulent flows*, Cambridge university press, 2000.

[11] Bailly, C. and Fujii, K., "High-speed jet noise," *Mechanical Engineering Reviews*, Vol. 3, No. 1, 2016, pp. 15–00496.

[12] Lighthill, M. J., "On sound generated aerodynamically. I. General theory." *Proc. Roy. Soc. A*, Vol. 211, No. 1107, 1952, pp. 564–587.

[13] Williams, J. E. E., "The noise from turbulence convected at high speed." *Proc. Roy. Soc. A*, Vol. 255, No. 1061, 1963, pp. 469–503.

[14] Tam, C. K. and Burton, D. E., "Sound generated by instability waves of supersonic flows. Part 1. Two-dimensional mixing layers," *J. Fluid Mech.*, Vol. 138, 1984, pp. 249–271.

[15] Tam, C. K. and Burton, D. E., "Sound generated by instability waves of supersonic flows. Part 2. Axisymmetric jets," *J. Fluid Mech.*, Vol. 138, 1984, pp. 273–295.

[16] Tam, C. K. and Hu, F. Q., "On the three families of instability waves of high-speed jets," *J. Fluid Mech.*, Vol. 201, 1989, pp. 447–483.

[17] Tam, C. K., Golebiowski, M., and Seiner, J. M., "On the two components of turbulent mixing noise from supersonic jets," *AIAA paper*, Vol. 1716, 1996, pp. 96.

[18] Williams, J., Simson, J., and Virchis, V., " ' Crackle ' : An annoying component of jet noise," *J. Fluid Mech.*, Vol. 71, No. 02, 1975, pp. 251–271.

[19] Anderson, A. T. and Freund, J. B., "Source mechanisms of jet crackle," *AIAA Paper*, Vol. 2251, 2012, pp. 2012.

[20] Buchta, D. A., Anderson, A. T., and Freund, J. B., "Near-Field Shocks Radiated by High-Speed Free-Shear-Flow Turbulence," *AIAA paper*, Vol. 3201, 2014, pp. 2014.

[21] Nichols, J. W., Lele, S. K., and Spyropoulos, J. T., "The source of crackle noise in heated supersonic jets," *AIAA paper*, Vol. 2197, 2013, pp. 2013.

[22] Krothapalli, A., Venkatakrishnan, L., and Lourenco, L., "Crackle: a dominant component of supersonic jet mixing noise," *AIAA paper*, Vol. 2000, 2000, pp. 2024.

[23] Petitjean, B. P. and McLaughlin, D. K., "Experiments on the Nonlinear Propagation of Noise from Supersonic Jets," *AIAA paper*, Vol. 3127, 2003, pp. 2003.

[24] Powell, A., "On the mechanism of choked jet noise," *Proc. Phys. Soc. London, Sec. B*, Vol. 66, No. 12, 1953, pp. 1039.

[25] Powell, A., "The noise of choked jets," *J. Acoust. Soc. Am.*, Vol. 25, No. 3, 1953, pp. 385–389.

[26] Manning, T. A. and Lele, S. K., "A numerical investigation of sound generation in supersonic jet screech," *AIAA paper*, Vol. 2081, 2000, pp. 2000.

[27] Kandula, M., "On the scaling laws and similarity spectra for jet noise in subsonic and supersonic flow," *Int. J. Acoust. Vib*, Vol. 13, No. 1, 2008, pp. 3–16.

[28] Bodony, D., "Understanding the role of tempreature in free shear flows via modification of the dynamics of the large scales," *CFTR, Proc. Summ. Prog.*, 2010, pp. 227–236.

[29] Bodony, D. J. and Lele, S. K., "Low-frequency sound sources in high-speed turbulent jets," *J. Fluid Mech.*, Vol. 617, 2008, pp. 231–253.

[30] Nonomura, T. and Fujii, K., "Overexpansion effects on characteristics of mach waves from a supersonic cold jet," *AIAA journal*, Vol. 49, No. 10, 2011, pp. 2282–2294.

[31] Nonomura, T., Goto, Y., and Fujii, K., "Aeroacoustic waves generated from a supersonic jet impinging on an inclined flat plate," *International Journal of Aeroacoustics*, Vol. 10, No. 4, 2011, pp. 401–425.

[32] Nagata, Y., Nonomura, T., Fujii, K., and Yamamoto, M., "Analysis of acoustic-fields generated by a supersonic jet impinging on flat and curved inclined plates," *International Journal of Aerospace and Lightweight Structures*, Vol. 3, No. 3, 2013, pp. 357–371.

[33] Nonomura, T., Terakado, D., Abe, Y., and Fujii, K., "A Technique for Freestream Preservation of Finite-Difference WENO on Curvilinear Grid." *Compt. Fluids.*, Vol. 107, 2015, pp. 242–255.

[34] Tsutsumi, S., Ishii, T., Ui, K., Tokudome, S., and Wada, K., "Study on acoustic prediction and reduction of Epsilon launch vehicle at liftoff," *Journal of Spacecraft and Rockets*, Vol. 52, No. 2, 2014, pp. 350–361.

[35] Imamura, T., Enomoto, S., Yokokawa, Y., and Yamamoto, K., "Three-dimensional unsteady flow computations around a conventional slat of high-lift devices," *AIAA journal*, Vol. 46, No. 5, 2008, pp. 1045–1053.

[36] Imamura, T., Hirai, T., Amemiya, K., Yokokawa, Y., Enomoto, S., and Yamamoto, K., "Aerodynamic and aeroacoustic simulations of a two-wheel landing gear," *Procedia Engineering*, Vol. 6, 2010, pp. 293–302.

[37] Bodony, D. J. and Lele, S. K., "On using large-eddy simulation for the prediction of noise from cold and heated turbulent jets," *Phys. Fluids*, Vol. 17, No. 8, 2005, pp. 085103.

[38] Cacqueray, N. D., Bogey, C., and Bailly, C., "Investigation of a high-Mach-number overexpanded jet using Large-Eddy Simulation," *AIAA journal*, Vol. 49, No. 10, 2011, pp. 2171–2182.

[39] Bodony, D. J. and Lele, S. K., "Current status of jet noise predictions using large-eddy simulation," *AIAA journal*, Vol. 46, No. 2, 2008, pp. 364–380.

[40] Bogey, C., Marsden, O., and Bailly, C., "Effects of moderate Reynolds numbers on subsonic round jets with highly disturbed nozzle-exit boundary layers," *Phys. Fluids*, Vol. 24, No. 10, 2012, pp. 105107.

[41] Bogey, C., Marsden, O., and Bailly, C., "Influence of initial turbulence level on the flow and sound fields of a subsonic jet at a diameter-based Reynolds number of 10 5," *J. Fluid Mech.*, Vol. 701, 2012, pp. 352–385.

[42] Bogey, C. and Bailly, C., "Influence of nozzle-exit boundary-layer conditions on the flow and acoustic fields of initially laminar jets," *J. Fluid Mech.*, Vol. 663, 2010, pp. 507–538.

[43] Nonomura, T. and Fujii, K., "Effects of Inflow Shear Layer Parameters on a Transitional Supersonic Jet with a Moderate Reynolds Number," *AIAA Paper*, Vol. 2237, 2013, pp. 2014.

[44] Mendez, S., Shoeybi, M., Sharma, A., Ham, F., Lele, S., and Moin, P., "Large-eddy simulations of perfectly expanded supersonic jets using an unstructured solver," *AIAA journal*, Vol. 50, No. 5, 2012, pp. 1103–1118.

[45] Nichols, J. W., Lele, S. K., Moin, P., Ham, F. E., and Bridges, J. E., "Large-eddy simulation for supersonic rectangular jet noise prediction: effects of chevrons," *AIAA paper*, Vol. 2212, 2012.

[46] Berland, J., Bogey, C., and Bailly, C., "Numerical study of screech generation in a planar supersonic jet," *Physics of Fluids (1994-present)*, Vol. 19, No. 7, 2007, pp. 075105.

[47] Passot, T. and Pouquet, A., "Numerical simulation of compressible homogeneous flows in the turbulent regime." *J. Fluid Mech.*, Vol. 181, 1987, pp. 441–466.

[48] Lee, S., Lele, S. K., and Moin, P., "Eddy shocklets in decaying compressible turbulence." *Phys. Fluids A*, Vol. 3, No. 4, 1991, pp. 657–664.

[49] Pirozzoli, S. and Grasso, F., "Direct numerical simulations of isotropic compressible turbulence: Influence of compressibility on dynamics and structures." *Phys. Fluids*, Vol. 16, No. 12, 2004, pp. 4386–4407.

[50] Kida, S. and Orzag, S. A., "Enstrophy budget in decaying compressible turbulence." *J. Sci. Comput.*, Vol. 5, No. 1, 1990, pp. 1–34.

[51] Wang, J., Shi, Y., Wang, L.-P., Xiao, Z., He, X., and Chen, S., "Effect of shocklets on the velocity gradients in highly compressible isotropic turbulence." *Phys. Fluids*, Vol. 23, No. 12, 2011, pp. 125103.

[52] Wang, J., Shi, Y., Wang, L.-P., Xiao, Z., He, X., and Chen, S., "Effect of compressibility on the small-scale structures in isotropic turbulence." *J. Fluid Mech.*, Vol. 713, 2012, pp. 588–631.

[53] Sarkar, S., Erlebacher, G., Hussaini, M., and Kreiss, H., "The analysis and modelling of dilatational terms in compressible turbulence," *J. Fluid Mech.*, Vol. 227, 1991, pp. 473–493.

[54] Sarkar, S., "The pressure–dilatation correlation in compressible flows," *Phys. Fluids A*, Vol. 4, No. 12, 1992, pp. 2674–2682.

[55] Sarkar, S., "The stabilizing effect of compressibility in turbulent shear flow," *J. Fluid Mech.*, Vol. 282, 1995, pp. 163–186.

[56] Vreman, A., Sandham, N., and Luo, K., "Compressible mixing layer growth rate and turbulence characteristics," *J. Fluid Mech.*, Vol. 320, 1996, pp. 235–258.

[57] Freund, J. B., Lele, S. K., and Moin, P., "Compressibility effects in a turbulent annular mixing layer. Part 1. Turbulence and growth rate," *J. Fluid Mech.*, Vol. 421, 2000, pp. 229–267.

[58] Sarkar, S. and Hussaini, M. Y., "Computation of the sound generated by isotropic turbulence," Tech. rep., DTIC Document, 1993.

[59] Proudman, I., "The generation of noise by isotropic turbulence," *Proceedings of the Royal Society of London A: Mathematical, Physical and Engineering Sciences*, Vol. 214, The Royal Society, 1952, pp. 119–132.

[60] Choi, G., Li, Y., Tanahashi, M., and Miyauchi, T., "Sound generation mechanism in turbulent mixing layer," *Proc. Turbulence and Shear Flow Phenomena–3*, Vol. 2, 2003, pp. 279–284.

[61] Colonius, T., Lele, S. K., and Moin, P., "Sound generation in a mixing layer," *J. Fluid Mech.*, Vol. 330, 1997, pp. 375–409.

[62] Crighton, D. and Huerre, P., "Shear-layer pressure fluctuations and superdirective acoustic sources," *J. Fluid Mech.*, Vol. 220, 1990, pp. 355–368.

[63] Avital, E., Sandham, N., and Luo, K., "Mach wave radiation by mixing layers. Part I: Analysis of the sound field," *Theor. Comput. Fluid Dyn.*, Vol. 12, No. 2, 1998, pp. 73–90.

[64] Avital, E., Sandham, N., and Luo, K., "Mach wave radiation by mixing layers. Part II: Analysis of the source field," *Theor. Comput. Fluid Dyn.*, Vol. 12, No. 2, 1998, pp. 91–108.

[65] Kleinman, R. R. and Freund, J. B., "The sound from mixing layers simulated with different ranges of turbulence scales," *Phys. Fluids*, Vol. 20, No. 10, 2008, pp. 101503.

[66] Cacqueray, N. D. and Bogey, C., "Noise of an overexpanded Mach 3.3 jet: non-linear propagation effects and correlations with flow," *Int. J. Aeroacoust.*, Vol. 13, No. 7-8, 2014, pp. 607–632.

[67] Ghosh, S. and Matthaeus, W., "Low Mach number two-dimensional hydrodynamic turbulence: Energy budgets and density fluctuations in a polytropic fluid," *Phys. Fluids A*, Vol. 4, No. 1, 1992, pp. 148–164.

[68] Bayly, B., Levermore, C., and Passot, T., "Density variations in weakly compressible flows," *Phys. Fluids A*, Vol. 4, No. 5, 1992, pp. 945–954.

[69] Cai, X., O ' Brien, E. E., and Ladeinde, F., "Thermodynamic behavior in decaying, compressible turbulence with initially dominant temperature fluctuations," *Phys. Fluids*, Vol. 9, No. 6, 1997, pp. 1754–1763.

[70] Terakado, D. and Hattori, Y., "Density distribution in two-dimensional weakly compressible turbulence," *Phys. Fluids*, Vol. 26, No. 8, 2014, pp. 085105.

[71] Freund, J., Lele, S., and Moin, P., "Numerical simulation of a Mach 1.92 turbulent jet and its sound field," *AIAA journal*, Vol. 38, No. 11, 2000, pp. 2023–2031.

[72] Foysi, H. and Sarkar, S., "The compressible mixing layer: an LES study," *Theor. Comput. Fluid Dyn.*, Vol. 24, No. 6, 2010, pp. 565–588.

[73] Feiereisen, W. J., Reynolds, W. C., and Ferziger, J. H., "Numerical simulation of a compressible homogeneous, turbulent shear flow," *Report TF 13, Thermosci., Div., Mech. Eng., Stanford University*, 1981.

[74] Kennedy, C. A. and Gruber, A., "Reduced aliasing formulations of the convective terms within the Navier–Stokes equations for a compressible fluid," *J. Comput. Phys.*, Vol. 227, No. 3, 2008, pp. 1676–1700.

[75] Pirozzoli, S., "Stabilized non-dissipative approximations of Euler equations in generalized curvilinear coordinates." *J. Compt. Phys.*, Vol. 230, 2011, pp. 2997–3014.

[76] Hu, X. Y., Wang, Q., and Adams, N. A., "An adaptive central-upwind weighted essentially non-oscillatory scheme." *J. Compt. Phys.*, Vol. 229, 2010, pp. 8952–8965.

[77] Ducros, F., Ferrand, V., Nicoud, F., Weber, C., Darracq, D., Gacherieu, C., and Poinsot, T., "Large-eddy simulation of the shock/turbulence interaction," *J. Comput. Phys.*, Vol. 152, No. 2, 1999, pp. 517–549.

[78] Jiang, G.-S. and Wu, C.-c., "A high-order WENO finite difference scheme for the equations of ideal magnetohydrodynamics," *J. Comput. Phys.*, Vol. 150, No. 2, 1999, pp. 561–594.

[79] Balsara, D. S. and Shu, C.-W., "Monotonicity preserving weighted essentially non-oscillatory schemes with increasingly high order of accuracy," *J. Comput. Phys.*, Vol. 160, No. 2, 2000, pp. 405–452.

[80] Bhagatwala, A. and Lele, S. K., "Interaction of a Taylor blast wave with isotropic turbulence," *Phys. Fluids*, Vol. 23, No. 3, 2011, pp. 035103.

[81] Bhagatwala, A. and Lele, S. K., "Interaction of a converging spherical shock wave with isotropic turbulence," *Phys. Fluids*, Vol. 24, No. 8, 2012, pp. 085102.

[82] Miura, H., "Excitations of vortex waves in weakly compressible isotropic turbulence." *J. Turbul.*, Vol. 5, No. 10, 2004, pp. 1–22.

[83] Lee, K., Girimaji, S. S., and Kerimo, J., "Effect of compressibility on turbulent velocity gradients and small-scale structure." *J. Turbul.*, Vol. 10, No. 9, 2009, pp. 1–18.

[84] Vaghefi, N. S. and Madnia, C. K., "Local flow topology and velocity gradient invariants in compressible turbulent mixing layer," *J. Fluid Mech.*, Vol. 774, 2015, pp. 67–94.

[85] Hadjadj, A., Yee, H. C., and Sjögreen, B., "LES of temporally evolving mixing layers by an eighth-order filter scheme," *International Journal for Numerical Methods in Fluids*, Vol. 70, No. 11, 2012, pp. 1405–1427.